AD_____
(Leave blank)

Award Number:
W81XWH-04-1-0594

TITLE:
Pre-clinical and Clinical Evaluation of High Resolution, Mobile Gamma Camera and Positron Imaging Devices

PRINCIPAL INVESTIGATOR:
David R. Gilland, Ph.D.

CONTRACTING ORGANIZATION:
University of Florida
Gainesville, FL, 32611

REPORT DATE:
October 2010

TYPE OF REPORT:
Final

PREPARED FOR: U.S. Army Medical Research and Materiel Command
               Fort Detrick, Maryland 21702-5012

DISTRIBUTION STATEMENT:

REPORT DOCUMENTATION PAGE

Form Approved
OMB No. 0704-0188

1. REPORT DATE *(DD-MM-YYYY)*	2. REPORT TYPE	3. DATES COVERED *(From - To)*
20-10-2010	Final	13 MAY 2004 - 20 SEP 2010

4. TITLE AND SUBTITLE
Pre-clinical and clinical evaluation of high resolution, mobile gamma camera and positron imaging devices

5a. CONTRACT NUMBER

5b. GRANT NUMBER
W81XWH-04-1-0594

5c. PROGRAM ELEMENT NUMBER

6. AUTHOR(S)
David R. Gilland, Ph.D.

Email: gilland@ufl.edu

5d. PROJECT NUMBER

5e. TASK NUMBER

5f. WORK UNIT NUMBER

7. PERFORMING ORGANIZATION NAME(S) AND ADDRESS(ES)
University of Florida, Gainesville, FL 32611

8. PERFORMING ORGANIZATION REPORT NUMBER

9. SPONSORING / MONITORING AGENCY NAME(S) AND ADDRESS(ES)
U.S. Army Medical Research and
and Materiel Command
Fort Detrick, Maryland 21702-5012

10. SPONSOR/MONITOR'S ACRONYM(S)

11. SPONSOR/MONITOR'S REPORT NUMBER(S)

12. DISTRIBUTION / AVAILABILITY STATEMENT
Approved for public release; distribution unlimited

13. SUPPLEMENTARY NOTES

14. ABSTRACT
  The objective of this project is to design, build and evaluate a compact and mobile gamma and positron imaging camera. This imaging device has several advantages over conventional systems: (1) greater flexibility in positioning with respect to the target organ for improved spatial resolution and sensitivity, (2) the ability to image patients who cannot be transported to a radiology suite, for example, intensive care patients, and (3) the potential for greater cost effectiveness for organ-specific imaging tasks, compared with larger, general purpose imaging systems.
  The complete imaging system was assembled at the University of Florida and evaluation studies were performed. Basic performance measures including spatial resolution, system sensitivity, and count rate capability were performed and met design specifications. Reconstructed image quality was assessed using anthropomorphic phantoms. In the initial clinical evaluation, the images from the mobile system compared favorably with images obtained from the same patients using conventional imaging systems.

15. SUBJECT TERMS
Nuclear medicine, PET, SPECT, mobile gamma camera, emission tomography

16. SECURITY CLASSIFICATION OF:			17. LIMITATION OF ABSTRACT	18. NUMBER OF PAGES	19a. NAME OF RESPONSIBLE PERSON USAMRMC
a. REPORT U	b. ABSTRACT U	c. THIS PAGE U	UU	54	19b. TELEPHONE NUMBER *(include area code)*

Standard Form 298 (Rev. 8-98)
Prescribed by ANSI Std. Z39.18

Table of Contents

1. Introduction

The objective of this project was to design, build and evaluate a compact and mobile gamma and positron imaging camera. This imaging device has several advantages over conventional systems: (1) greater flexibility in positioning with respect to the target organ for improved spatial resolution and sensitivity, (2) the ability to image patients who cannot be transported to a radiology suite, for example, intensive care patients, and (3) the potential for greater cost effectiveness for organ-specific imaging tasks, compared with larger, general purpose imaging systems. The complete imaging system was assembled at the University of Florida and evaluation studies were performed. Basic performance measures—including spatial resolution, system sensitivity, and count rate capability—were performed and met design specifications. Reconstructed image quality was assessed using anthropomorphic phantoms. In the clinical evaluation, the images from the mobile system compared favorably with images obtained from the same patients using conventional imaging systems.

2. Body

Tables 1 and 2 outline the Statement of Work for the original and continuation project periods, respectively. This section of the report describes the research efforts related to each of the tasks in the tables:

Section	Task(s)/Table
2.A	01-03/1
2.B	03-04/1
2.C	07-09/1
2.D	10-11/1
2.E	12-13/1
2.F	14-15/1
2.G	16-17/1
2.H	01-03/2
2.I	04-07/2

Table 1: Statement of Work for Original Project Period

#	Activity	Duration (mos.)
	YEAR 1	
	Simulation Studies	
01	Simulation study I: determine required detector orbit	2
02	Simulation study II: determine spatial resolution, detection efficiency, count rate capability, reconstructed image quality	2
	Gantry Design, Construction, and Evaluation	
03	Computer-aided design including intensive care bed	1
04	Specification of mechanical components	1
05	Fabrication of gantry using mock detectors	5
06	Evaluation of mechanical capabilities using mock detectors	5
	Detectors Design, Construction, and Evaluation	
07	Optimization of data acquisition system for high count rate	3
08	Assembly of detector components	6
09	Planar detector performance evaluation	3
	Image Reconstruction Algorithm Development	
10	Unconventional camera orbits/geometries	6
11	New iterative algorithms for limited angle data	6
	YEAR 2	
	System Assembly	
12	Mechanical, electrical assembly of detectors and gantry	2
13	Mechanical performance evaluation	2
	Imaging Performance Evaluation with Phantoms	
14	Planar spatial resolution, detection sensitivity, count rate capability	3
15	Reconstructed image quality	4
	Establish Human Subject Research Protocol	
16	Submit research protocol to local IRB's (UF and USF)	3
17	Identify patient population, coordinate with ICU staff	3

Table 2: Statement of Work for Continuation Project Period

#	Activity	Duration (mos.)
Clinical evaluation of SPECT/PET imager		
01	Imaging software development	4
02	Phase I (patients 1-4): determine (1) optimum injected activity, (2) background (scatter, randoms) subtraction method, (3) image reconstruction method	5
03	Phase II (patients 5-20): clinical assessment	4
Simulation and phantom evaluation of SPECT imager		
04	Collimator design and simulation studies	3
05	Image reconstruction algorithm development	
06	Collimator fabrication	4
07	Experimental phantom evaluation: spatial resolution, sensitivity, SPECT image quality	6

2.A   Simulation Studies (tasks 01 and 02 from Table 1)

We performed simulation studies to evaluate two approaches to imaging positron emission tomography (PET) radionuclides with the compact imaging system. The first approach, which was published in the 2004 IEEE Nuclear Science Symposium Conference Record (included in this report as Appendix 4), involves coincidence detection of the paired gamma photons from the positron annihilation. Due to the physical impediments imposed by the patient bed (Fig. 1, Appendix 4), we simulated a limited angle data acquisition wherein the detectors assume only two positions: anterior/posterior and lateral (Fig. 3, Appendix 4). As a result, oblique projection angles are not sampled.

We evaluated the resulting image quality under several experimental conditions including the effect of image noise and with and without attenuation correction. Also, we assessed the detectability of myocardial defects for two different defect severities. The results of this study demonstrate that image quality was not significantly degraded by random noise (Fig. 5, Appendix 4). Photon attenuation had a moderate degrading effect on image quality, which could be improved only to a small degree by conventional attenuation correction methods. The largest effect on image quality was due to the limited angle nature of the data, which was responsible for approximately 20% intensity artifacts in the myocardial regions (Fig. 5, Appendix 4). In terms of defect detectability, the results of this study showed that relatively mild defects (25% below normal intensity) would be difficult to detect due to the intensity artifacts. However, more severe defects (75% below normal intensity) were clearly detectable in these images (Fig. 6, Appendix 4).

The second approach that we investigated for imaging positron emitters with this system involves single photon emission computed tomography (SPECT) techniques and the use of absorptive collimation. This work was presented at the 2005 IEEE Nuclear Science Symposium and Medical Imaging Conference. The advantage of this approach is that it is not necessary to position a detector beneath the patient bed: sufficient angular sampling may be obtained by rotating a single detector through the anterior 180

degrees. A disadvantage is that a collimator is required, which substantially reduces detector sensitivity. Furthermore, the spatial resolution with the collimated approach can be degraded relative to coincidence imaging, and the penetration of the high energy 511 keV gamma rays through the collimator septa can be problematic. Fortunately, the reduced sensitivity can be compensated in this application by longer scan time. In order to compensate for the spatial resolution degradation and penetration issues, unique image processing methods are being investigated and are described below.

We performed a simulation study to assess the image quality that can be obtained using compact detectors with 511 keV SPECT methods for cardiac imaging. Simulated projection data were generated for a 3D spherical annulus using the GEANT4 Monte Carlo code [1] and a customized Monte Carlo code for SPECT imaging [2]. The simulated detector had a 25 cm x 25 cm field-of-view and a high energy, parallel hole collimator. Data were obtained for 30 equally-spaced angles over 180 degrees. In addition to this SPECT data, a point source image was obtained in order to demonstrate the point spread function and to design a deconvolution filter.

The measured point source sensitivity with this system was 5.4 counts/second/μCi considering only detected counts in a neighborhood around the point. The measured spatial resolution was 17 mm FWHM; however, substantial "tails" to the point spread function were observed due to septal penetration. In order to improve the spatial resolution in the reconstructed image and to reduce the effect of septal penetration, a 3D post-reconstruction deconvolution filter, based on the measured point spread function, was applied. The resulting SPECT images exhibited substantial noise, due to the relatively short acquisition time, and a degree of penetration artifacts. However, the general structure of the annulus is maintained, and with the longer acquisition times that are anticipated in this application, there is promise that clinically useful cardiac SPECT images may be obtained with this approach.

2.B   Gantry Design, Construction and Evaluation (tasks 03-06 from Table 1)

The electro-mechanical gantry allows the detectors to be transported within a hospital and was designed for precise positioning of the detectors with respect to the patient. The computer-aided design images of the gantry that were generated during the design phase are shown in Fig. 1. The detectors are positioned for PET coincidence imaging in anterior/posterior (left) and lateral (right) orientations.
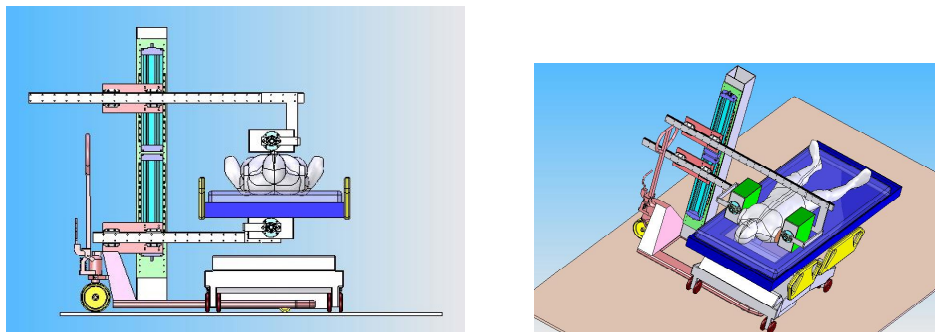

Fig. 1: Computer-aided design drawing of mechanical gantry

The gantry system was designed to position the detectors for PET or SPECT acquisition under the challenging conditions of the bedside environment. Low profile legs slide beneath ICU beds for stable support. The detectors mount to the rails of a

linear bearing set that allows precise horizontal detector motion. Vertical detector motion is motor-driven using electronic motion control modules. Detector pivoting provides the additional, necessary motion dimension. The linear motions and pivot angle are digitally encoded for input to the reconstruction software. In PET mode, the detectors assume a 180 deg. opposing orientation; in SPECT mode, the two detectors can assume a variable angle orientation (90-180 deg.) and orbit the anterior of the patient. In tests with a graduate student laboratory member lying supine on an intensive care unit bed, the gantry was able to position mock detectors in anterior/posterior opposing, lateral opposing, and anterior "L" orientations (Fig. 2).

Fig. 2: Photographs of system gantry with mock detectors positioned in anterior/posterior opposing (left), lateral opposing (center), and anterior "L" orientations.

2.C   Detector Design, Construction and Evaluation (tasks 07-09 from Table 1)

Single detector head prototype.   In the framework of an imager R&D with new generation of flat panel photodetectors, the Jefferson Lab Detector Group developed a fast gamma camera with a field of view of 20cmx20cm. The camera was funded with other funds, prior to the receipt of the Army grant funds at Jefferson Lab, and is intended for a relevant application as a mobile high rate first pass cardiac gamma camera (Fig. 3). When implemented with specialized software with phase analysis, it is expected to be used in prompt detection of myocardial infarction in emergency room patients.
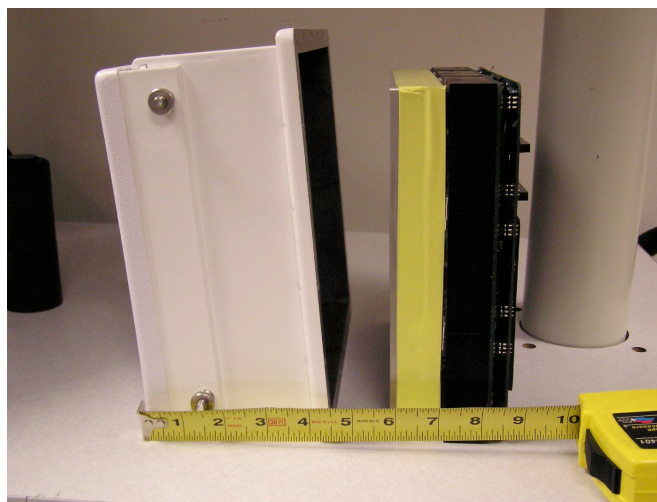

Fig. 3: Prototype compact detector head.

The experience gained with the prototype detector was the following:

1. The Burle 85001 multi-anode photomultiplier tube (PMT) is validated as a good quality photodetector
2. The array of these PMTs can operate as an efficient imager with moderate spatial resolution (due to dead edges around these PMTs), sufficient for cardiac imaging (the prototype field-of-view is 20cm)
3. The implemented first generation fast front-end electronics and data acquisition (DAQ) based readout can operate at rates sufficient for cardiac single-gamma (Tc-99m) first-pass operation

Fast Readout. The output of the PMT's is handled by high-speed data acquisition (DAQ) electronics for high detector count rate capability. Our initial plans to use a conventional multi-channel DAQ system encountered a major problem by our inability to pass a rather low rate event limit of only 25-30kHz in practical implementations. We, therefore, decided to aggressively pursue a completely different method by building our own fast field-programmable gate array (FPGA) DAQ system. To achieve high rate capability, each detector head is connected to a separate, 64 channel FPGA DAQ card which is in turn read via a USB2 link to a hard drive of a separate data acquisition PC. Two data acquisition PCs, one for each detector, send the collected data files for processing to an "event builder" computer where time-stamped data files from each detector are processed and fused into one coincident file or treated separately when used in a single gamma mode. During the coincident file event building phase, the time-stamped events corresponding to two coincident 511 keV quanta are processed and put into a summary file. The summary file lists the calculated x,y gamma event positions and the gamma energies for the two gammas (one from each detector), plus a single time stamp for the coincidence event.

The design of the detector heads involves 4x4 arrays of flat panel Burle 850001 PMTs. Each PMT has four output channels. The readout therefore has 16 x 4 x 2 = 128 readout channels for the system composed of two detector heads. The system is built of 16 channel cards inserted in 64 channel mother boards. Two mother boards are used to read the two detector heads. The data are streamed to disk with each event having a time stamp for post-scan coincidence events identification and image reconstruction. Depending on the final system rate capability, it is planned that data will be also processed *in-situ* to produce feedback images for quality control purposes. To process the data quickly, an economical but powerful small computer farm is considered for the project.

Following the prototype detector evaluation and the fast readout development, one of two detectors for the mobile imaging system was fabricated and evaluated. A summary description is included here.

The detector consists of a pixilated NaI scintillator with individual scintillator pixels that are 5 mm x 5 mm in cross-section and 12.5 mm thick. The total crystal area is approximately 25 cm x 25 cm (Fig. 4, right). The scintillator is optically coupled to an array of position-sensitive photomultiplier tubes (PSPMT). The 4x4 array of PSPMT's (Burle, model 850012-800) are highly compact, particularly in thickness, which makes them ideal for a compact detector design (Fig. 4, left).

Initial tests of detector performance were carried out using a Na-22 point source. Figure 5 shows an example of a raw flood image from a fully illuminated detector head after first-order gain uniformity correction (by adjusting high voltage biases of individual PMTs). Good pixel separation over the whole field-of-view is observed. Response non-uniformities are still evident due to the remaining gain differences and dead regions

between individual PSPMTs. This detector operates with over 100 kHz coincidence trigger rate. The measured energy resolution for selected pixels ranged from 15 to 20%.
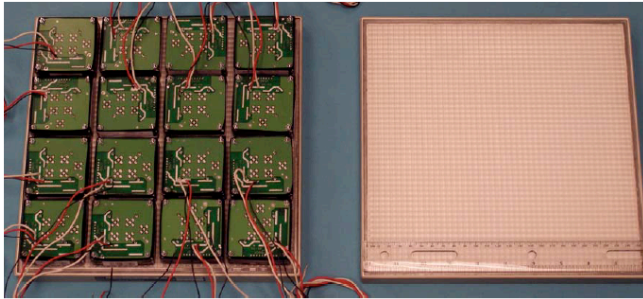

Fig. 4: Left: bottom view of detector showing photomultiplier tube array, Right: view of pixilated NaI scintillator
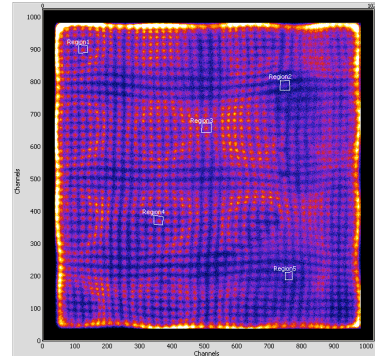

Fig. 5: Flood image for prototype detector.

After the successful fabrication of the first detector, a second detector was built, and tests were performed on the pair of detectors operating in coincidence mode. A Na-22 point source was placed between the two opposing detectors (closer to the left detector), which were 25 cm apart. Figure 6A and 6B show the raw coincidence images for the left and right detectors, respectively. Spatial separation of the detector pixels is evident in this coincidence data. Figure 6C shows the detected energy spectrum from these measurements. An average energy resolution across the field-of-view of approximately 20% was observed.
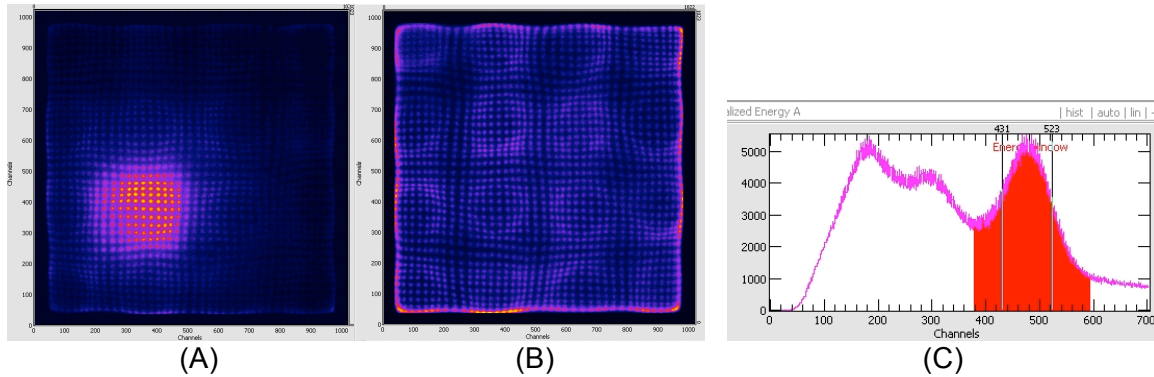

(A)　　　　　　　　　(B)　　　　　　　　　(C)

Fig. 6: (A,B) Coincidence images and (C) measured energy spectrum

2.D. Image Reconstruction Algorithm Development (tasks 10,11 from Table 1)

Novel image reconstruction methods were incorporated into the simulation studies described in section 2.A. In the study described in Appendix 4, which involved coincidence PET data from two opposing detector positions (anterior/posterior and lateral), an iterative, 3D reconstruction method was employed. This method had been used previously to reconstruct limited-angle positron emission mammography data [3] in which a single position of the opposing detectors is acquired. This method was generalized for our purposes to handle the two detector positions. This method computes projection data for all lines-of-response (LORs) in 3D, then updates the image estimate given the discrepancy between the computed LORs and the measured LORS.

10

In the second simulation study, a key feature of the image reconstruction process involved the deconvolution filter, which was designed to mitigate the degrading spatial resolution effects due to collimator septal penetration. The deconvolution, or Metz, filter was designed based on the measured point spread function. The shape of the filter provides recovery of low spatial frequencies, which are associated with the broad tails of the point spread function due to penetration, before rolling off to zero gain at high spatial frequencies where random noise dominates the signal. This filter demonstrated the ability to substantially recover signal and improve spatial resolution in the resulting reconstructed SPECT images while simultaneously controlling image noise.

2.E. System Assembly (tasks 12,13 from Table 1)

The detectors were delivered to UF from Jefferson Lab in April 2007, and an evaluation of the mechanical capabilities of the system with detectors mounted was performed. The added weight of the detectors did impede the mechanical performance of the system. As shown in Fig. 7, the gantry can position the detectors in an anterior/posterior, lateral or both anterior orientations. This work, including an initial imaging performance evaluation, was published in the IEEE Transactions on Nuclear Science (listed as Studenski et. al. 2009 in Section 4 and included in this report as Appendix 1).

Fig. 7: Photograph of system gantry with actual detectors mounted. Detectors are positioned in anterior/posterior (left), lateral (middle), and both anterior (right) orientations

2.F. Imaging Performance Evaluation with Phantoms (tasks 14, 15 from Table 1)

Raw flood images were obtained from both detectors using a 7 μCi ^{22}Na disk source (Fig. 8). In these images, first-order gain uniformity correction has been applied by adjusting the high-voltage biases of individual PMT's. Good pixel separation over the entire field-of-view is evident. Intensity non-uniformities are still present due to factors such as remaining PMT gain differences and gaps between PMT's.
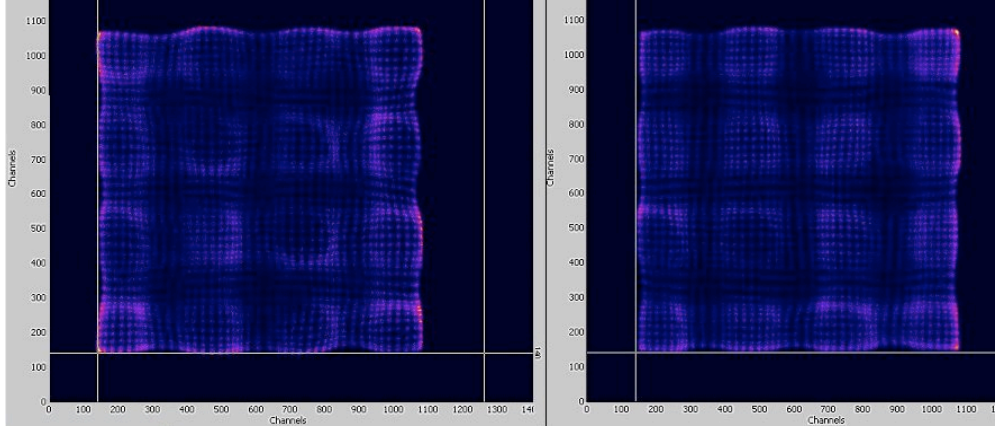
Fig. 8. Raw flood images from detector 1 (left) and detector (2) with ^{22}Na source.

Energy resolution spectra from both detectors using the ^{22}Na source were obtained (Fig. 9). The spectra represent the combined pulse height spectra of all individual detector pixels. The measured FWHM of the photopeak was 24% for detector 1 and 22% for detector 2.
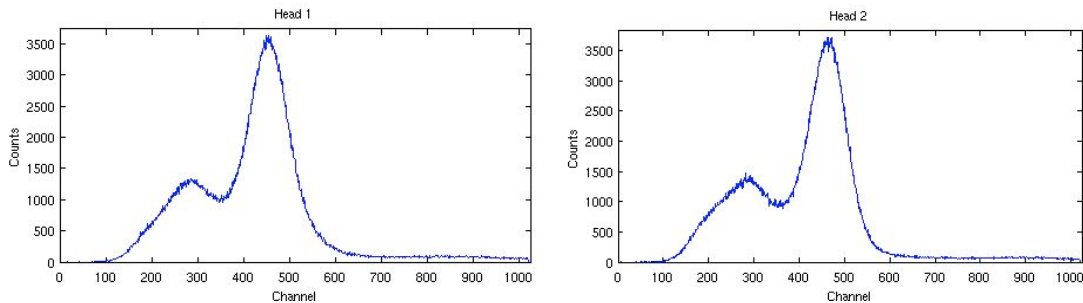

Fig. 9: Measured energy spectra from detector 1 (left) and detector (2) with ^{22}Na source.

The basic SPECT imaging performance of the experimental system was performed including measurements of spatial resolution, system sensitivity and count rate capability using a simple point source. This work resulted in a peer-reviewed publication in IEEE Transactions on Nuclear Science (Studenski et al, 2009), which is included as Appendix 1 in this report. The reader is referred to this publication for a detailed description of this work.

We extended this evaluation using an anthropomorphic cardiac phantom that resembles the human anatomy. This work is described in detail in a peer-reviewed publication in IEEE Transactions on Nuclear Science (Studenski et al, 2010), which is included as Appendix 2 in this report. One of the key results from this work is presented in Fig. 10, which shows a comparison of reconstructed images obtained from the experimental, mobile system with those obtain from a commercial SPECT system. The object was the anthropomorphic cardiac phantom. The phantom myocardium was filled with Tc-99m activity to simulate a SPECT myocardial perfusion study. The results demonstrate the reconstructed image quality that can be produced by this system and the fact that the images are reasonably similar to those produced by a commercial SPECT system.

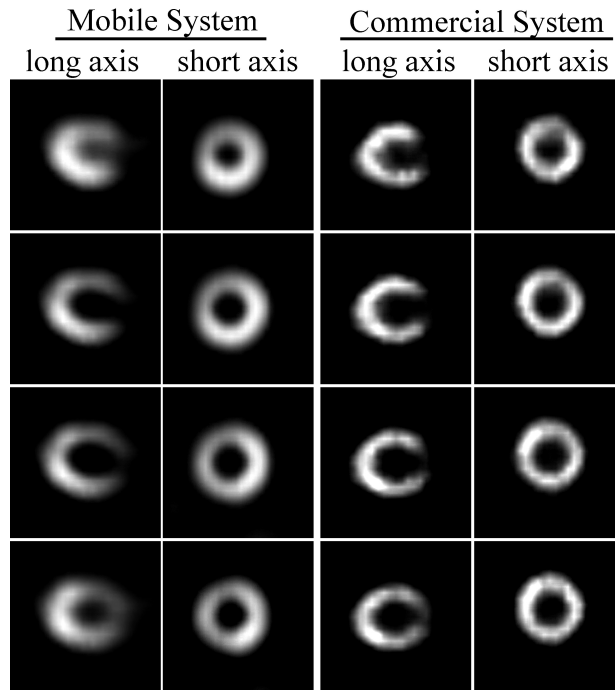|	Mobile System	Commercial System
long axis short axis	long axis short axis

Fig. 10. Comparison of the mobile system's performance to a commercial system using the dynamic cardiac phantom and Tc-99m. The mobile system used 37 angles over 180 degrees and the commercial system used 64 angles over 180 degrees.

During the course of this work using the anthropomorphic cardiac phantom, we made several key developments in the image acquisition and image processing aspects of this system. These developments included a focused region-of-interest for image acquisition that allows the relatively small field-of-view detector to maintain the heart in the field-of-view over all projection angles. The other key development was a method for the reduction of septal penetration effects through deconvolution filtering.

2.G. Establish Human Subjects Research Protocol (tasks 16,17 from Table 1)

Included in the tasks of this project was the establishment of a human subjects research protocol at UF in anticipation of continuation funding of this project that would enable patient evaluation studies. Toward this goal, we prepared a protocol that was approved by the local Institutional Review Board at UF as well as the U.S. Army Medical Research and Materiel Command (USAMRMC), Office of Research Protections (ORP), Human Research Protection Office (HRPO).

2.H. Clinical evaluation of SPECT/PET imager (tasks 01-03 from Table 2)

We performed a clinical evaluation of the mobile camera. A total of seven patients were included in the study. As part of their routine care, the patients received a rest-stress SPECT sestamibi study. Immediately after their routine study, the patients were scanned using the mobile camera. An example case is shown in Fig. 11. The patient

13

was a 52 year old woman with a history of heart disease who was being evaluated for recent angina symptoms.
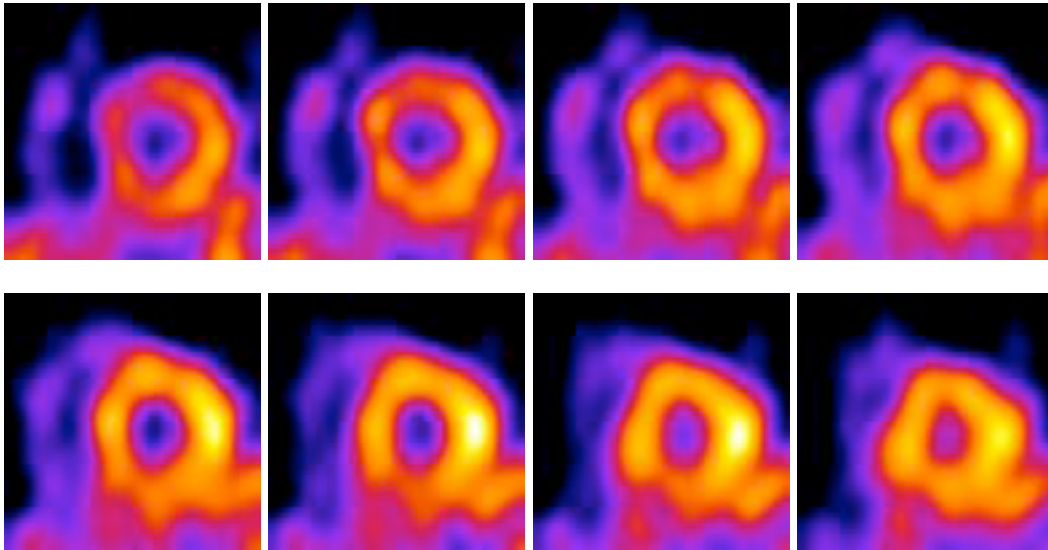

Fig. 11. Reconstructed images from first patient study

The images in Fig. 11 generally have a satisfactory appearance; however the next step was to obtain the images of the patients that were produced by the conventional SPECT camera and compare the image quality of the two image sets. An example of this is shown in Figure 12, which shows the stress images from both the mobile system and the commercial SPECT system in the nuclear medicine clinic. The images from the commercial system have less extra-myocardial intensity, which is possibly due to artifacts from the smaller useful field-of-view of the mobile system and using only 145 degrees (rather than 180 degrees) of projection data. The images from both systems were read as "negative" by Walter Drane, M.D., the Co-Principal Investigator on this grant. These images are representative of the other patient studies that were performed.
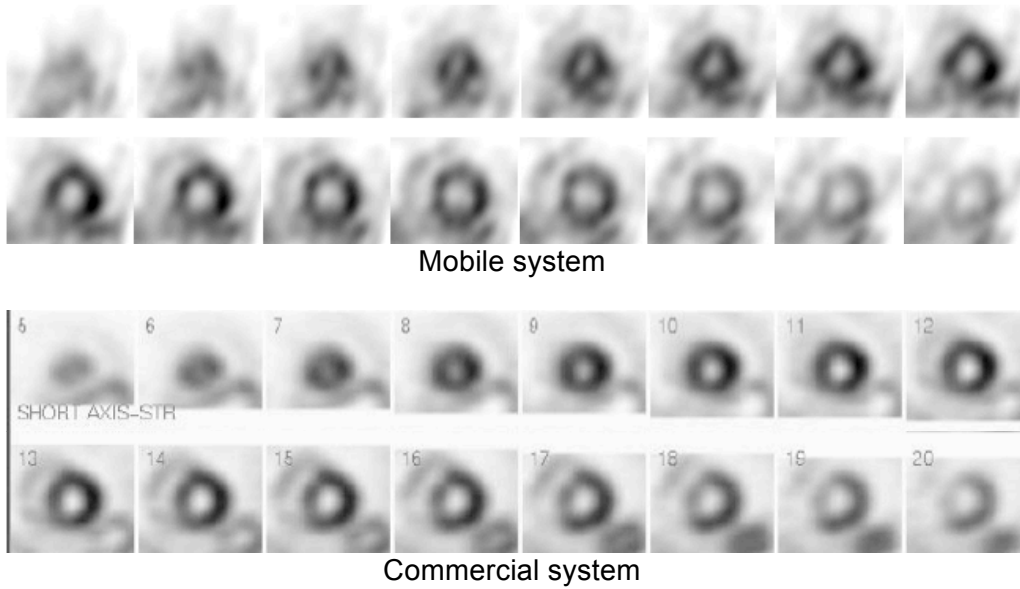
Mobile system

Commercial system

Fig. 12. Comparison of reconstructed images of a patient Tc-99m sestamibi study from the mobile system (top two rows) and a commercial SPECT system (bottom two rows).

Figure 13 shows a second case of a patient with a suspected perfusion defect in the infero-lateral region of the left myocardium (5 o'clock position). The top row of the figure contains images obtained at rest; the bottom row images were obtained at stress.
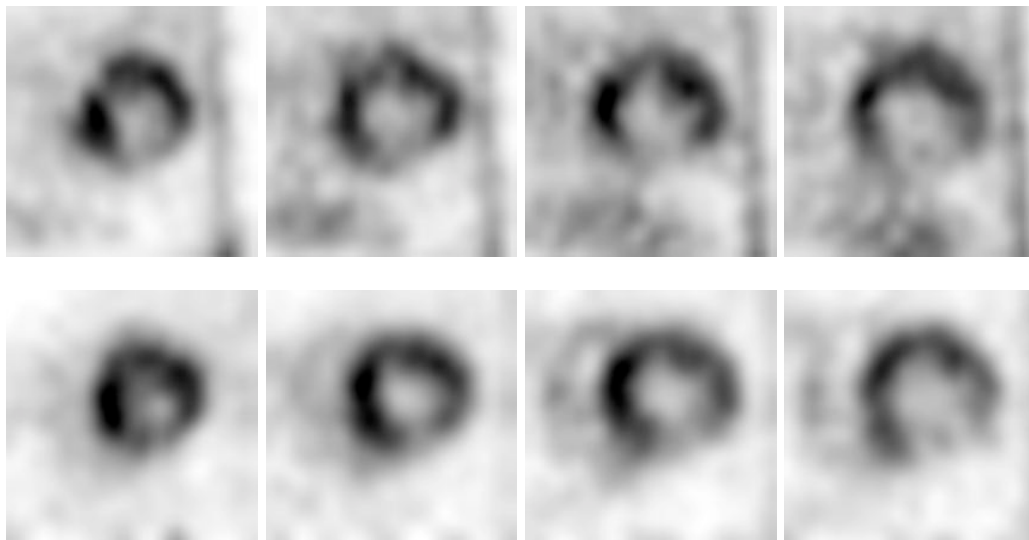

Fig. 13. Reconstructed images of patient with suspected perfusion defect. Top row: rest images; bottom row: stress images.

2.I. Simulation and phantom evaluation of SPECT imager (tasks 04-07, Table 2)

Another major thrust of this research over the last year was the design and testing of a new collimator for high energy (511 keV) SPECT imaging. The collimator uses a

pinhole aperture, rather than conventional parallel holes. The potential advantages of the pinhole design for this application include better spatial resolution/sensitivity trade-off and lighter weight for equivalent stopping power.

Examples of the key results are shown in Figs. 14 and 15, which are the parallel hole collimator (Fig. 14) and the pinhole collimator (Fig. 15) images of a point source. These images were obtained using a Monte Carlo simulation program.   These figures demonstrate that the pinhole collimator reduces the "tails" in the point spread function and eliminates the star artifacts. This star pattern is the result of high energy photons that penetration the septa of the parallel hole collimator.
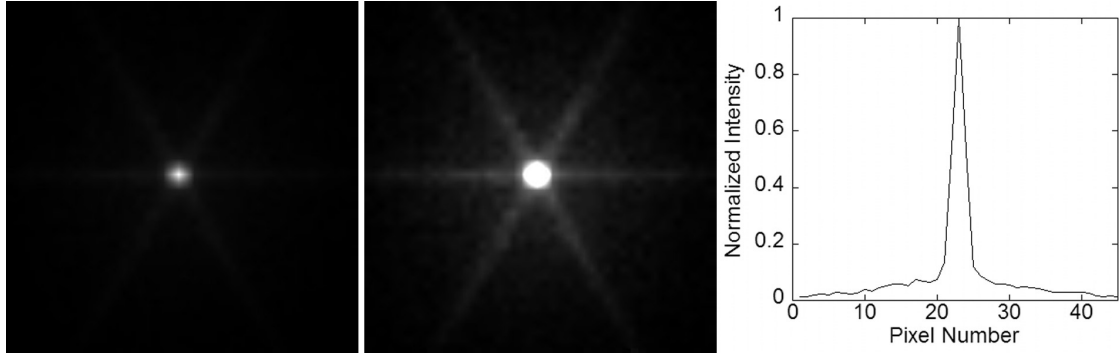

Fig. 14. GATE simulation of a point source and our parallel hole collimator without windowing (left), windowed to 25% of the maximum pixel intensity (middle), and a horizontal profile (right). The septal penetration star pattern is clearly seen in the windowed image.

Fig. 15. GATE simulation of a point source and the pinhole hole collimator without windowing (left), windowed to 25% of the maximum pixel intensity (middle), and a horizontal profile (right). Notice that there are penetration photons but there is no star pattern.

We fabricated a pinhole collimator for the mobile system based on the simulation studies and have performed for the first time acquisitions with the thorax phantom using the pinhole collimator. A photograph of the pinhole collimator is shown in Fig. 16. The objective was to compare the image quality from the pinhole collimator with that from the high energy, parallel hole collimator. Figure 17 shows a projection image of the thorax phantom, with radioactivity only in the cardiac insert, for the high-energy parallel hole collimator (left) and the pinhole collimator (right). Relative to the parallel hole collimator,

the pinhole collimator is able to reduce the low intensity outside of the cardiac region, which is due to the unwanted detection of photons that penetrate the collimator wall. We anticipate that this will result in improved reconstructed image quality with the pinhole collimator.
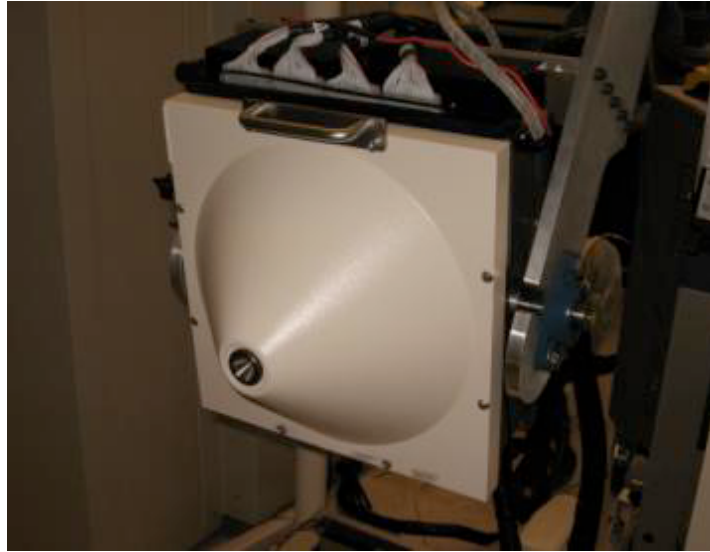

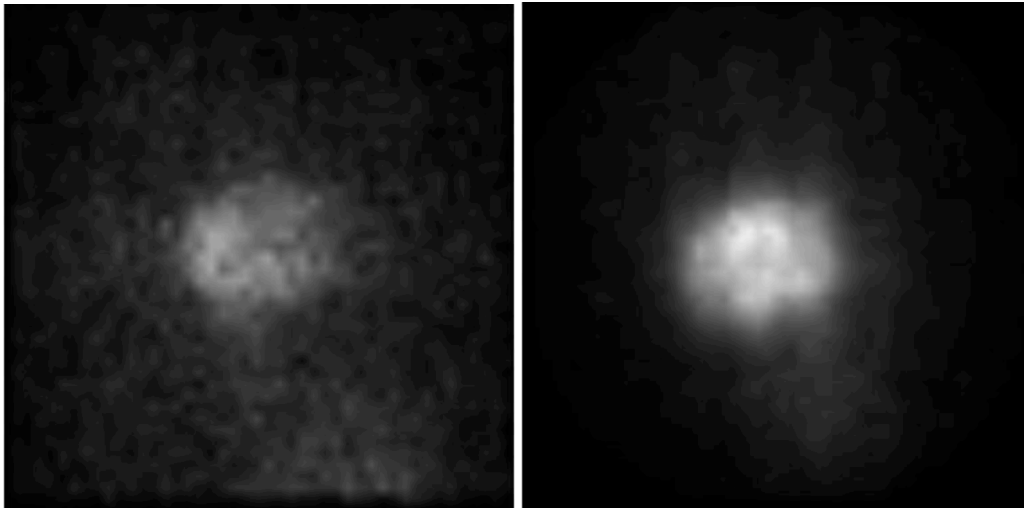Fig. 16. Pinhole collimator for mobile system

Fig. 17. Projection images from the thorax phantom (activity only in the cardiac region) using the high-energy, parallel hole collimator (left) and the pinhole collimator (right).

3. Key Research Accomplishments

I. SIMULATION STUDIES
- Development of software simulation tools
  - Analytical projection data simulator
  - Novel method for efficiently incorporating collimator effects into SPECT simulation program
  - Validation of collimator simulation using cardiac phantoms
- Validation of imager design by simulation
  - PET coincidence acquisition with two detector positions
  - SPECT acquisition with high energy collimation

II. GANTRY DESIGN AND CONSTRUCTION
- Completed CAD design
- Completed gantry construction
- Evaluation of gantry mechanical performance using mock detectors in the environment of an intensive care unit bed.

III. DETECTOR DESIGN AND CONSTRUCTION
- Initial validation of key detector sensor components:
- Designing and testing of first fast readout prototype including FPGA array cards, carrier board cards and quality control software
- Fabrication of prototype detector consisting of pixilated NaI scintillator (25 cm x 25 cm) and 4x4 array of position sensitive photomultiplier tubes.
- Evaluation with Na-22 flood field showed satisfactory pixel separation and energy resolution

IV. IMAGE RECONSTRUCTION DEVELOPMENT
- Generalized 3D iterative PET reconstruction for compact detectors
- Deconvolution of septal penetration effects for SPECT images

V. SYSTEM INTEGRATION
- Successful mechanical performance evaluation with detectors mounted to gantry
- Initial flood field measurements performed

VI. SYSTEM EVALUATION PERFORMANCE EVALUATION WITH PHANTOMS
- Completed study on basic performance measurements of imaging system including spatial resolution, sensitivity, energy resolution and count rate capability.
- Evaluated imaging performance using a cardiac thorax phantom and compared image quality with a commercial SPECT system
- Completed study on imaging performance using a cardiac thorax phantom including simulated perfusion defects.
-

VII. PINHOLE COLLIMATOR DESIGN AND EVALUATION
- Designed and evaluated by simulation a pinhole collimator for high energy SPECT imaging with the mobile system.
- Pinhole collimator was fabricated for the mobile system and the performance was evaluated using an experimental thorax phantom.

VII. CLINICAL EVALUATION
- Obtained human subjects research approval by University of Florida Institutional Review Board and U.S. Army Medical Research and Materiel Command (USAMRMC), Office of Research Protections (ORP), Human Research Protection Office (HRPO)
- A clinical evaluation of the mobile system was performed based on SPECT sestamibi imaging, and the images obtained from the mobile were of comparable in terms of image quality to images obtained from a conventional SPECT camera.

4. Reportable Outcomes

The peer-reviewed journal papers and conference proceedings listed below are included as appendices in this report.

4.A Peer-reviewed Journal Papers

1. Studenski MT, Gilland DR, Parker JG, Majewski S, Hammond W, Weisenberger A, Popov V. Performance evaluation of a bedside cardiac SPECT system, *Transactions on Nuclear Science*, 56:625-632, 2009. **(APPENDIX 1)**
2. Studenski MT, Gilland DR, Cebula, A. Acquisition and processing methods for a bedside cardiac SPECT imaging system. *Transactions on Nuclear Science*, 57:206-213, 2010. **(APPENDIX 2)**

4.B Conference Proceedings

1. Tipnis U, Gilland DR, Smith MF, Drane WE, Majewski S. Design of a compact, mobile PET detector for bedside cardiac imaging. 2003 IEEE Nuclear Science Symposium Conference Record, 19-25 Oct, 2003, vol. 4, pp. 2438-2441. **(APPENDIX 3)**
2. Tipnis U, Smith MF, Turkington TG, Wilson J, Majewski S, Gilland DR. A simulation study of a bedside cardiac PET imager. 2004 IEEE Nuclear Science Symposium Conference Record, 16-22 Oct, 2004, vol. 5, pp. 3126-3129. **(APPENDIX 4)**
3. Studenski MT, Parker JG, Gilland DR, Majewski S, Hammond B. Performance evaluation of a small field-of-view, mobile PET/SPECT system. *2007 IEEE Nuclear Science Symposium Conference Record*, 26 Oct. – 3 Nov., vol. 5, pp. 3770-3, 2007. **(APPENDIX 5)**
4. Weisenberger AG, Majewski S, Gilland DR, Hammond W, Kross B, Popov V, Proffitt J, Mckisson J, Smith MF, Zorn C. Implementation of a mobile cardiac PET imager for the emergency room and intensive care unit. *2007 IEEE Nuclear Science Symposium Conference Record*, 26 Oct. – 3 Nov., vol. 5, pp. 3705-8, 2007. **(APPENDIX 6)**

4.C Presentations at Scientific Meetings

1. Tipnis U, Gilland DR, Smith MF, Drane WE, Majewski S. Design of a compact, mobile PET detector for cardiac imaging. Presented at the IEEE 2003 Nuclear

Science Symposium and Medical Imaging Conference, October 22-25, 2003, Portland, OR.

2. Dingley J, Tipnis UJ, Gilland DR. Cardiac 511 keV SPECT simulation with a compact detector design. Presented at: 2005 Nuclear Science Symposium and Medical Imaging Conference, October 23-29, Fajardo, Puerto Rico.

3. Majewski S, Gunning W, Hammond W, Kross B, Smith M, Popov V, Proffitt J, Weisenberger A, Wojcik R, and Gilland D. Development and Evaluation of Detector Heads and Readout for a Mobile Cardiac Imager System, Presented at: 2006 IEEE Nuclear Science Symposium and Medical Imaging Conference, Oct. 29 – Nov. 3, San Diego, CA.

4. Studenski MT, Parker JG, Gilland DR, Majewski S, Hammond B. Performance evaluation of a small field-of-view, mobile PET/SPECT system. Presented at: 2007 IEEE Nuclear Science Symposium and Medical Imaging Conference, Oct. 27 – Nov. 3, Honolulu, HI.

5. Weisenberger AG, Majewski S, Gilland DR, Hammond W, Kross B, Popov V, Proffitt J, Mckisson J, Smith MF, Zorn C. Implementation of a mobile cardiac PET imager for the emergency room and intensive care unit. Presented at: 2007 IEEE Nuclear Science Symposium and Medical Imaging Conference, Oct. 27 – Nov. 3, Honolulu, HI

6. Studenski MT, Gilland DR, Parker JG. A Small Field-of-View, Mobile PET/SPECT System for Bedside Environments: A Dynamic Cardiac Phantom Study using 99mTc and 18F-FDG. Presented at the American Association of Physicists in Medicine 50th Annual Meeting, July 27-31, 2008, Houston, TX.

7. Studenski MT, Gilland DR. Acquisition and Processing Methods for a Bedside Cardiac SPECT Imaging System. Presented at the IEEE 2008 Nuclear Science Symposium and Medical Imaging Conference, October 18-25, 2008, Dresden, Germany.

8. Cebula A, Studenski MT, Samarin A, Gilland DR, Evaluation of a Bedside SPECT Imaging System based on Myocardial Defect Detection. Presented at 2009 IEEE Nuclear Science Symposium and Medical Imaging Conference, Oct. 25-31, 2009.

9. Cebula A, Studenski MT, Gilland DR, Bedside SPECT Imaging with pinhole collimation. Accepted to the 52nd Annual Meeting of American Association of Physicists in Medicine, July 18-22, 2010, Philadelphia, PA.

5. Conclusions

A compact and mobile imaging system has been fabricated and undergone pre-clinical and clinical evaluation at the University of Florida. The system is unique in its ability to do both SPECT and PET imaging at the patient bedside. Incorporated into the system are customized detectors that have been built within a compact housing and with high count rate capability. The detectors are mounted on a gantry that provides portability and positioning capability for tomographic imaging. Basic performance measures—including spatial resolution, system sensitivity, and count rate capability—were performed and met design specifications. Reconstructed image quality was assessed using anthropomorphic phantoms and found to be satisfactory. In the clinical evaluation, the images from the mobile system compared favorably with images obtained from the same patients using conventional imaging systems.

6. References

1. Website: http://www-lphe.epfl.ch/~PET/research/gate
2. Ljungberg M. The SIMIND Monte Carlo program. In "Monte Carlo Calculation in Nuclear Medicine: Applications in Diagnostic Imaging", Ljungberg M, Strand S-E, King MA, eds.), pp. 145-163. IOP Publishing, Bristol and Philadelphia.
3. M.F. Smith, S. Majewski, A.G. Weisenberger, D.A. Kieper, R.R. Raylman, T.G. Turkington. Analysis of factors affecting positron emission mammography (PEM) image formation. IEEE Transactions on Nuclear Science, vol. 50 (1), Feb. 2003, pp. 53-59.

7. Appendices

Appendices Summary

Appendix #   Content
1   Studenski MT, Gilland DR, Parker JG, Majewski S, Hammond W, Weisenberger A, Popov V. Performance evaluation of a bedside cardiac SPECT system, *Transactions on Nuclear Science*, 56:625-632, 2009.

2   Studenski MT, Gilland DR, Cebula, A. Acquisition and processing methods for a bedside cardiac SPECT imaging system. *Transactions on Nuclear Science*, 57:206-213, 2010.

3   Tipnis U, Gilland DR, Smith MF, Drane WE, Majewski S. Design of a compact, mobile PET detector for bedside cardiac imaging. 2003 IEEE Nuclear Science Symposium Conference Record, 19-25 Oct, 2003, vol. 4, pp. 2438-2441.

4   Tipnis U, Smith MF, Turkington TG, Wilson J, Majewski S, Gilland DR. A simulation study of a bedside cardiac PET imager. 2004 IEEE Nuclear Science Symposium Conference Record, 16-22 Oct, 2004, vol. 5, pp. 3126-3129.

5   Studenski MT, Parker JG, Gilland DR, Majewski S, Hammond B. Performance evaluation of a small field-of-view, mobile PET/SPECT system. *2007 IEEE Nuclear Science Symposium Conference Record*, 26 Oct. – 3 Nov., vol. 5, pp. 3770-3, 2007.

6   Weisenberger AG, Majewski S, Gilland DR, Hammond W, Kross B, Popov V, Proffitt J, Mckisson J, Smith MF, Zorn C. Implementation of a mobile cardiac PET imager for the emergency room and intensive care unit. *2007 IEEE Nuclear Science Symposium Conference Record*, 26 Oct. – 3 Nov., vol. 5, pp. 3705-8, 2007.

Performance Evaluation of a Bedside Cardiac SPECT System

Matthew T. Studenski, *Student Member, IEEE*, David R. Gilland, *Member, IEEE*, Jason G. Parker, B. Hammond, Stan Majewski, Andrew G. Weisenberger, and Vladimir Popov

Abstract—**This paper reports on the initial performance evaluation of a bedside cardiac PET/SPECT system. The system was designed to move within a hospital to image critically-ill patients, for example, those in intensive care unit (ICU) or emergency room settings, who cannot easily be transported to a conventional SPECT or PET facility. The system uses two compact (25 cm × 25 cm) detectors with pixilated NaI crystals and position sensitive PMTs. The performance is evaluated for both 140 keV (Tc-99m) and 511 keV (F-18) emitters with the system operating in single photon counting (SPECT) mode. The imaging performance metrics for both 140 keV and 511 keV included intrinsic energy resolution, spatial resolution (intrinsic, system, and reconstructed SPECT), detection sensitivity, count rate capability, and uniformity. Results demonstrated an intrinsic energy resolution of 31% at 140 keV and 23% at 511 keV, a planar intrinsic spatial resolution of 5.6 mm full width half-maximum (FWHM) at 140 keV and 6.3 mm FWHM at 511 keV, and a sensitivity of 4.15 counts $\cdot \mu Ci^{-1} \cdot s^{-1}$ at 140 keV and 0.67 counts $\cdot \mu Ci^{-1} \cdot s^{-1}$ at 511 keV. To further the study, a SPECT acquisition using a dynamic cardiac phantom was performed, and the resulting reconstructed images are presented.**

Index Terms—**Cardiac SPECT, mobile SPECT, 511 keV SPECT.**

I. INTRODUCTION

THIS paper reports on the initial performance evaluation of a bedside cardiac PET/SPECT system. The system was designed to move within a hospital to image critically-ill patients, for example, those in intensive care unit (ICU) or emergency room settings, who cannot easily be transported to a conventional SPECT or PET facility. In these settings, patients with known or suspected severe coronary artery disease typically must be managed without the benefit of myocardial perfusion or viability imaging studies. Although portable cardiac SPECT systems are currently commercially marketed,[1] the system described here is unique in its design to image critically-ill patients lying supine in ICU or emergency room beds.

An additional unique feature of this system is the capability of imaging both Tc-99m and positron (e.g. F-18) emitting tracers. The complementary information provided by Tc-99m perfusion tracers and F-18 viability tracers give a more complete assessment of the extent of cardiac disease. While this two detector system is capable of operating in PET coincidence mode, in this study we investigate the 511 keV SPECT approach using high energy collimation. In the context of bedside imaging, the 511 keV SPECT approach, using an anterior 180 degree detector orbit, has the advantage of not requiring a detector to be positioned beneath the patient bed where detector movement is often obstructed. Clearly, the disadvantage of this approach is the reduced sensitivity of absorptive, compared with electronic, collimation.

A mobile imaging system of this nature cannot be expected to achieve the same image quality of conventional SPECT or PET systems, particularly when the mobile system is designed for both 140 keV and 511 keV imaging. Our design goal was to achieve an economical design that is capable of detecting moderate to severe myocardial defects in patients, not to try to match conventional imaging systems in terms of performance capabilities. For example, the targeted spatial resolution for this system was 1.5–2.0 cm in the reconstructed image. Conventional systems can achieve better spatial resolution (and other performance parameters), but these systems are often not a viable option for patients in an ICU or emergency room.

II. SYSTEM DESIGN

The mobile system consists of two compact detectors, each with approximately 25×25 cm^2 detector area, mounted on a mobile gantry system with a detachable computer and electronics rack (Fig. 1). The detectors (fabricated at Thomas Jefferson National Accelerator Facility [1]) consist of pixilated NaI(Tl) ($5.0 \times 5.0 \times 12.5$ mm^3 with 5.5 mm pitch). The reduced detection efficiency for 511 keV from the 12.5 mm thick NaI crystal is a concern, but we anticipate that this can be partially compensated by longer scan times in ICU applications. The photomultiplier tube (PMT) readout uses position-sensitive PMTs with high-rate four analog outputs arranged in a 4 × 4 array for each detector to form the 25×25 cm^2 active detector area. A detailed description of the detector electronics and signal processing can be found in [1].

M. T. Studenski is with the Nuclear and Radiological Engineering Department, University of Florida, Gainesville, FL 32611 USA (e-mail: mstudens@ufl.edu).

D. R. Gilland is with the Nuclear and Radiological Department and the Biomedical Engineering Department, University of Florida, Gainesville, FL 32611 USA (e-mail: gilland@ufl.edu).

J. G. Parker is with the Innovation Center, Kettering Health Network, and the Biomedical Engineering Department, Wright State University, Dayton, OH 45402 USA (e-mail: Jason.Parker@khnetwork.org; parkej@ufl.edu).

B. Hammond is with the Material Science and Engineering Department, University of Florida, Gainesville, FL 32611 USA (e-mail: whmmond@gmail.com).

S. Majewski, A. G. Weisenberger, and V. Popov are with the Detector Group, Thomas Jefferson National Accelerator Facility, Newport News, VA 23606 USA (e-mail: majewski@jlab.org; drew@jlab.org; popov@jlab.org).

[1]For example, Segami Corporation, "Nomad" system.

Fig. 1. Photograph of bedside cardiac imaging system. Detectors are shown in left lateral and right anterior oblique orientations. Associated electronics rack and computers shown at right.
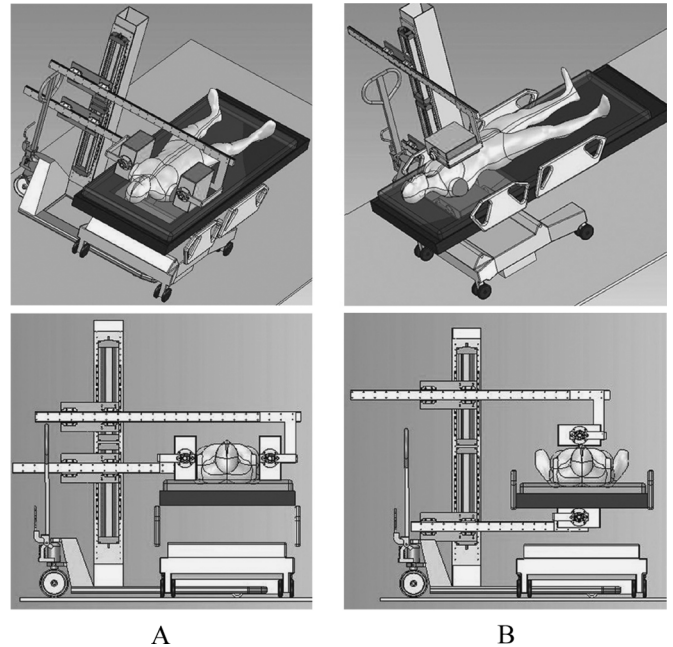

Fig. 2. Computer-aided design drawings of the system gantry and the different detector positioning capabilities. (A) Lateral view. (B) Anterior/posterior view. Notice that the ICU bed arms move up and down to allow for detector positioning.

The custom manufactured gantry system[2] has been designed to position the detectors for tomographic imaging under the challenging conditions imposed by the ICU or emergency room settings. The gantry has low profile legs that slide beneath ICU beds for stable support, as shown in the computer-aided design drawings in Fig. 2. The detectors mount to the rails of a linear bearing set that allows precise horizontal and vertical detector motion. Vertical detector motion is motor-driven using electronic motion control modules. Detector pivoting provides the additional, necessary motion dimension for tomographic imaging. The linear motions and pivot angle are digitally encoded for input to the reconstruction software.

This paper reports on the performance evaluation of this imaging system operated in single photon detection mode (SPECT) for both 140 keV and 511 keV imaging. Although this system is capable of acquiring coincidence PET data from the two detectors in opposing orientation [Fig. 2(a) and (b)], the 511 keV SPECT approach, using high energy collimators and acquiring projections over the anterior 180°, has advantages in this context despite the reduced detection sensitivity from the high energy collimators. First, projection data with complete angular sampling (anterior 180°) are more readily achieved in SPECT mode than in PET mode due to the obstruction of detector movement beneath the patient bed in PET mode. A PET acquisition using two static detector orientations [lateral in Fig. 2(a) and anterior/posterior in Fig. 2(b)] may be used; however, our earlier studies showed that this limited angle projection data results in reconstruction artifacts [2]. Second, due to the superficial position of the heart to the anterior chest wall, the effects of attenuation and scatter in the patient body are greatly reduced with 511 keV SPECT for cardiac imaging using 180° anterior data relative to PET.

III. EVALUATION METHODS

Five imaging performance metrics were evaluated for both 140 keV and 511 keV imaging with this system: intrinsic energy

resolution, spatial resolution (planar and reconstructed SPECT), detection sensitivity, count rate capability, and uniformity.

A. Energy Resolution

The energy resolution of the system was measured intrinsically (without collimator) with a point source positioned 75 cm from the detector face and 1.0×10^7 total counts acquired for each source. Using this geometry, energy spectra of the point sources were obtained. An 80 μCi source of Tc-99m (140 keV) was imaged at the detector's low energy setting and a 240 μCi source of F-18 (511 keV gamma) was imaged at the high energy setting. These radioactivity levels were low enough to ensure that the detector did not exceed the maximum count rate.

To determine a keV/channel calibration factor for each energy setting, a 5 μCi source of Co-57 (122 keV gamma) was imaged at the low energy setting and a 65 μCi source of Cs-137 (662 keV gamma) was imaged at the high energy setting. The peak channel for each of these sources was recorded and a keV/channel factor was obtained for each energy setting by comparing the peak channels of the two different sources at each respective energy setting. This calibration factor was used to convert the measured energy resolution (FWHM in channels) into keV units. The photopeak FWHM was measured without curve fitting due to the low noise and fine sampling (channel width less than FWHM/100) of the energy spectrum. The maximum was taken to be the peak value and the full-width was found by linear interpolation of the two closest half maximum channels on each side of the photopeak.

B. Spatial Resolution

The intrinsic planar spatial resolution of the system at 140 keV and 511 keV was measured using a 5 cm thick,

	Low Energy	High Energy
Hole Shape	hexagonal	hexagonal
Collimator Thickness [cm]	2.3	4.9
Hole Diameter [mm]	1.5	2.3
Septal Thickness [mm]	0.2	2.02

1 mm wide lead slit phantom with Tc-99m (190 μCi) and F-18 (160 μCi) point sources. The sources were positioned 75 cm from the detector face, and 5.0×10^6 counts were obtained for both energies. Count rate was substantially below the system maximum. The intrinsic spatial resolution was measured and averaged over three acquisitions with the slit phantom translated in 1 mm increments perpendicular to the slit. This was done in order to average out potential variation in the measured spatial resolution due to the position of the slit position relative to the detector grid.

The system planar spatial resolution at 140 keV and 511 keV was evaluated using low and high energy collimators, respectively. The collimator parameters are given in Table I. The theoretical septal penetration level for the high energy collimator at 511 keV is 7% using the formula from [3], which is slightly greater than the conventionally used level of 5%.

Line source images were acquired using 1 mm inner diameter capillary tubes containing either 500 μCi of Tc-99m or 200 μCi of F-18 with an energy window of 30% for Tc-99m and 20% for F-18. Images with 5.0×10^5 total counts were obtained at distances of 10 cm, 20 cm, and 30 cm from the collimator face and in both x and y orientations. Profiles were taken across the images to obtain line spread functions (LSF) at each distance, and the FWHM was measured. For the 511 keV case, the FWHM was measured both with and without subtracting a constant from the LSF to reduce the effect of the septal penetration "tails" in the measured LSF. This constant, 0.18, was computed from the average intensity of twenty pixels not contained in the peak. The reported FWHM was the average of the x and y directions. These results were then compared to the theoretical FWHM calculated using the effective length and diameter of the collimator holes and the distance from the collimator face [3]. In order to assess the level of septal penetration in the line source images, the full-width-tenth-maximum (FWTM) was also measured. Uniformity correction was applied to all the images acquired for spatial resolution measurements.

The reconstructed SPECT spatial resolution at 140 keV was measured using a point source of Tc-99m (2.5 mCi) located at the tip of a syringe. The same measurement was performed at 511 keV using 250 μCi of F-18. A total of 19 projections (every 10° from 0°–180°) with 5.0×10^5 counts per projection and a 20% energy window were obtained. The activity in the syringe was centered in the detector field-of-view with a radius of rotation of 22 cm. The projections were reconstructed using MLEM [4] with 50 iterations into a $45 \times 45 \times 45$ voxel image (5 mm voxel). The iterative MLEM reconstruction algorithm was used because we have found this method to be superior to filtered

backprojection with ramp filter in terms of reducing streak artifacts when projection angular sampling is somewhat coarse, as in this case. The system model within the MLEM algorithm assumed ideal spatial resolution, so there was not any spatial resolution enhancement through image processing. The number of iterations, 50, was chosen based on the fact that the change in the reconstructed spatial resolution at greater iteration numbers was negligible. A profile was taken across a transaxial and coronal slice of the reconstructed image and from this, the FWHM was measured.

The effect of projection angle sampling was not studied. Theoretically, it has been noted that the required number of angular samples changes linearly with the linear sampling distance and inversely with the field-of-view (FOV) size [5]. Comparing the FOV of this system (25 cm) to that of a traditional system (typically 50 cm), the required number of angular samples with this system is reduced by a factor of two relative to a traditional SPECT system.

C. Detection Sensitivity

The extrinsic (with collimator) detection sensitivity in terms of counts $\cdot \mu Ci^{-1} \cdot s^{-1}$ was evaluated using point sources of 240 μCi Tc-99m and 170 μCi F-18 suspended 15 cm from the collimator face. Each acquisition was 300 s with an energy window twice the width of the FWHM of the photopeak. For the Tc-99m case, the measured sensitivity was obtained by summing the counts over the entire detector surface. For the F-18 case, in order to get a more meaningful measure of sensitivity that excluded uncollimated photons, the measured sensitivity was obtained by summing over a 35 cm^2 circular region-of-interest (ROI) centered on the peak image intensity. This ROI was chosen subjectively; in practice it is impossible to eliminate all penetrating photons while including all collimated photons with a single ROI. To quantify the effect of different ROI sizes on the sensitivity measurement, a second, 45 cm^2 circular ROI was also measured.

To investigate the non-uniformity in detection sensitivity over the detector surface, the sensitivity measurements for both energies were obtained with the point sources located at five different positions across the detector field-of-view. The positions were chosen in an attempt to sample the full range of sensitivity variation based on the detector count rate readout.

A discrepancy was observed between the predicted and measured sensitivity for the Tc-99m case. In order to further investigate this effect, additional detection sensitivity measurements were performed with Tc-99m using the high energy collimator.

D. Count Rate Capability

The detector count rate performance for 140 and 511 keV was evaluated using point sources with 535 μCi of Tc-99m and 1.1 mCi of F-18. Each source was suspended 30 cm from the detector face and 20 s acquisitions were obtained while the source decayed through several half lives. The counts per second (cps) minus background integrated over the entire detector surface was recorded at each time point. For this acquisition no out-of-field activity was used.
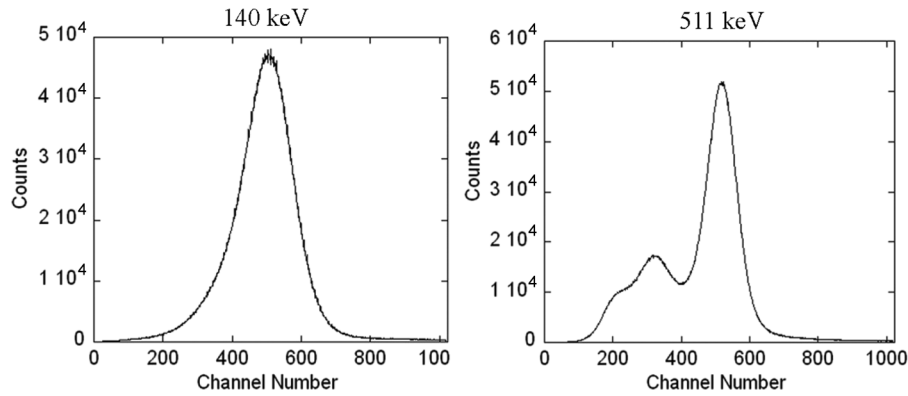
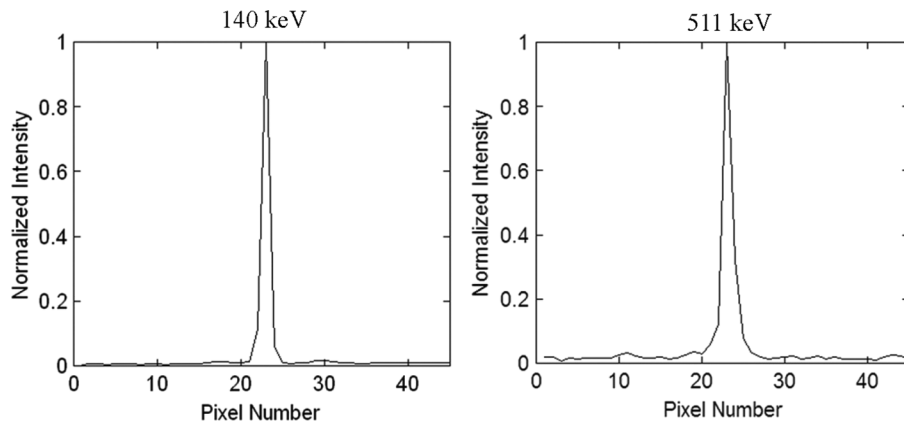Fig. 3.   Energy spectra obtained from 140 keV and 511 keV point sources.

Fig. 4.   Normalized intrinsic spatial resolution LSFs with Tc-99m and F-18.

E. Flood Field Uniformity

Flood field uniformity was evaluated using the images that resulted from the energy resolution measurements (Section III-A). The images are presented both with and without linearity correction. The linearity-corrected flood image is used for uniformity correction in the measured projection images.

F. Phantom Acquisition

The performance of this system was further assessed based on SPECT image quality using an anthropomorphic, dynamic cardiac phantom.[3] The phantom contains simulated lungs, spine, liver, and myocardium. Both Tc-99m and F-18 studies were performed using approximately 1 mCi injected into the simulated myocardium. There was no activity placed outside of the myocardium. The phantom heart rate was 72 beats per minute; the ejection fraction was 45%. As with the previous SPECT acquisitions, 19 projections were acquired with 2.5×10^5 counts per projection, which resulted in approximately 35 minute scan time. The energy window was 30% for Tc-99m and 20% for 511 keV.

IV. RESULTS

A. Energy Resolution

The energy spectra from the Tc-99m and F-18 images can be seen in Fig. 3. Using the calculated keV/channel fac-

---

[3]Model ECT/DY-CAR/P, Data Spectrum Corp. Hillsborough, NC, 27278.

tors (0.27 keV/channel at 140 keV and 1.00 keV/channel at 511 keV), the measured FWHM was 43 keV (31%) for 140 keV and 108 keV (23%) for 511 keV. Low energy tails are absent from the Tc-99m spectrum, and the photopeak is asymmetric. We suspect that this is due to the fact that the energy discrimination with this detector has been optimized for 511 keV and that a low energy cutoff is affecting photons in the lower half of the photopeak, between approximately 100 keV and 140 keV.

B. Spatial Resolution

The intrinsic spatial resolution was measured to be 5.6 mm FWHM at 140 keV and 6.3 mm FWHM at 511 keV. Fig. 4 shows the normalized LSFs from the slit phantom images. Because the face of the detector was completely shielded except for the slit, we suspect the cause of the low intensity tails in the 511 keV LSF are from photons that penetrate through the lead in the slit phantom.

Fig. 5 shows the normalized system spatial resolution LSFs from the capillary tube acquisitions at 140 keV and 511 keV. Each plot includes the measurements at 10, 20 and 30 cm from the detector face. For both energies, plots are shown for the x and y profile directions. The tails in the 511 keV LSFs can be attributed to collimator septal penetration.

Fig. 6 shows line source images acquired at 10 cm from the detector face for both 140 keV and 511 keV. The effects of septal penetration are evident in the 511 keV image in the region surrounding the line source. The septal penetration pattern is con-
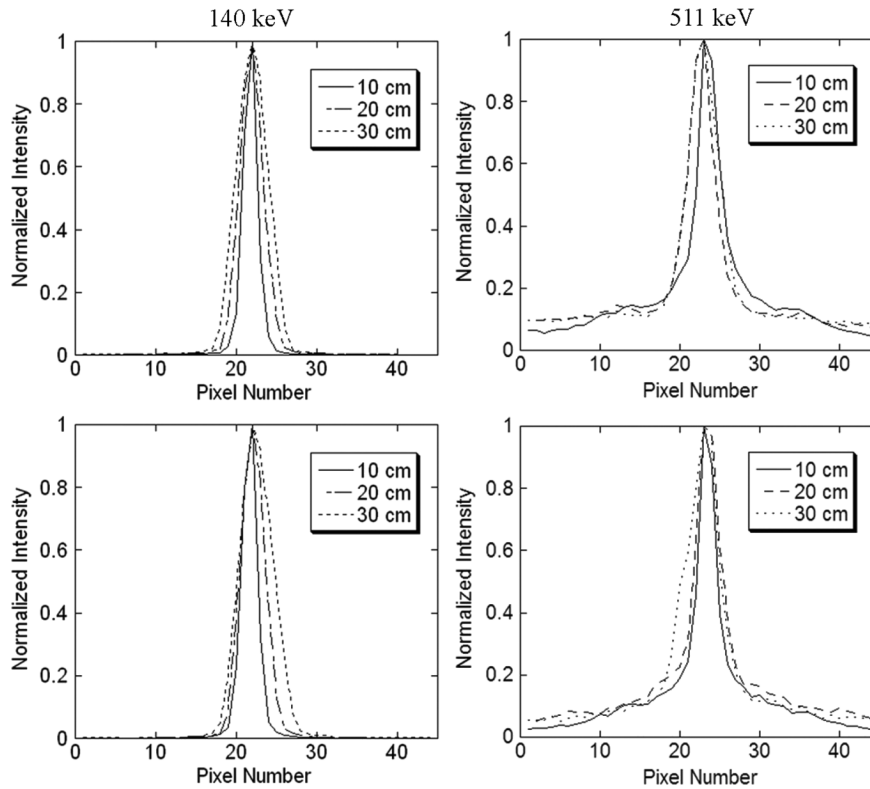
Fig. 5. Normalized system spatial resolution LSFs at 10, 20, and 30 cm from the detector face for both 140 keV and 511 keV. For both energies, LSF's are shown in the x direction (top row) and the y direction (bottom row).

TABLE II
SYSTEM SPATIAL RESOLUTION

| Energy | b [cm] | FWHM [cm] | | | | FWTM [cm] |
		w/o Subtraction	With Subtraction	Theoretical	% Deviation	
140 keV	10	1.14	-	0.99	14.7	2.16
	20	1.64	-	1.59	3.1	3.16
	30	2.35	-	2.23	5.4	4.12
511 keV	10	1.52	1.23	1.05	44.8 / 17.1	12.06
	20	2.04	1.68	1.59	28.3 / 5.7	13.42
	30	2.47	2.10	2.06	19.9 / 1.9	13.62
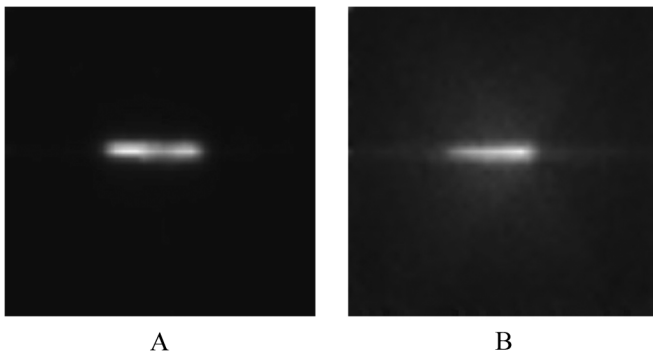
Fig. 6. Line source images for system spatial resolution measurements. (A) 140 keV. (B) 511 keV. Line source to detector distance was 10 cm.

sistent with the commonly observed, six point star artifact with hexagonal hole collimators [6].

Table II summarizes the measured FWHM as a function of distance from the collimator ("b"), both with and without constant subtraction, and the theoretical calculation and the percent deviation of the measured from the theoretical. The table shows that the tails from septal penetration caused substantial increase in the measured FWHM and a closer agreement with the theoretical spatial resolution occurred after subtracting the constant. Table II also shows the FWTM results in which the effect of septal penetration with 511 keV photons is evident in the larger FWTM values.

Fig. 7 shows the reconstructed SPECT image of the point source and the corresponding LSF obtained by integrating the intensity along columns in the image (and normalizing). The FWHM of the LSF at 140 keV was 1.59 cm in the transaxial plane and 1.57 cm in the coronal plane. This is in close agreement with the theoretical, planar system spatial resolution (1.59 cm), which is obtained using the standard formula from
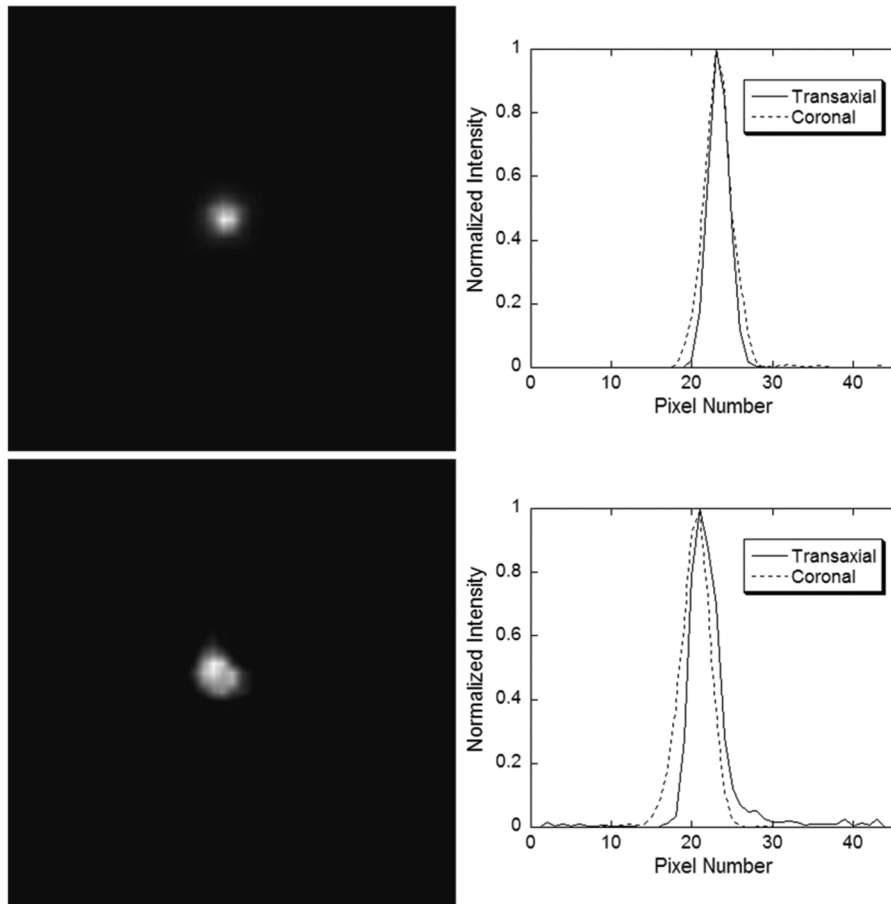
Fig. 7. Reconstructed coronal SPECT slice from a 140 keV (top row) and 511 keV (bottom row) point source and its corresponding point spread functions in both the transaxial and coronal planes.

[3] for the low energy collimator at a distance from the collimator face equal to the radius of rotation used in the SPECT acquisition. For the 511 keV source, the FWHM was 1.58 cm in the transaxial plane and 1.74 cm in the coronal plane. These values also agree well with the theoretical resolution (1.59 cm).

C. Detection Sensitivity

Table III contains the results from the sensitivity measurements along with the predicted sensitivity calculated from geometric collimator efficiency "g" [3] and intrinsic crystal efficiency at both energies. To show the effect of the sensitivity non-uniformity over the detector surface, both the minimum and maximum values from the five measurements are included in the table. The measurements using F-18 have two values from the two different sized ROIs; the first value is the sensitivity from the 35 cm² ROI and the second value is from the 45 cm² ROI.

The 511 keV measurements compared well with the predicted values. Some of the measured values were actually higher than the predicted values, which we suspect is due to the inclusion of uncollimated photons in the measurement. The 140 keV measurements are lower than predicted for both the low and high energy collimators. This discrepancy can largely be attributed to the reduced sensitivity in the regions between PMT's, which is represented by the minimum measured sensitivity in Table III.

TABLE III
SYSTEM SENSITIVITY

Source Energy and Collimator	Predicted [cts/μCi/s]	Measured [cts/μCi/s]		
		Min.	Max.	Avg.
140 keV w/ low energy	8.57	1.73	6.06	4.15
140 keV w/ high energy	1.55	0.30	0.92	0.55
511 keV w/ high energy	0.92	0.40 / 0.93	0.87 / 1.14	0.67 / 1.06

D. Count Rate Capability

Fig. 8 shows plots of the detected count rate as a function of activity for Tc-99m and F-18. The maximum count rate in both of these curves was found near the left end of the plateau of these curves. The presence of a plateau is unlike the count rate curve of a typical paralyzeable detector, which exhibits a more clearly defined maximum. The maximum count rate was measured to be 1.46×10^5 cps for Tc-99m and 1.56×10^5 cps for F-18. This maximum occurred at 135 μCi for Tc-99m and 275 μCi for F-18. The images and energy spectra were distorted when the detector count rate was saturated.

E. Flood Field Uniformity

Fig. 9 shows the uncorrected raw flood images acquired at both 140 and 511 keV, and Fig. 10 shows the flood images after
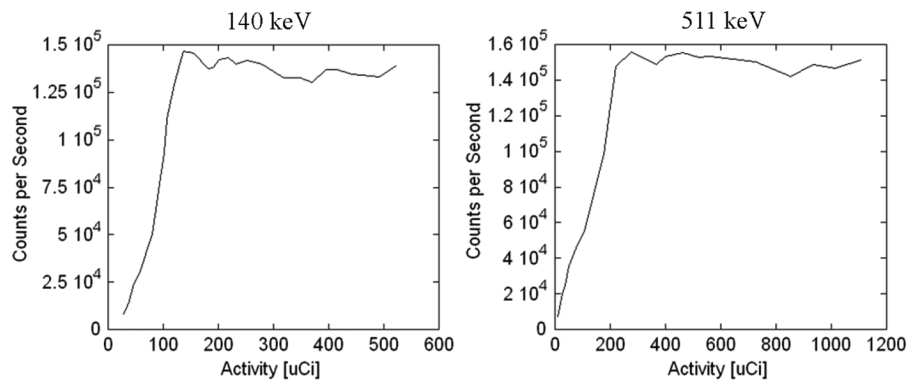
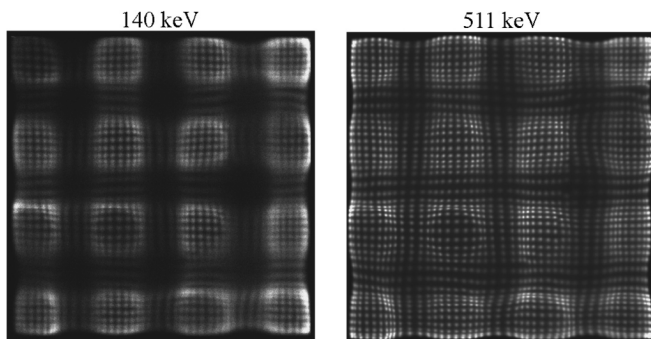Fig. 8. Count rate as a function of activity for 140 keV and 511 keV.

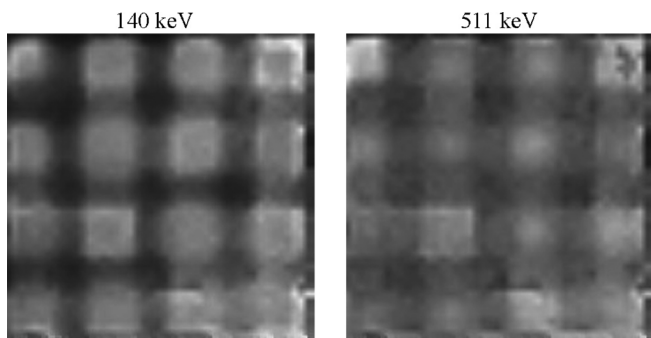Fig. 9. Raw, uncorrected flood images for both 140 keV and 511 keV energies.

Fig. 10. 45 × 45 pixel linearity corrected flood images for both 140 keV and 511 keV energies used to correct for uniformity in acquired images.
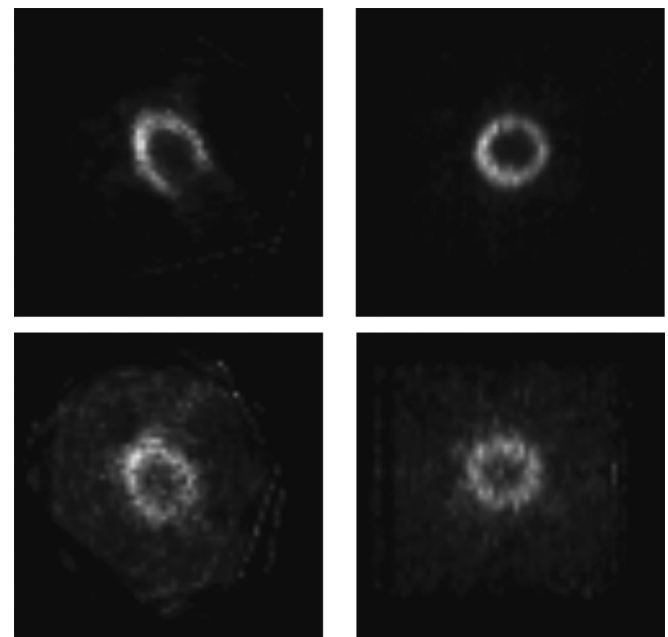

Fig. 11. Reconstructed transaxial (left column) and coronal (right column) slices from the dynamic cardiac phantom acquisition with Tc-99m (top row) and F-18 (bottom row).

linearity correction. The 4 × 4 array of PMTs and the 45 × 45 pixel array can clearly be seen in the images. The degree of non-uniformity between the low intensity regions (between PMTs) and high intensity regions (within PMTs) is perhaps best quantified by the detection sensitivity minimum and maximum presented in Table III. For 140 keV, the minimum and maximum regions differ by a factor of approximately 3.5; for 511 keV, they differ by a factor of approximately 2.

F. Phantom Acquisition

Fig. 11 shows the reconstructed myocardium of the dynamic cardiac phantom in transaxial and coronal slices for the Tc-99m and F-18 acquisitions. The F-18 images show artifacts in the form of extra-myocardial image intensities, which can be attributed to septal penetration effects. These effects result in a lower ventricle-to-myocardium contrast when compared to the Tc-99m images, as found previously [6]. Further studies will be performed with the phantom to assess the effects of out-of-field activity, angular sampling, and counts per projection; these issues are important for the environment in which we expect to use this system.

V. SUMMARY AND DISCUSSION

This paper presents the results of a basic performance evaluation of a compact, mobile PET/SPECT system designed for bedside imaging. The performance of the system was measured for 140 keV and 511 keV in terms of energy resolution, spatial resolution (intrinsic, planar system, and reconstructed SPECT), detection sensitivity, count rate capability, and flood field uniformity.

As a mobile, bedside imager, the performance of this system is not expected, nor designed, to match that of a conventional SPECT system. The design of this camera, including pixilated NaI and position-sensitive PMT's, was chosen to allow a

compact design with effective imaging closer to the edge of the camera. This will be advantageous for future PET imaging, which will require a detector to be positioned beneath the bed. For solely anterior, 180 degree SPECT, it may be that conventional camera designs will work effectively in the bedside environment with potentially improved system performance. In spite of the inferior performance relative to conventional systems, this bedside system may still provide images of sufficient quality to aid in patient management. For example, severe cardiac disease can be readily apparent in cardiac Tc-99m and F-18-FDG images and does not necessarily require a gamma camera or PET system with ultra-high spatial resolution and detection sensitivity. The critical question of whether the performance of this system, as presented in this paper, is adequate to diagnose moderate-to-severe cardiac defects will require further study that includes experimental phantoms with realistic defects and initial patient studies.

In terms of energy resolution, the measured values (31% for 140 keV and 23% for 511 keV) were worse than typically found for conventional SPECT systems. Current systems using NaI scintillators can achieve an energy resolution of around 10% at 140 and 511 keV [8], [9], but adding a pixilated crystal and the position sensitive PMTs can degrade the resolution to 18% [10]. Other systems using LSO and BGO scintillators at 511 keV can achieve an energy resolution of about 18% and 22%, respectively [8], [10]. We are not aware of any fundamental reason why the energy resolution should be worse than a conventional gamma camera. The degraded energy resolution is expected to impact scatter rejection and, as a result, the detectability of myocardial defects to some degree.

In order to reduce costs and because ultra-high spatial resolution was not a design goal, this system uses a NaI crystal with 5 mm pixels. At a higher cost, a different material, such as CZT or LaBr$_3$: Ce with much smaller pixels could be used, which would improve both spatial resolution and energy resolution [7].

Gains could be made in the sensitivity of the system by matching the collimator pitch to the crystal pitch [11]. To reduce expenses with the system, using a traditional hexagonal hole collimator was more efficient than having a custom-made square hole collimator that matched the pixel pitch. The larger size of the pixels in this system compared to other systems was another reason to choose the traditional hexagonal collimator.

Future work will involve an evaluation of the dynamic cardiac phantom with both Tc-99m and positron emitters with out-of-field activity and myocardial defects. The effects of angular sampling and counts per projection will be tested since these factors will be important in the challenging environment of the ICU or ER. We will also work on a means of filtering the projection data to reduce septal penetration effects in the F-18 acquisitions.

REFERENCES

[1] A. G. Weisenberger, S. Majewski, and D. Gilland *et al.*, "Implementation of a mobile, cardiac PET imager for the emergency room and intensive care unit," presented at the 2007 IEEE Nucl. Sci. Symp. Med. Imag. Conf., Honolulu, HI.

[2] U. Tipnis, M. Smith, and T. Turkington *et al.*, "A simulation study of a bedside cardiac PET imager," in *2004 IEEE Nucl. Sci. Symp. Conf. Rec.*, Oct. 16–22, 2004, vol. 5, pp. 3126–3129.

[3] S. Cherry, J. Sorenson, and M. Phelps, *Physics in Nuclear Medicine*, 3rd ed.   Philadelphia, PA: Saunders, 2003.

[4] L. A. Shepp and Y. Vardi, "Maximum likelihood reconstruction in positron emission tomography," *IEEE Trans. Med. Imag.*, vol. MI-1, no. 2, pp. 113–122, 1982.

[5] H. Barrett and W. Swindell, *Radiological Imaging: The Theory of Image Formation, Detection, and Processing*.   San Diego, CA: Academic Press, 1981.

[6] C. Laymon and T. Turkington, "Characterization of septal penetration in 511 keV SPECT," *Nuc. Med. Commun.*, vol. 27, no. 11, pp. 901–909, 2006.

[7] R. Pani, R. Pellegrini, and M. N. Cinti *et al.*, "Recent Advances and future perspectives of gamma camera imagers for scintimammography," *Nucl. Instr. Meth. A*, vol. 569, pp. 296–300, 2006.

[8] L. Adam, J. Karp, and R. Freifelder, "Energy-based scatter correction for 3-D PET scanners using NaI(Tl) detectors," *IEEE Trans. Med. Imag.*, vol. 19, no. 5, pp. 513–521, May 2000.

[9] Y. Qi, B. Tsui, B. Yoder, and E. Frey, "Characteristics of compact detectors based on pixellated NaI(Tl) crystal arrays," in *2002 IEEE Nucl. Sci. Symp. Conf. Rec.*, Nov. 10–16, 2002, pp. 1538–1542.

[10] B. Pichler, T. Gremeiilion, and V. Ermer *et al.*, "Detector characterization and detector setup of a NaI-LSO PET/SPECT camera," *IEEE Trans. Nuc. Sci.*, vol. 50, no. 5, pp. 1420–1427, Oct. 2003.

[11] C. Jeanguillaume, A. Douiri, and M. Quartuccio *et al.*, "CACAO a collimation means well suited for pixellated γ-camera," in *2001 IEEE Nucl. Sci. Symp. Conf. Rec.*, Oct. 4–10, 2001, vol. 4, pp. 2291–2294.

Acquisition and Processing Methods for a Bedside Cardiac SPECT Imaging System

Matthew T. Studenski, *Member, IEEE*, David R. Gilland, *Member, IEEE*, and Alan Cebula, *Student Member, IEEE*

Abstract—We have developed a compact and mobile gamma imaging system that is designed for both PET and SPECT acquisitions within a bedside environment, such as an intensive care unit, surgical suite, or emergency room. This paper describes the SPECT performance evaluation of the system for cardiac imaging, including both Tc-99m and F-18 radionuclides. For cardiac F-18 imaging in a bedside environment, the 511 keV SPECT approach using high energy collimation and anterior 180 degree acquisition has the advantages of not requiring a detector to be positioned beneath the bed and greatly reducing attenuation effects. In this study, we evaluated SPECT reconstructed image quality using an anthropomorphic dynamic cardiac phantom filled with Tc-99m and F-18 separately. The specific issues that were addressed in this study included the following: 1) mitigating septal penetration effects with the 511 keV photons using de-convolution filtering, 2) reducing truncation effects due to the relatively small field-of-view of the camera using angle-dependent center-of-rotation shifts, and 3) investigating the effects of reduced angular sampling and angular range. We found that reducing angular sampling to 28 projections through 135 degrees with Tc-99m and 25 projections through 180 degrees with F-18 showed all features of the myocardium.

Index Terms—Cardiac imaging, image processing, mobile PET, mobile SPECT.

I. INTRODUCTION

WE have developed a compact and mobile gamma imaging system that is designed for both PET and SPECT acquisitions within a bedside environment, such as an intensive care unit, surgical suite, or emergency room. The system consists of two compact detectors (25 cm × 25 cm active area) containing pixilated NaI scintillators (5 mm × 5 mm, 12.5 mm thick) and position-sensitive photomultiplier tubes. The detectors are mounted to a mobile gantry[1] that allows flexible detector motion and positioning for tomographic PET and SPECT imaging (Fig. 1). Details of the detector and gantry design and operation have been previously described in [1] and [2].

M. T. Studenski and A. Cebula are with the Department of Nuclear and Radiological Engineering, University of Florida, Gainesville, FL 32611 USA (e-mail: mstudens@ufl.edu; acebula@ufl.edu).

D. R. Gilland is with the Departments of Nuclear and Radiological Engineering and Biomedical Engineering, University of Florida, Gainesville, FL 32611 USA (e-mail: gilland@ufl.edu).

[1]Manufactured by Advanced Development Solutions, Phillipsburg, NJ, 08865

Fig. 1. Mobile gantry with detectors in an oblique and lateral orientation for SPECT imaging along with the associated mobile electronics rack seen to the right.

One of the key applications for this system is cardiac emission tomography, including both myocardial perfusion imaging using Tc-99m tracers and viability imaging using F-18 tracers [3]–[7]. For cardiac F-18 imaging in a bedside environment, the 511 keV SPECT approach using high energy collimation and an anterior 180 degree acquisition has the advantages of not requiring a detector to be positioned beneath the bed and greatly reducing attenuation effects.

The basic system performance measurements in planar and SPECT modes using both Tc-99m and F-18 point sources were described previously [2]. The low energy collimator for Tc-99m has 23 mm hole length, 1.5 mm hole diameter, and 0.2 mm septal thickness. The high energy collimator for F-18 has 49 mm hole length, 2.3 mm hole diameter, and 2.02 mm septal thickness. We found the spatial resolution at 10 and 20 cm to be 1.14 and 1.64 cm FWHM at 140 keV and 1.52 and 2.04 cm FWHM at 511 keV. The reconstructed SPECT spatial resolution near the center-of-rotation with a radius-of-rotation of 20 cm was measured to be 1.59 cm with Tc-99m and 1.58 cm with F-18 and the sensitivity was measured to be 4.15 counts/μCi/s with Tc-99m and 0.67 counts/μCi/s with F-18. Here, we further this system evaluation by considering reconstructed image quality using an anthropomorphic dynamic cardiac phantom[2] to simulate a more realistic source distribution and out-of-field activity (Fig. 2).

Three key factors for the imaging system are specifically addressed in this cardiac phantom study: 1) mitigating the effects of septal penetration photons for the 511 keV SPECT data, 2)

[2]Model ECT/DY-CAR/P, Data Spectrum Corp. Hillsborough, NC, 27278

Fig. 2.   The dynamic cardiac phantom and the bedside imaging system with the detector head in a left oblique position (45 degrees).

reducing truncation effects due to the relatively small field-of-view (FOV) of the detector, and 3) investigating the effects of reduced angular sampling and angular range.

To compensate for septal penetration effects, this study uses a Metz de-convolution filter which incorporates the measured 2D modulation transfer function (MTF) including septal penetration effects. The underlying assumption is that the septal penetration effects in the measured data can be modeled as a linear, spatially-invariant process. This method of septal penetration compensation was investigated previously for In-111 and I-123 imaging by King, *et al.*. [8].

Due to the relatively small FOV of the detectors, truncation of the myocardium can arise in the tomographic image, particularly in regions distant from the axis-of-rotation. In order to overcome this problem in this study, at each projection angle during the acquisition, the detector is translated tangentially to maintain the heart near the center of the FOV. This is effectively an angle-dependent center-of-rotation (COR) shift that is recorded and modeled in the reconstruction. Although this prevents truncation of the myocardium, there will likely be truncation of surrounding tissues, which is unavoidable with this small field-of-view system.

In this study we investigate the effects of angular sampling and angular sampling range on the resulting reconstructed image. Theoretically, it has been noted that the required number of angular samples changes linearly with the linear sampling distance and inversely with the field-of-view (FOV) size [9]. Comparing the FOV of this system (25 cm) to that of a traditional system (typically 50 cm), the required number of angular samples with this system is reduced by a factor of two relative to a traditional SPECT system. We would like to determine the minimum number of angular samples required since detector positioning with this prototype system is done manually, meaning that the detector is rotated to the desired angle, and then is moved horizontally and vertically until it is as close to the phantom as possible to maximize the spatial resolution at each projection angle. Subsequent system designs

could have automated positioning but it is not clear that for a mobile SPECT system, automated angle stepping, like conventional SPECT systems, will be the method of choice. In order to achieve a minimum source-to-detector distance for best spatial resolution at all angles, and an economical design, it is possible that manual positioning will be preferred. Clearly, the manual approach requires greater operator effort. In the manual positioning case, determining the minimum required number of angles is important.

Previous work on limited angular range (i.e., less than 360 degrees) has been used to reduce the overall acquisition time and improve image contrast [10], [11]. Our investigation of the reduced angular sampling range is motivated by our expectation that for applications such as ICU bedside imaging, it may be difficult to obtain quality lateral views of the patient if they are not capable of lifting their arms.

II. METHODS

A. Experimental Phantom

The dynamic cardiac phantom (Fig. 2) consists of a water filled torso, a beating heart composed of an inner and outer latex membrane, two lungs filled with one part water and two parts Styrofoam beads to simulate the density of the lungs, a Teflon spine, and a water filled liver. The volume contained between the two membranes of the beating heart can be filled with Tc-99m to simulate a myocardial perfusion study or with F-18 to simulate a myocardial viability study. A computer controlled pump is used to expand and contract the myocardium and values for stroke volume, ejection fraction, and beats per minute (BPM) can be input to the controlling computer. For this investigation, the phantom was programmed for 72 BPM, 45% ejection fraction, and 55 mL stroke volume.

For both the Tc-99m and F-18 studies, the phantom myocardium was filled with approximately 1 mCi of activity and the phantom liver (1700 mL) was filled with approximately 2 mCi of activity. For the F-18 studies, in order to isolate the effects of out-of-field activity, additional acquisitions were performed with no activity in the liver.

B. Data Acquisition

Acquisitions consisted of 37 projection angles equally spaced over 180 degrees. The energy window was 20% centered on the photopeak. Relatively high count, low noise projection data were acquired for both the Tc-99m and F-18 studies, and a count thinning technique was used to generate lower count data from this high count data [12]. This technique involves replacing each pixel value in the high count data with a sample from a binomial distribution with number of trials n equal to the high count pixel value and probability of success p equal to the desired scale factor. This is a convenient way to scale down the count level while maintaining the Poisson statistics of the measured data. For the Tc-99m study, the high count data were obtained using an approximately 55 minute acquisition time, which resulted in 2.5×10^5 total counts per projection. The F-18 data were obtained using an approximately 80 minute acquisition time with approximately 3.0×10^5 total counts per projection. One change

from the 37 projection angle protocol was that the F-18 acquisition containing out-of-field activity was done with 25 projection angles resulting in a 60 minute acquisition time.

In order to simulate the increased noise that results from shorter acquisition times, a count thinning technique was applied to the high count projection data. The count thinning approach was used to scale down the projection data by factors of 2, 4, and 8.

C. Metz Filtering of the Projection Data

In planar images of an F-18 point source, low intensity "tails" due to septal penetration by the 511 keV photons are observed [2], [6]. In order to conserve weight, the high energy collimator was designed to allow a 7% penetration level rather than the conventional 5% [13]. To mitigate this septal penetration effect in this study, we filter the projection data prior to the reconstruction using a 2D Metz filter, which is a combination of a de-convolution and smoothing filter [14]. The Metz filter function is given in (1) where $\mathrm{MTF}(v)$ is the 2D modulation transfer function and parameter X determines the extent to which the filter follows the inverse MTF before rolling off to zero gain. We tested a range of values for X (50, 100, and 200) for the F-18 filter and negative values in the filtered images were set to zero.

$$\mathrm{Metz}\left(v\right) = \frac{1 - \left(1 - \mathrm{MTF}\left(v\right)^2\right)^{\mathrm{X}}}{\mathrm{MTF}\left(v\right)} \qquad (1)$$

The 2D MTF for the Metz filter was obtained from measured point spread functions using an F-18 point source (5 mm in diameter and 20 cm from collimator) and is shown in Fig. 3 along with the point spread function from a similar Tc-99m point source. The star pattern due to collimator septal penetration is evident and is not seen in the 140 keV point source image. We acknowledge that the MTF is distance dependent and we chose 20 cm as an average source-to-detector distance over all the projections covering 180 degrees. We also tested the Metz filter on the Tc-99m data to study its effect on the final reconstructed image. For the Tc-99m projections, we tested the filter with values of 2, 5, and 10 for X in (1).

The first step in processing the projection data was to obtain the MTFs for both Tc-99m and F-18. Fig. 4 shows the MTFs along with horizontal and vertical profiles. From the calculated MTFs, the 2D Metz filter was created. Fig. 5 shows horizontal and vertical profiles from the 2D Metz filters with different values of X tested for the Tc-99m and F-18 acquisitions.

D. Image Reconstruction

Because of the small field-of-view of this system, the conventional method of orbiting the detector about a fixed axis located near the body axis can result in truncation of the heart region, as shown in Fig. 6(A). In order to eliminate the truncation of the myocardium, at each projection angle the detector is shifted tangentially to maintain the myocardium near the center of the FOV (Fig. 6(B)). This angle-dependent shift (effectively an angle-dependent "center-of-rotation" shift) is accounted for within the reconstruction algorithm.
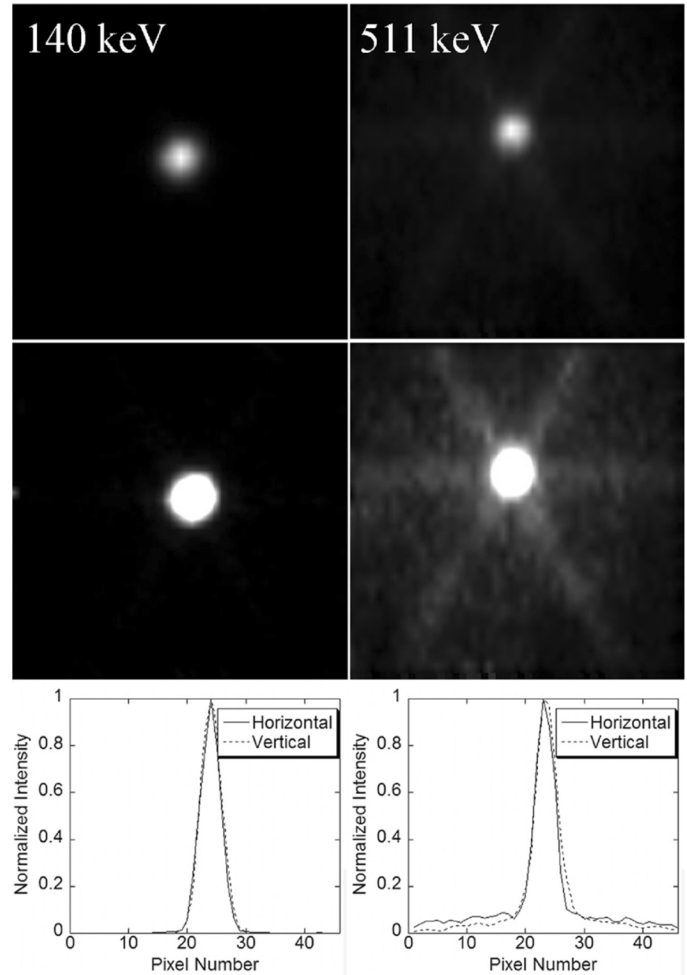

Fig. 3. Point source images for 140 keV and 511 keV sources without windowing (top), windowed to 33% of the maximum pixel intensity (middle), and the corresponding horizontal and vertical profiles (bottom). The FOV in both images is 25×25 cm^2.

For each projection, the horizontal and vertical position of the detector, and the detector angle are recorded. The angle-dependent shift is computed using simple trigonometric equations. The MLEM reconstruction algorithm (50 iterations for Tc-99m and 200 iterations for F-18) was used to reconstruct the images without attenuation, scatter, or detector response corrections applied [15]. These iteration stopping points, combined with the Metz filter, were chosen subjectively. The reconstruction times were approximately 10 seconds for the Tc-99m images and 40 seconds for the F-18 images.

E. Effect of Angular Sampling

One of the goals of this paper was to investigate the effect of reduced angular sampling and angular range on reconstructed image quality. To test how limiting the number of projection angles affected the final reconstructed images, we reduced the number of projections reconstructed from 37 to 19 and 10 evenly spaced projection angles through 180 degrees. The count level was adjusted for the three cases by count thinning to simulate a constant acquisition time. To test the effect of reduced angular sampling range, the anterior 135 and 90 degrees of projection
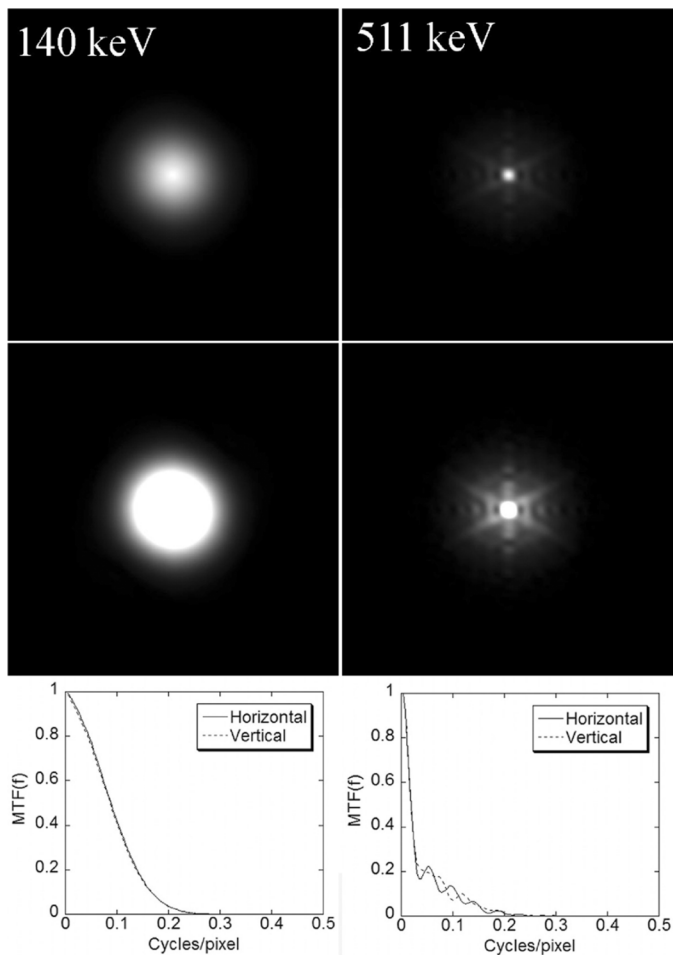
Fig. 4. MTF (top) and MTF windowed to 33% of the maximum pixel intensity (middle) with the corresponding horizontal and vertical profiles (bottom) for both 140 and 511 keV point sources used in calculating the Metz filter.

data were extracted and reconstructed. A constant acquisition time was simulated for these tests as well.

F. Comparison with a Commercial SPECT System

To compare the performance of the mobile system to a traditional SPECT system with Tc-99m, we acquired data of the dynamic cardiac phantom on a commercial SPECT system[3] with low energy, ultra-high resolution collimators. The phantom myocardium was filled with Tc-99m and a 180 degree, 64 projection acquisition was obtained at a moderately high count level (approximately 2.15×10^5 counts within a mid-ventricular 3 mm transaxial slice resulting in an acquisition time of approximately 20 minutes). The projections were obtained over the anterior 180 degrees, as with the mobile system. No activity was added to the phantom liver and no attenuation, scatter, or detector response corrections were applied to the MLEM reconstruction (50 iterations). We compared this data to a 15 minute, 37 projection acquisition with Tc-99m and out-of-field activity obtained with the mobile system.

[3]Triad 88, Trionix Research Laboratory, Twinsburg, OH 44087
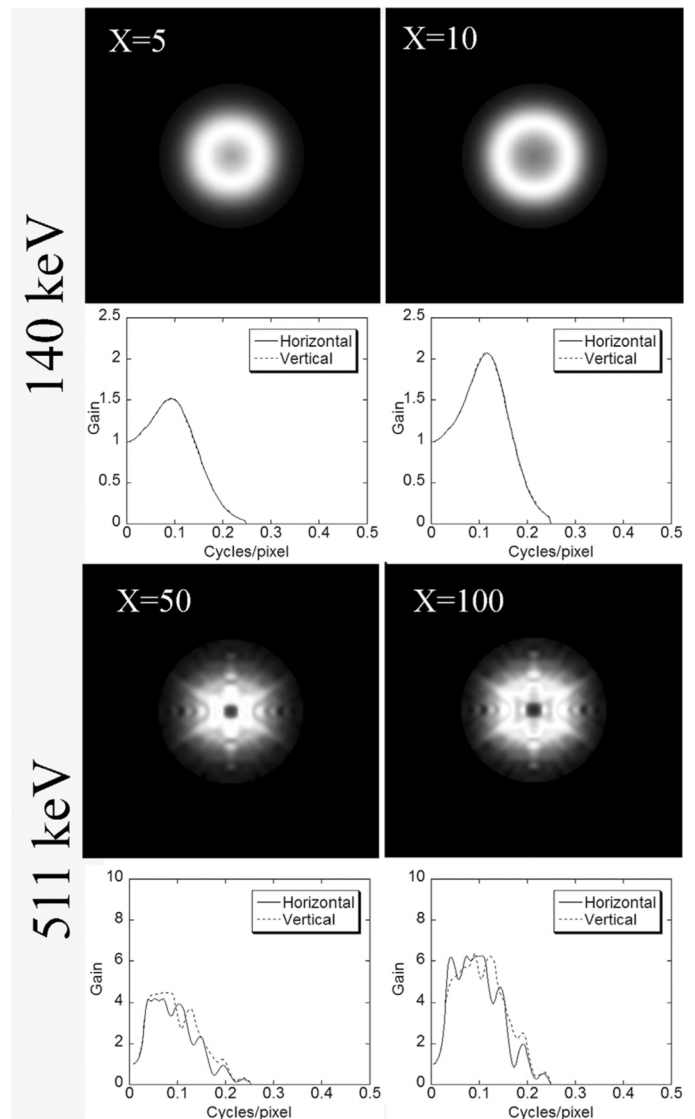
Fig. 5. Metz filters and the associated horizontal and vertical profiles for both 140 keV and 511 keV with different values for X.
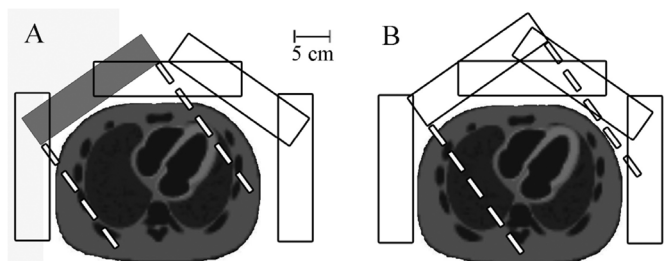
Fig. 6. Five projection angles demonstrating how myocardial truncation results in the fixed axis acquisition protocol (A) while the new protocol (B) eliminates truncation of the myocardium (but not surrounding tissue). The shaded detector's position causes myocardial truncation as shown by the dashed lines indicating the edges of the FOV.

G. Myocardial Defect Study

As an initial test to assess reconstructed image quality with a myocardial defect present, we obtained a fillable plastic defect (4 cm wide by 2 cm tall by 1 cm thick) that was filled with water
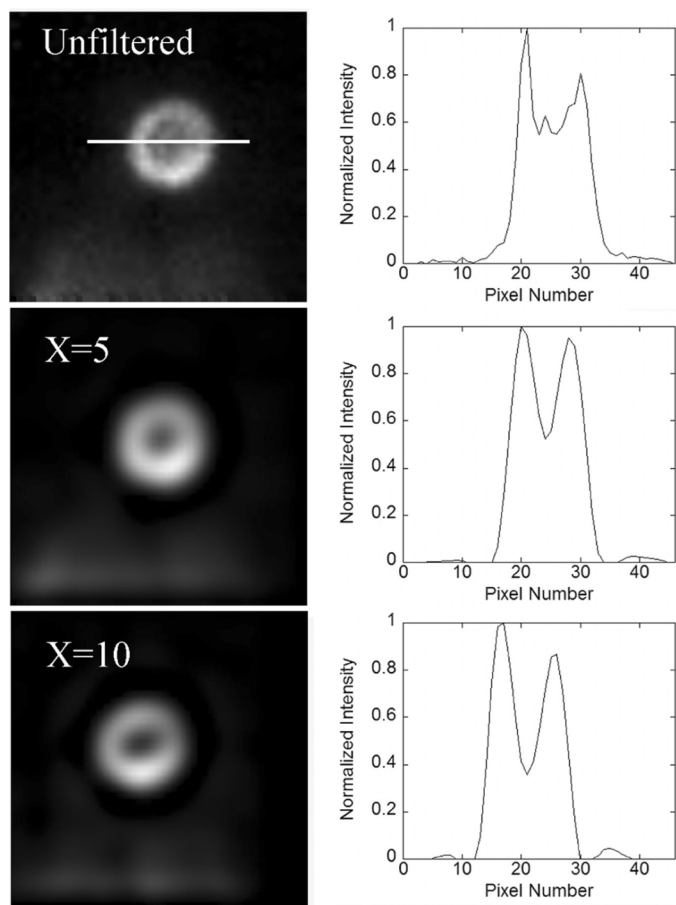
Fig. 7.   Projection images obtained at 45 degrees using Tc-99m and out-of-field activity with varying degrees of filtering.
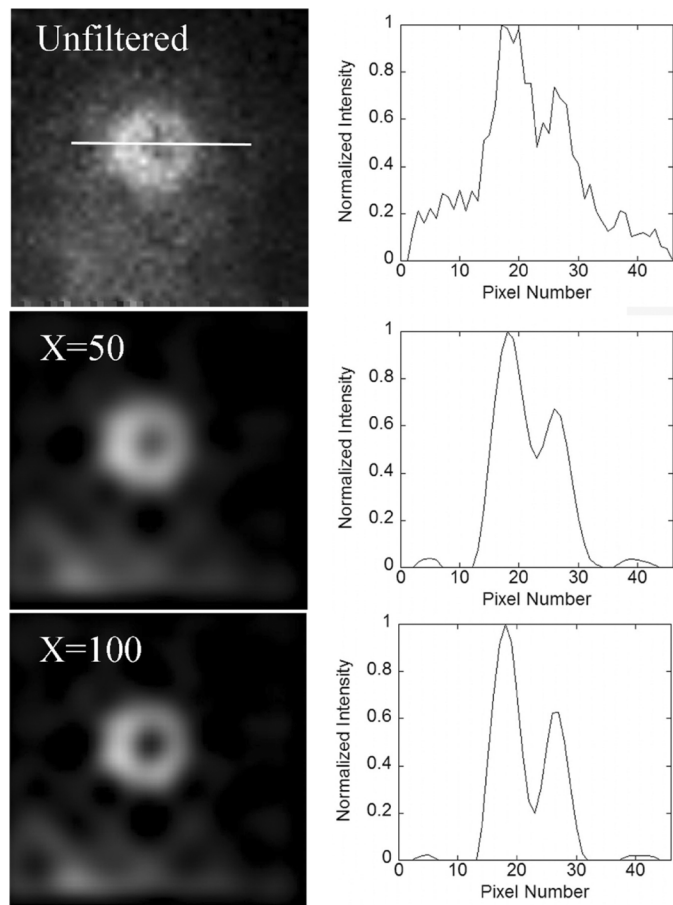
Fig. 8.   Projection images obtained at 45 degrees using F-18 and out-of-field activity with varying degrees of filtering.

without activity. We inserted this defect in the myocardium of the dynamic cardiac phantom and acquired 25 projection angles with 300 kcts/projection over the anterior 180 degrees. Two acquisitions were performed (Tc-99m and F-18). Each was 40 min. with 1 mCi of activity in the myocardium and 2 mCi in the liver to simulate out-of-field activity.

These acquisitions provided high count, low noise images. From this high count data, lower count data were generated using binomial thinning of the measured projection data to reduce the count level by a factor of four.

Projection data were reconstructed using 50 iterations of MLEM. The reconstructed images were reoriented into short axis slices. Profiles of the short axis slices were obtained through the myocardial defect region.

III. RESULTS

A. Septal Penetration Compensation

Figs. 7 and 8 show 45 degree projection images from the Tc-99m and F-18 acquisitions (with out-of-field activity), respectively, with the varying degrees of filtering. Detected events outside of the myocardium are more pronounced in the F-18 images, as expected, due to septal penetration. The Poisson noise in this region is evident. Larger values of the Metz filter parameter were used with the F-18 data in order to effectively compensate for septal penetration effects in the F-18 data. The pa-

rameter value of 100 with the F-18 data, while greatly reducing penetration effects, produced large negative values in the projection data that require truncation before reconstruction. The remainder of the results focus on $X = 5$ for Tc-99m and $X = 50$ for F-18.

B. Comparison With a Commercial SPECT System

Fig. 9 shows four long and short axis slices from both the commercial system acquisition and our 37 projection acquisition with the mobile system. The commercial system showed superior spatial resolution demonstrated by the thinner, more defined myocardium and superior statistical variation demonstrated by the even activity distribution throughout the myocardium. The differences in spatial resolution can be attributed to differences in collimator spatial resolution ("ultra-high" spatial resolution for the commercial system and general purpose class of spatial resolution with the mobile system) and also potentially to differences in angular sampling. The images with the commercial system provide a gold standard for image quality comparison, although bedside SPECT imaging is not possible with the commercial system.

C. Effect of Angular Sampling

1) Tc-99m: For the remainder of the paper, the figures are labeled in terms of number of projection angles/angular coverage in degrees/total acquisition time in minutes, as seen above the
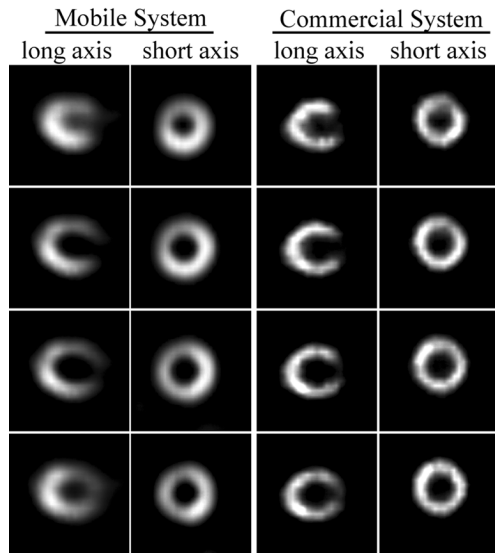
Fig. 9. Comparison of the mobile system's performance to a commercial system using the dynamic cardiac phantom and Tc-99m. The mobile system used 37 angles over 180 degrees and the commercial system used 64 angles over 180 degrees.
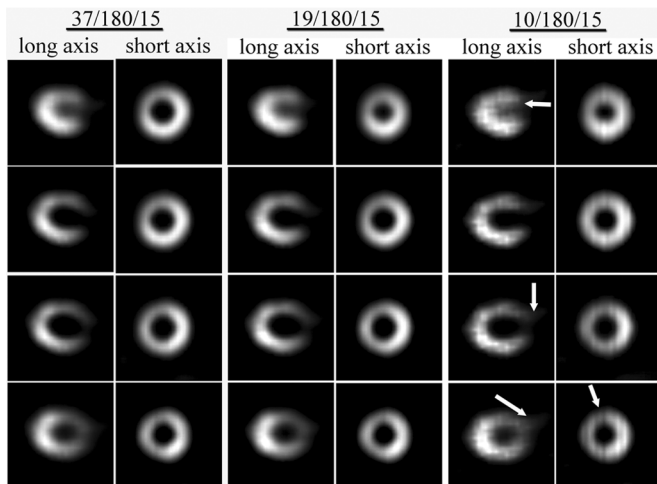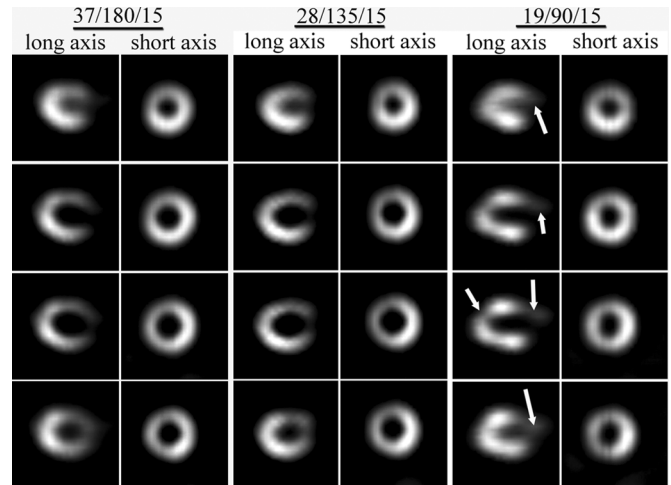

Fig. 11. Four long axis and four short axis slices from the Tc-99m 180 degree (highest sampling), 135 degree, and the 90 degree angular coverage acquisition. Artifacts are indicated by the white arrows.
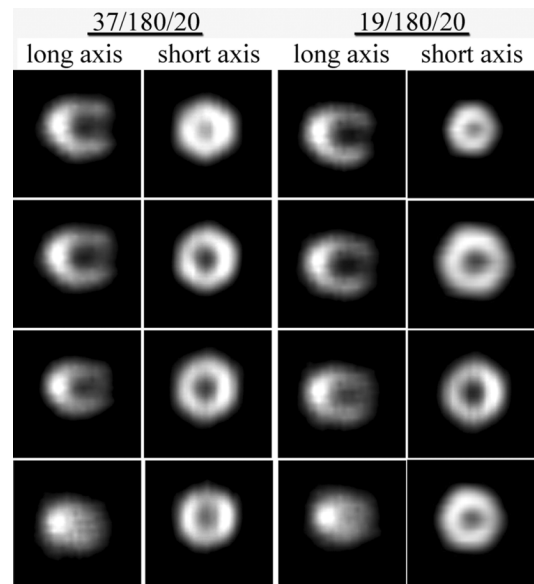

Fig. 10. Four long axis and four short axis slices from the 15 minute Tc-99m acquisitions with 37 (highest sampling), 19, and 10 projection angles. Artifacts in the images are indicated by the white arrows.

Fig. 12. Four long axis and four short axis slices from the F-18 acquisitions without activity in the liver and 37 and 19 projection angles.

images in Fig. 10. Fig. 10 shows four slices in both the short and long axis planes from 15 minute acquisitions with 37 (highest sampling), 19, and 10 projection angles. This figure demonstrates that reducing the number of projection angles to 19 does not appreciably affect the image quality when using Tc-99m. Fig. 10 also shows that reducing the sampling in an extreme case to 10 projections degrades the images both with streaking artifacts outside the myocardium and dark streaks in the myocardium.

We also wanted to test the effect of reducing the angular coverage from 180 degrees. We observed that reducing the angular coverage to 135 degrees did not severely degrade reconstructed image quality (Fig. 11). Fig. 11 also showed that severely limited angular coverage (90 deg.) introduced substantial streak artifacts. In a clinical situation, reducing the angular coverage

would only be recommended if the bedside environment prevented full 180 degree angular coverage.

2) F-18: Fig. 12 shows the reconstructed image slices from the F-18 data without out-of-field activity in the liver. Compared with the Tc-99m images with similar angular sampling, the F-18 images exhibit somewhat degraded spatial resolution of the myocardium walls and a reduced ventricle-to-myocardium contrast. This effect is due mainly to the propagation of the septal penetration patterns in the reconstruction. These effects become more pronounced in the 19 angle images although the overall shape of the myocardium is accurately depicted. The reduced angular sampling images also exhibited streaking artifacts that resulted from interpolation when the reconstruction was reoriented into long and short axis slices. These streaks are not seen in the projection images (Figs. 7 and 8) or in the original reconstruction.
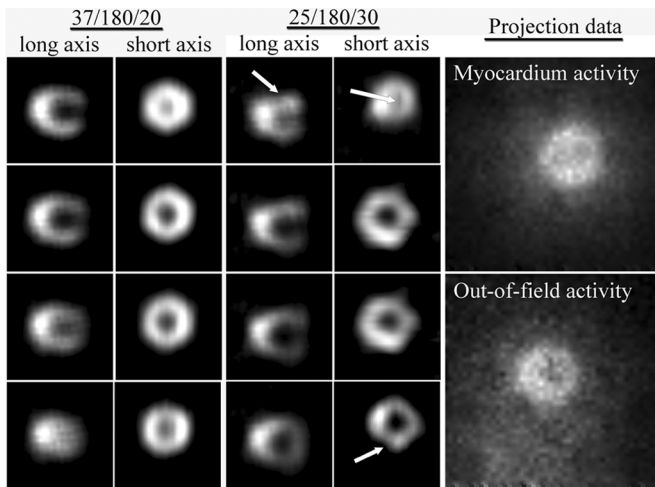
Fig. 13. Four long axis and four short axis slices from the F-18 acquisition without activity in the liver (left) and with out-of-field activity in the liver (middle). Artifacts are indicated by the white arrows. The projection data (unprocessed) to the right shows the effect of penetration photons from the out-of-field activity.
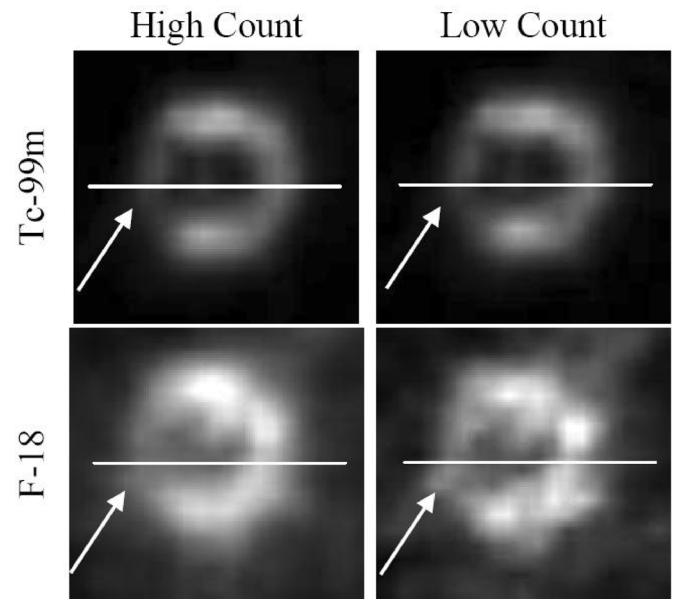

Fig. 14. Short axis slices from the high and low count acquisitions and the location of the profiles. The arrows indicate the location of the defect.

Fig. 13 shows the F-18 results with liver activity present compared to the highly sampled acquisition without activity in the liver. Also included in the figure are unprocessed projection images with and without background activity. These images begin to show a distortion of the shape of the myocardium and a small level of intensity artifacts (hot and cold spots) that are not observed in the images without liver activity. The streaking artifacts from interpolation are also present as before.

As with the Tc-99m acquisitions we reconstructed images with reduced angular coverage, but reducing the angular coverage to less than 180 degrees resulted in more severe streaking artifacts.

D. Myocardial Defect Study

Fig. 14 shows the reconstructed short axis images and location of the profiles used for comparison. There is minimal difference between the high and low count images for Tc-99m. The low count F-18 image shows increased noise and artifacts compared to the high count F-18 image.

Comparing the F-18 images with the Tc-99m images, the effects of septal penetration with the high energy emitter can be seen. In the F-18 images, there is a greater level of extra-myocardial intensity including in the ventricle region. Fig. 15 shows the increase in image noise for lower count acquisitions. For F-18, the effect of image noise appears as hot and cold spots in the image.

IV. Summary and Discussion

This paper presents the SPECT performance evaluation of a mobile gamma imager for cardiac applications using Tc-99m and F-18. The system employed angle-dependent projection shifting to reduce truncation effects and de-convolution filtering to control septal penetration effects with F-18. We chose the Metz filter over a simple low pass filter in order to de-convolve the low frequency tails in the point spread function that result
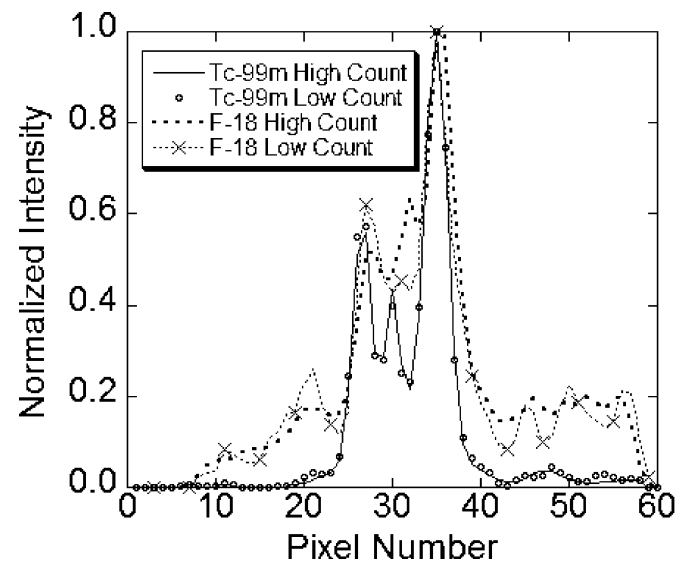

Fig. 15. Normalized line profiles from the high and low count Tc-99m and F-18 acquisitions.

from septal penetration. Like a low-pass filter, the Metz filter is also capable of controlling high frequency noise by rolling off to zero gain at high frequency.

Another possible means of reducing the effect of septal penetration is to use the point response function in an iterative reconstruction algorithm [16]. This method has been shown to be effective although it requires greater computation than simple de-convolution filtering.

The results using a dynamic cardiac phantom showed that with Tc-99m, the reconstructed image quality did not substantially degrade when the angular sampling was reduced to 19 angles over 180 degrees or to 28 angles over 135 degrees. The results with the F-18 images showed a moderate degree of spatial resolution loss compared with the Tc-99m images. With liver

activity present in the F-18 images, a distortion of the myocardial shape was observed, which we attribute to increased detection of septal penetration photons.

Results from the myocardial defect study demonstrate the capability of the mobile SPECT system to image a moderately sized defect, void of activity, with Tc-99m and F-18 distributions. In the Tc-99m images, the defect was readily apparent. In the F-18 images, the quality was degraded by septal penetration of the 511 keV photons in spite of using a high energy collimator. In a clinical setting, it is possible this mobile SPECT system may have difficulty imaging subtle myocardial defects with F-18 tracers, but it may effectively image moderate to severe defects.

The effects of limited angles and septal penetration will depend on the source distribution. We have attempted to mimic realistic source distributions by including extra-myocardial activity in the liver. In patients more areas other than the heart and liver contain activity; therefore, the results from this study may not generalize to all patient studies.

Future work will involve investigating alternate collimators for the 511 keV SPECT approach, for example, a pinhole collimator [17]–[19]. This type of collimator would more effectively reduce septal penetration effects. Also, the anthropomorphic thorax phantom with the defect will be scanned with the commercial SPECT system. Phantom images acquired on the commercial SPECT system will then be compared to images reconstructed from the mobile system under similar conditions.

REFERENCES

[1] A. G. Weisenberger, S. Majewski, D. Gilland, W. Hammond, B. Kross, J. Proffitt, J. McKisson, and M. Smith, "Implementation of a mobile cardiac PET imager for the emergency room and intensive care unit," in *Proc. IEEE Nuclear Science Symp. Conf. Rec.*, 2007, vol. 5, pp. 3705–3708.

[2] M. T. Studenski, D. Gilland, J. Parker, B. Hammond, S. Majewski, A. Weisenberger, and V. Popov, "Performance evaluation of a bedside cardiac SPECT system," *IEEE Trans. Nucl. Sci.*, vol. 56, no. 3, pp. 625–632, Jun. 2009.

[3] G. DePuey, E. V. Garcia, and D. S. Berman, , Lippencott, Williams, and Williams, Eds., *Cardiac SPECT Imaging*, 2nd ed. Philadelphia, PA: Lippincott, Williams & Wilkins, 2001.

[4] J. Patton *et al.*, "High energy (511 keV) imaging with the scintillation camera," *Radiograph.*, vol. 16, pp. 1183–1194, 1996.

[5] M. Sandler *et al.*, "Fluorine-18 fluoro-deoxyglucose cardiac imaging using a modified scintillation camera," *J. Nucl. Med.*, vol. 39, pp. 2035–2043, 1998.

[6] C. Laymon and T. Turkington, "Characterization of septal penetration in 511 keV SPECT," *Nucl. Med. Commun.*, vol. 27, no. 11, pp. 901–909, 2006.

[7] E. Q. Chen, W. J. MacIntyre, R. T. Go, R. C. Brunken, G. B. Saha, C. O. Wong, D. R. Neumann, S. A. Cook, and S. P. Khandekar, "Myocardial viability studies using fluorine-18-FDG SPECT: A comparison with fluorine-18-FDG PET," *J. Nucl. Med.*, vol. 38, pp. 582–586, 1997.

[8] M. A. King, R. B. Schwinger, B. C. Penney, P. W. Doherty, and J. A. Bianco, "Digital restoration of indium-111 and iodine-123 SPECT images with optimized Metz filters," *J. Nucl. Med.*, vol. 27, pp. 1327–1336, 1986.

[9] H. H. Barrett and W. Swindell, *Radiological Imaging: The Theory of Image Formation, Detection, and Processing*. San Diego, CA: Academic, 1981.

[10] P. F. Sharp, H. G. Gemmell, and A. D. Murray, *Practical Nuclear Medicine*, 3rd ed. New York: Springer, 2005.

[11] D. E. Wessell, D. J. Kadrmas, E. C. Frey, and B. M. W. Tsui, "Limited angle tomographic breast imaging: A comparison of parallelbeam and pinhole collimation," in *Proc. IEEE Nuclear Science Symp. Conf. Rec.*, Nov. 2–9, 1996, vol. 2, pp. 1104–1108.

[12] R. Bartoszynski and M. Niewiadomska-Bugaj, *Probability and Statistical Inference*, 2nd ed. New York: Wiley-Interscience, 2008.

[13] S. Cherry, J. Sorenson, and M. Phelps, *Physics in Nuclear Medicine*, 3rd ed. Philadelphia, PA: Saunders, 2003.

[14] C. E. Metz, "A mathematical investigation of radioisotope scan image processing," Ph.D. dissertation, Univ. Pennsylvania, Philadelphia, 1969.

[15] L. A. Shepp and Y. Vardi, "Maximum likelihood reconstruction in positron emission tomography," *IEEE Trans. Med. Imag.*, vol. 1, no. 2, pp. 113–122, 1982.

[16] G. Zeng, G. Gullberg, C. Bai, P. Christian, F. Trisjono, E. Di Bella, J. Tanner, and H. Morgan, "Iterative reconstruction of fluorine-18 SPECT using geometric point response correction," *J. Nucl. Med.*, vol. 39, pp. 124–130, 1998.

[17] C. R. Tenney, M. P. Tornai, M. F. Smith, T. G. Turkington, and R. J. Jaszczak, "Uranium pinhole collimators for 511-keV photon SPECT imaging of small volumes," *IEEE Trans. Nucl. Sci.*, vol. 48, no. 4, pp. 1483–1489, Aug. 2001.

[18] M. F. Smith, R. J. Jaszczak, and H. Wang, "Pinhole aperture design for I-131 tumor imaging," *IEEE Trans. Nucl. Sci.*, vol. 44, no. 3, pp. 1154–1160, Jun. 1997.

[19] M. Smith, R. Jaszczak, H. Wang, and J. Li, "Lead and tungsten pinhole inserts for I-131 SPECT tumor imaging: Experimental measurements and photon transport simulations," *IEEE Trans. Nucl. Sci.*, vol. 44, no. 1, pp. 74–82, Feb. 1997.

Design of a Compact, Mobile PET Detector for Bedside Cardiac Imaging

Uday J. Tipnis, David R. Gilland, *Member, IEEE*, Mark F. Smith, *Member, IEEE*, Walter E. Drane
and Stan Majewski

Abstract—The long term objective of this work is to design and build a compact and mobile PET system for bedside cardiac imaging. For patients under intensive care with severe left heart failure, FDG PET studies are crucial for the decision between emergency bypass surgery versus heart transplantation, but often these patients are too ill to be transported to an outpatient PET center. Our goal is to design a PET system that can be transported within a hospital for imaging in environments such as an intensive care unit (ICU) as well as an operating room or interventional suite. In this paper we investigate by simulation the effect of limited angle acquisition on the quality of reconstructed images for a given compact detector design and imaging geometry. We present results of a simulated phantom study that show the effect of changing the number of detector positions, the distance between the detectors and the angles of acquisition.

I. INTRODUCTION

THE goal of this project is to design and build a compact and mobile PET detector for bedside cardiac imaging in environments such as an Intensive Care Unit. A difficult challenge with tomographic imaging within such an environment is achieving complete angular sampling due to limitations posed by the patient bed. Compared with imaging tables of conventional PET systems, the beds are wider and thicker and include side rails and support structure that makes it difficult to rotate a detector beneath a bed. Typical ICU mattresses are 3-6 inches thick, 36 inches wide and 84 inches long. They have a bed and also include support structure and side rails. Fig. 1 shows photographs of a typical ICU bed.

Fig. 1. Photographs of a typical ICU bed. The side rails can be moved up and down. The mattress side-to-side width (not including the side rails) is 36 inches. The thickness of the mattress is 3-6 inches.

For this reason we are investigating a limited angle approach in which compact, planar detectors are positioned at several angles along the patient's thorax. Fig. 2 shows 3D sketches of the gantry design concept at two detector positions along with the patient and the bed.
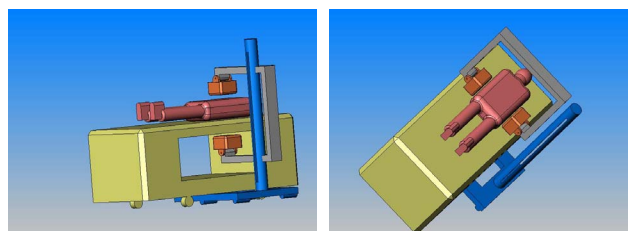

Fig. 2. Gantry design concept. The sketches show two positions of the detectors with reference to the patient and the bed.

Apart from these two positions of acquisition, the angular positions are affected by the patient bed. The size of the patient is also a factor in the quality of the reconstructed images as it affects the distance between the detector faces. Fig. 3 is a sketch that shows the patient bed and the different detector positions. Using a simulated phantom study we investigate the effects of changing the number of acquisition angles, the distance between the detectors and the angles of acquisition on the quality of reconstructed images.
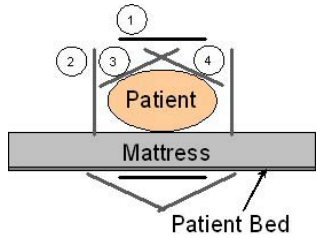
Fig. 3. A sketch of the patient bed and the various detector positions.

II. METHODS

The proposed PET detector design consists of two planar detectors, each with a 25 cm x 25 cm imaging area. The detectors contain pixelated (5 mm x 5 mm x 10 mm) arrays of Sodium Iodide (NaI) crystal detectors at a pitch of 5.5 mm.
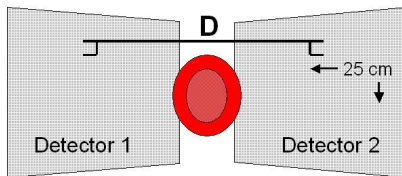

Fig. 4. A sketch of the source object and detector geometry.

We investigate the effect of changing the detector-to-detector distance (D) on the reconstructed image quality considering D=30 cm and 40 cm and the effect of changing the number of detector positions from 2 to 4. Even in the 4 detector position case we change the angles of the detectors with respect to the source object (+/- 10°, +/- 20° and +/- 30°) and observe its effect.

We use an analytical simulation to compute the projection data from a known source object. The simulation computes path lengths through the source region and models the stopping efficiency of the NaI crystal to the 511 keV gamma rays. The non-uniform sensitivity throughout the field-of-view is modeled appropriately. In order to isolate the effects of the limited angle reconstruction, this simulation did not consider attenuation or scatter within or around the source object, detector blurring or image noise.

The source object consisted of a 3D annulus designed to model the myocardium in FDG myocardial metabolism imaging. The semi-axes of the inner walls of the annulus were 3 cm, 3 cm and 4 cm, and the wall thickness 2 cm. The source object was centered between the two detector faces. Fig. 4 is a sketch of the detector geometry and the source object.

Images were reconstructed using a 3D MLEM method with 5 iterations. With these simple source objects, we have found that this is a sufficient number of iterations to achieve convergence. The reconstructed image volume is 15 cm x 15 cm x 15 cm, centered in the field-of-view, and voxels are 2.5 mm a side. For purposes of the simulation we considered only the source object to be present within the detectors, to isolate the effects of limited angle reconstruction. Fig. 5 is a sketch of

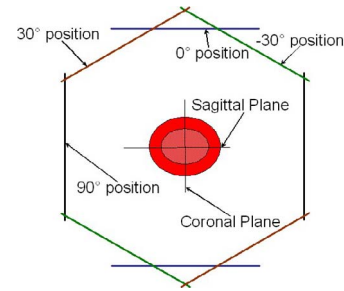the source object and the various angles of acquisition (detector positions) we used.

Fig. 5. Transaxial view of source object and detector positions.

The sketch in Fig. 5 shows the detectors at 0°, 90° and +/- 30°. We have also acquired images with detector positions at +/- 10° and +/- 20°, apart from the one detector position (0°) and two detector (0°, 90°) positions.

III. RESULTS

The reconstructed images are presented in this section. Fig. 6 shows images which highlight the effect of increasing the number of detector positions. The rows have been numbered from top to bottom as row 1 to row 4. Row 1 is the views of the actual object. Rows 2, 3 and 4 are the views of the reconstructed images with 1, 2 and 4 detector positions respectively. A single detector position means both detectors placed opposite to each other at a given angle. With one detector position (row 2) we see significant distortion in the shape of the object in the coronal and transaxial views (left and right columns respectively) whereas the size of the object is distorted in the sagittal view (middle column). The coronal and transaxial views are distorted to a much greater extent than the sagittal view because for the one detector position case, the detectors are parallel to the sagittal plane and perpendicular to the coronal and transaxial planes. This distortion in the shape and size of the object reduces considerably as we increase the number of detector positions to two (0° and 90°) and then four (-30°, 0°, 30°, 90°) because of the more complete angular sampling achieved.

Fig. 7 shows reconstructed images which highlight the effect of changing the angles of the detectors while keeping the number of detector positions constant. All the images in Fig. 7 have been reconstructed with four detector positions but the angles of the detectors are different for each of them. Row 1 is the views of the actual object. Row 2 is the reconstructed images of the object with detector positions of -10°, 0°, 10° and 90°. We can see distortion in the shape of the reconstructed images in the transaxial view (right column). There is slight distortion in the size of the object in the sagittal view (middle column). As we increase the angles of the detectors from +/- 10° to +/- 20° there is an improvement in the shape of the object in the transaxial view but the size distortion in the sagittal view is very much similar. A further

increase in the angles of the detectors to +/- 30°, improves the shape of the object in the transaxial view and its size in the sagittal view considerably.
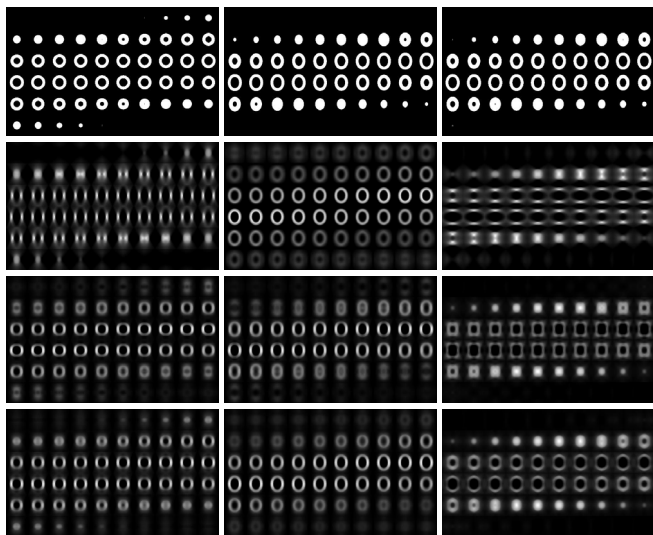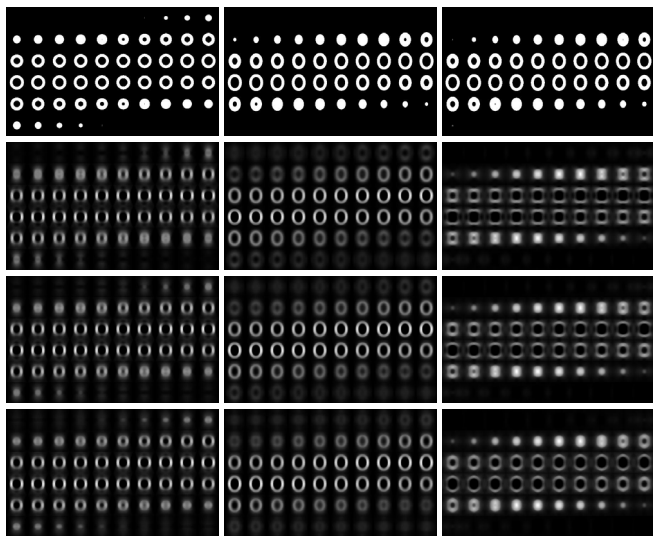

Fig. 6. Reconstructed images showing the effect of changing the number of detector positions. Left column: Coronal view, Middle column: Sagittal view, Right column: Transaxial view. Rows 1-4: Top to Bottom. Row 1: True Object. Row 2: Reconstructed images with one detector position (0°). Row 3: Reconstructed images with two detector positions (0°, 90°). Row 4: Reconstructed images with four detector positions (-30°, 0°, 30°, 90°).

Fig. 7. Reconstructed images showing the effect of changing angles of detectors while keeping the number of detector positions constant. Left column: Coronal view, Middle column: Sagittal view, Right column: Transaxial view. Rows 1-4: Top to Bottom. Row 1: True Object. Row 2: Reconstructed images with four detector positions (-10°, 0°, 10°, 90°). Row 3: Reconstructed images with four detector positions (-20°, 0°, 20°, 90°). Row 4: Reconstructed images with four detector positions (-30°, 0°, 30°, 90°).

Fig. 8 shows reconstructed images with distance between the detector faces changed. Row 2 is reconstructed images with four detector positions and distance between detector faces (D) 30 cm. Row 3 is reconstructed images with four detector positions, same angles of acquisition for the detectors and distance between detector faces (D) 40 cm. The sagittal view appears improved when the distance between the detector faces is reduced from 40 cm to 30 cm. The distortions in the size of the object are reduced as the distance between detector faces is reduced.
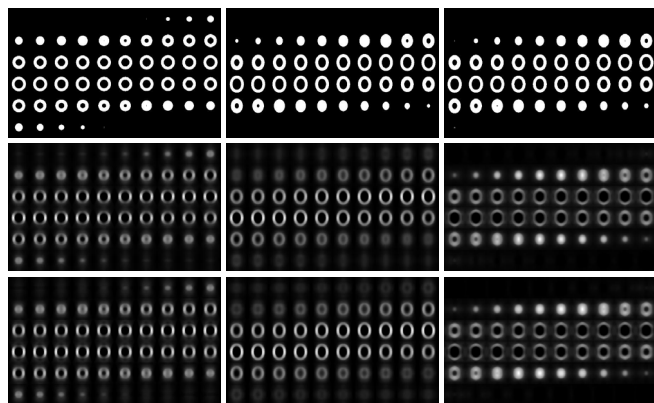

Fig. 8. Reconstructed images showing the effect of changing the distance between the detector faces. Left column: Coronal view, Middle column: Sagittal view, Right column: Transaxial view. Rows 1-3: Top to Bottom. Row 1: True Object. Row 2: Reconstructed images with four detector positions (-30°, 0°, 30°, 90°), D=30 cm. Row 3: Reconstructed images with four detector positions (-30°, 0°, 30°, 90°), D=40 cm.

From the results presented above we can see that the quality of the images improves as we increase the number of detector positions or reduce the distance between the detector faces. It also improves with increase in the angles of detectors for a fixed number of detector positions. This is because of the better angular sampling achieved in each of the cases.

IV. SUMMARY

A typical ICU bed poses challenges to bedside PET imaging in an ICU environment due to obstructions from the thick, wide mattress and its support structures. The results of this study show that with the proposed detector design, a substantial degree of distortion and blurring occurs in images acquired with one (0°) or two (0°, 90°) detector positions due to insufficient angular sampling. But when the number of detector positions is increased to four then we see a significant reduction in the blurring and distortion artifacts. Even when using four detector positions, the quality of the reconstructed images improves as we increase the angles of the detectors from +/- 10° to +/- 20° and +/- 30°.

V. REFERENCES

[1] C.J. Thompson, K. Murthy, R.L. Clancy, J.L. Robar, A. Bergman, R. Lisbona, A. Loutfi, J.H. Gagnon, I.N. Weinberg, R. Mako, "Imaging Performance of PEM-I: A High Resolution System for Positron Emission Mammography (PEM)", Nuclear Science Symposium and Medical Imaging Conference Record, Vol. 2, Pg. 1074-1078, (1995).
[2] M.F. Smith, S. Majewski, A.G. Weisenberger, D.A. Kieper, R.R. Raylman, T.G. Turkington, "Analysis of factors affecting positron

emission mammography (PEM) image formation", IEEE Transactions on Nuclear Science, Vol. 50, No. 1, Feb. 2003, Pg. 53-59.

[3] M.F. Smith, S. Majewski, R.R. Raylman, "Positron emission mammography with multiple angle acquisition", Nuclear Science Symposium and Medical Imaging Conference Record, Vol. 3, Pg. 1883-1886, (2002).

[4] R.S. Miyaoka, T.K. Lewellen, J.S. Kim, M.S. Kaplan, S.K. Kohlmyer, W. Costa, F. Jansen, "Performance of Dual Headed SPECT System for Coincidence Detection", Nuclear Science Symposium and Medical Imaging Conference Record, Vol. 3, Pg. 1348-1352, (1995).

[5] P. Nelleman, H. Hines, W. Braymer, G. Muehllehner, M. Geagan, "Performance Characteristics of Dual Headed SPECT scanner with PET capability", Nuclear Science Symposium and Medical Imaging Conference Record, Vol. 3, Pg. 1751-1755, (1995).

[6] R. Freifelder, J.S. Karp, "A dedicated PET scanner for Breast Cancer", Nuclear Science Symposium and Medical Imaging Conference Record, Vol. 3, Pg. 1358-1362, (1995).

[7] C.J. Thompson, K. Murthy, Y. Picard, I.N. Weinberg, R. Mako, "Positron Emission Mammography (PEM): A Promising technique for detecting Breast Cancer", Nuclear Science Symposium and Medical Imaging Conference Record, Vol. 4, Pg. 1893-1897, (1994).

[8] R.H. Huesman, G.J. Klein, W.W. Moses, J. Qi, B.W. Reutter, P.R.G. Virador, "List Mode Maximum Likelihood Reconstruction applied to PEM with Regular Sampling", IEEE Transactions on Medical Imaging, Vol. 19, No. 5, May 2000, Pg. 532-537.

[9] J. Qi, G.J. Klein, R.H. Huesman, "Image Properties of List Mode Likelihood Reconstruction for Rectangular PEM with Depth of Interaction (DOI) measurements", IEEE Transactions on Nuclear Science, Vol. 48, No. 4, Aug. 2001, Pg. 1343-1349.

[10] Y. D'Asseler, S. Vandenberghe, C.G. Matthews, M. Koole, R. Van de Walle, I. Lemahieu, R.A. Dierckx, "Three Dimensional Geometric Sensitivity Calculation for Three Headed Coincidence Imaging", IEEE Transactions on Nuclear Science, Vol. 48, No. 4, Aug. 2001, Pg. 1446-1451.

[11] R.R. Raylman, S. Majewski, R. Wojcik, A.G. Weisenberger, B. Kross, V. Popov, "Correction for the Effects of Accidental Coincidences, Compton Scatter and Object Size in PEM Imaging", IEEE Transactions on Nuclear Science, Vol. 48, No. 3, June 2001, Pg. 913-923.

[12] N.K. Doshi, R.W. Silverman, Y. Shao, S.R. Cherry, "maxPET: A Dedicated Mammary and Axillary Region PET Imaging System for Breast Cancer", IEEE Transactions on Nuclear Science, Vol. 48, No. 3, June 2001, Pg. 811-815.

[13] S. Vandenberghe, Y. D'Asseler, M. Koole, R. Van de Walle, I. Lemahieu, R.A. Dierckx, "Physical Evaluation of 511 keV Coincidence Imaging with a Gamma Camera", IEEE Transactions on Nuclear Science, Vol. 48, No. 1, Feb. 2001, Pg. 98-105.

[14] R.S. Miyaoka, S.K. Kohlmyer, T.K. Lewellen, "Hot Sphere Detection Limits for Dual Head Coincidence Imaging System", IEEE Transactions on Nuclear Science, Vol. 46, No. 6, Dec. 1999, Pg. 2185-2191.

[15] K. Murthy, D. Jolly, M. Aznar, C.J. Thompson, A. Loutfi, R. Lisbona, J.H. Gagnon, "Quantification in PEM with Planar Detectors: Contrast Resolution Measurements using a Custom Breast Phantom and Novel Spherical Hot Spots", IEEE Transactions on Nuclear Science, Vol. 46, No. 6, Dec. 1999, Pg. 2192-2196.

[16] D. Visvikis, T. Fryer, S. Downey, "Optimization of Noise Equivalent Count Rates for Brain and Body FDG Imaging using Gamma camera PET", IEEE Transactions on Nuclear Science, Vol. 46, No. 3, June 1999, Pg. 624-630.

[17] C.M. Laymon, T.G. Turkington, R.E. Coleman, "Attenuation Effects in Gamma Camera Coincidence Imaging", IEEE Transactions on Nuclear Science, Vol. 45, No. 6, Dec. 1998, Pg. 3115-3121.

[18] C.J. Thompson, K. Murthy, Y. Picard, I.N. Weinberg, R. Mako, "Positron Emission Mammography (PEM): A Promising technique for detecting Breast Cancer", IEEE Transactions on Nuclear Science, Vol. 42, No. 4, Aug. 1995, Pg. 1012-1017.

[19] R.S. Miyaoka, W.L.S. Costa, T.K. Lewellen, S.K. Kohlmyer, M.S. Kaplan, F. Jansen, C.W. Stearns, "Coincidence Imaging using a Standard Dual Headed Camera", Nuclear Science Symposium and Medical Imaging Conference Record, Vol. 2, Pg. 1127-1134, (1996).

[20] T.K. Lewellen, R.S. Miyaoka, F. Jansen, M.S. Kaplan, "A Data Acquisition System for Coincidence Imaging using Conventional Dual Headed Gamma Camera", Nuclear Science Symposium and Medical Imaging Conference Record, Vol. 2, Pg. 1305-1309, (1996).

A Simulation Study of a Bedside Cardiac PET Imager

Uday J. Tipnis, *Student Member, IEEE*, Mark F. Smith, *Member, IEEE*, Timothy G. Turkington, John Wilson, Stan Majewski, Brian Kross, Randolph Wojcik, David R. Gilland, *Member, IEEE*

Abstract—This paper presents the results of a simulation study on the imaging performance of a bedside cardiac PET system. The proposed system consists of two compact gamma cameras mounted on a mobile gantry. Key challenges presented by this imaging context include: detector positioning to obtain sufficient angular sampling, attenuation correction in the absence of transmission images, and control of image noise. The primary aim of this paper was to quantify the extent of reconstructed image artifacts that result from these effects under the anticipated imaging conditions. The simulation studies demonstrated that limited angle acquisition is the primary source of artifacts followed by attenuation effects. Image noise in this context was not a major factor in the reconstructed image quality. Image artifacts resulting in a nearly 50% variation in image intensity in isolated regions of the myocardium could be expected from this imaging system. Such artifacts render the detection of mild myocardial defects highly difficult; however, severe defects should still be detectable with this system, which can offer important diagnostic information for this patient population.

I. INTRODUCTION

THE long term objective of this project is to design and build a compact and mobile PET detector for bedside cardiac imaging in environments such as an intensive care unit (ICU), interventional suite or operating room. This PET system could provide critical information on cardiac function for patients with severe left heart failure, but who cannot be transported to a conventional PET facility.

A difficult challenge with tomographic imaging within such an environment is achieving complete angular sampling due to limitations imposed by the patient bed. Compared with imaging tables of conventional PET systems, the beds are wider and thicker and include side rails and support structure that makes it difficult to rotate a detector beneath a bed. Typical ICU mattresses are 3-6 inches thick, 36 inches wide and 84 inches long. Fig. 1 shows photographs of a typical ICU bed. One beneficial feature typical of these beds is the low

attenuating plastic plate beneath the patient's thorax, which is designed to allow chest x-ray imaging (Fig. 1, lower right).

Fig. 1. Photographs of a typical ICU bed. The side rails can be moved up and down.

In order to help overcome the physical obstacles to tomographic imaging in this environment, we are investigating the use of compact, planar detectors that would allow detector positioning and acquisition in tight spaces (Fig. 2). The proposed detector design utilizes a pixelated crystal and position-sensitive photomultiplier tubes to provide high count rate capability and reduce dead space along the perimeter of the detector face. Such detector designs have been previously used successfully with limited angle acquisitions for positron emission mammography applications. Such a system has been built and its performance has been evaluated using phantoms [1]-[4]. The purpose of this work was to investigate the use of this detector design with limited angle acquisition for cardiac imaging applications.
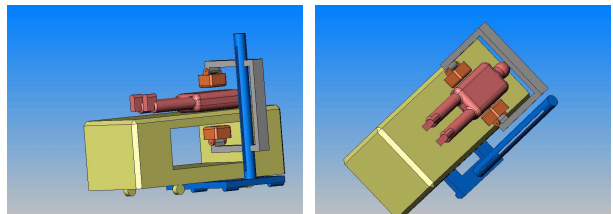

Fig. 2. Gantry design concept. The sketches show two positions of the detectors with reference to the patient and the bed.

An additional challenge to cardiac PET imaging in this environment is compensating for attenuation effects without the availability of transmission images. In this paper we evaluate the results of using a uniform attenuation map based on knowing the patient boundary. Such a method should be possible in this imaging context. The final effect that is evaluated in this paper is that of image noise. Noise is one effect that we anticipate will be reduced in this imaging context relative to conventional PET imaging due to the long imaging times that will be possible for patients in an intensive care unit.

Hence, using a simulated phantom study we investigate the impact of: 1) limited angular sampling, 2) attenuation correction and 3) count statistics on non-uniform intensity artifacts and hence quality of reconstructed images.

II. METHODS

A. Data Simulation

The proposed PET detector design consists of two planar detectors, each with a 25 cm x 25 cm imaging area. The detectors contain pixelated (5 mm x 5 mm x 25 mm) arrays of sodium iodide (NaI) crystals at a pitch of 5.5 mm. Two acquisition angles were considered: lateral (60 cm detector separation) and anterior/posterior (33 cm detector separation). The detector separation for the lateral view accommodates room for the patient arms, which may not be able to be raised out of the field-of-view. The anterior/posterior view detector separation considers typical patient thorax dimensions and bed thickness. Figure 3 shows a scaled drawing of the detector positioning relative to the patient thorax.

We use an analytical simulation to compute projection data from a known source object. The simulation computes path lengths through the source region and models the stopping efficiency of NaI crystal to the 511 keV gamma rays. The non-uniform sensitivity throughout the field-of-view is modeled appropriately. Based on experiments with a physical prototype system using a cardiac torso phantom, we added realistic levels of noise to the simulated data. It was computed from these experiments that a typical PET data acquisition from a detector of this design would contain approximately 6 million total counts, which was the count level used in these simulations.

The source object consisted of a 3D annulus designed to model the myocardium in FDG myocardial imaging. The semi-axes of the inner walls of the annulus were 2.5 cm, 3.5 cm and 2.5 cm, and the wall thickness 1.5 cm. In some cases, a defect was modeled in the myocardium. It had reduced intensity (75% and 25% of normal source intensity) and was an ellipsoid of semi axes lengths 1 cm x 2 cm x 2 cm. No activity was modeled outside the myocardium. The attenuating body consisted of lungs and torso defined around the myocardium. The torso was an elliptical cylinder of 20 cm x 12 cm semi axes lengths and assumed to be filled with water. The lungs were circular cylinders of 5.5 cm semi axis length and assumed to contain 1/3 water and 2/3 air. Figure 3 is a sketch of the source object, attenuating body and the two angles of acquisition (detector positions).
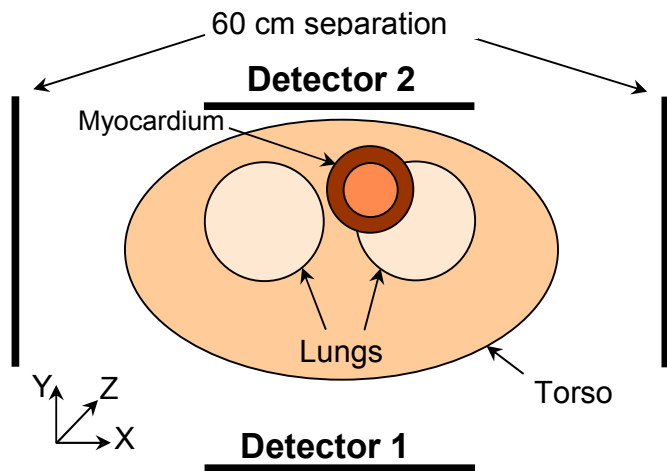

Fig. 3. A sketch of the two detector positions, attenuating body and source object.

B. Image Reconstruction

Images were reconstructed using a 3D MLEM algorithm with 25 iterations. With these simple source objects, we have found that this is a sufficient number of iterations to achieve convergence. The reconstructed image volume was 15 cm x 15 cm x 15 cm, centered on the myocardium, and voxels were 3.75 mm a side. Attenuation correction was done using either uniform attenuation map (average value computed on basis of all defined regions between detector faces) or exact non-uniform attenuation map (regions exactly as shown in Fig. 3). Table I below summarizes the various acquisition parameters considered for the results presented in the next section.

TABLE I
Summary of acquisition parameters.

Figure#	Attenuation Correction	Noise	# of detector positions	Defect
Fig. 5A	No	No	2	No
Fig. 5B	No	Yes	2	No
Fig. 5C	Uniform	Yes	2	No
Fig. 5D	Non-uniform	Yes	2	No
Fig. 5E	No	Yes	4	No
Fig. 6B	No	Yes	2	75%
Fig. 6D	No	Yes	2	25%

C. ROI Analysis

To quantify degree of non-uniform intensity artifacts in the reconstructed images, region-of-interest (ROI) analysis was performed. Average intensities ($\bar{I}$) were computed within six ROI's within the myocardium in 3D. The locations of the six regions are shown in Fig. 4. For each region an index of the intensity artifact was computed representing the variation of that region's intensity from the maximum region intensity:

$$A_i = \frac{\bar{I}_i}{\bar{I}_{max}}, i = 1,6$$

where $\bar{I}_{max}$ is maximum region intensity. The ideal reconstructed image, in the absence of true defects, has $A_i = 1$ for all six regions.
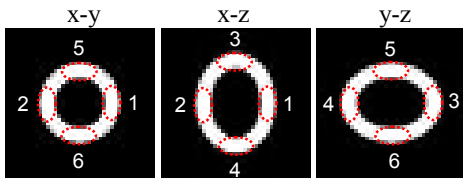
Fig. 4. True object and ROI's.

The index A was computed for images with no attenuation correction, uniform correction and exact non-uniform correction. Additional simulations included reconstructed images with noise free data (to evaluate effect of noise) and with complete angular sampling (to evaluate effect of limited angular sampling). The complete angular sampling acquisition had data from 4 detector positions, 45° apart with 34 cm detector separation and circular detector path.

III. RESULTS

Reconstructed images are presented in this section. Table II gives A values for reconstructed images shown in Figure 5. The minimum value of A for each of the reconstructed images is underlined in the table.

Comparing images without and with the expected image noise (Fig. 5A and 5B, respectively), we see that noise does not have substantial effect on reconstructed image quality. The values in the second and third row of Table II confirm this conclusion. Uniform attenuation correction offers only slight improvement in intensity artifacts over no attenuation correction as shown in Fig. 5C and row 4 of Table II.

Non-uniform attenuation correction, if it were possible in this context, would offer improvement in reconstructed image artifacts. Fig. 5D and row 5 in Table II demonstrate this effect. ROI analysis of images with complete angular sampling gives near perfect A values. Hence, reduction in artifacts can be attributed most to improvement in angular sampling. Figure 6 shows images of objects with 25% and 75% intensity defect modeled, to estimate the severity of defect that can be diagnosed by a PET imager of this design.
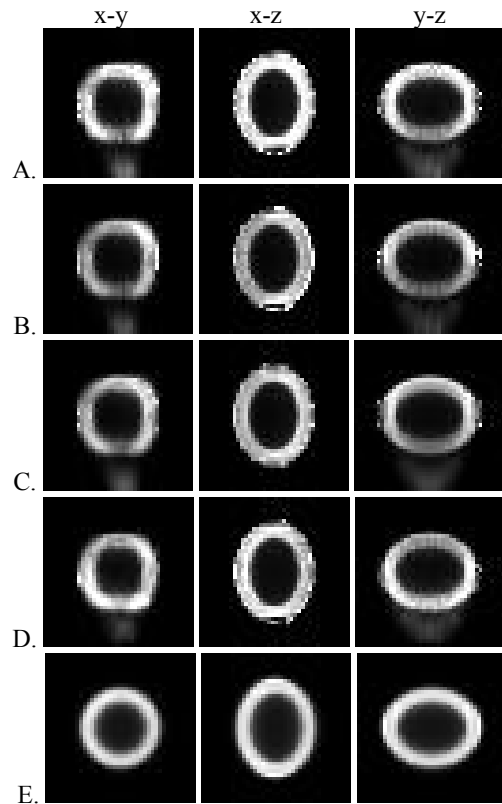

Fig. 5. Reconstructed images with A) Noise free data and no attenuation correction, B) No attenuation correction, C) Uniform attenuation correction, D) Exact non-uniform attenuation correction and E) Complete Angular Sampling.

Table II
Non-uniform Intensity Artifact (A) values
(AC=attenuation correction)

Region # Image	1	2	3	4	5	6
Noise free, no AC	1.00	0.73	0.95	0.89	0.78	0.48
No AC	1.00	0.74	0.93	0.87	0.78	0.48
Uniform AC	1.00	0.79	0.90	0.85	0.78	0.52
Non-uniform AC	0.96	0.95	1.00	0.87	0.66	0.88
Complete Angular Sampling	0.92	0.98	0.99	1.00	0.98	0.92

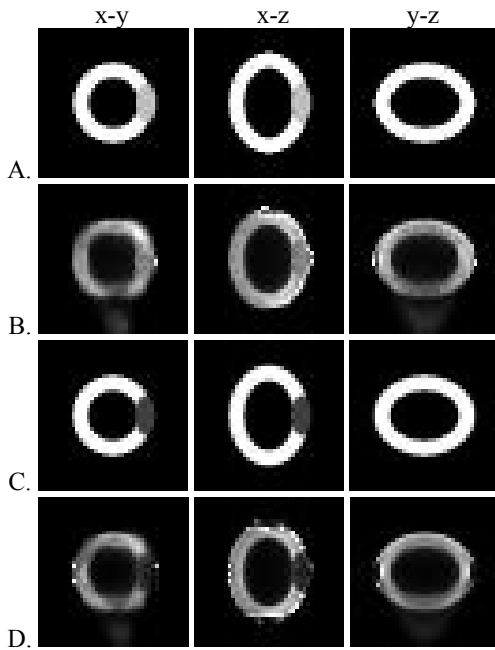|	x-y	x-z	y-z

A.

B.

C.

D.

Fig. 6. True objects with A) 75% defect and C) 25% defect. Reconstructed images without attenuation correction and with B) 75% defect and D) 25% defect.
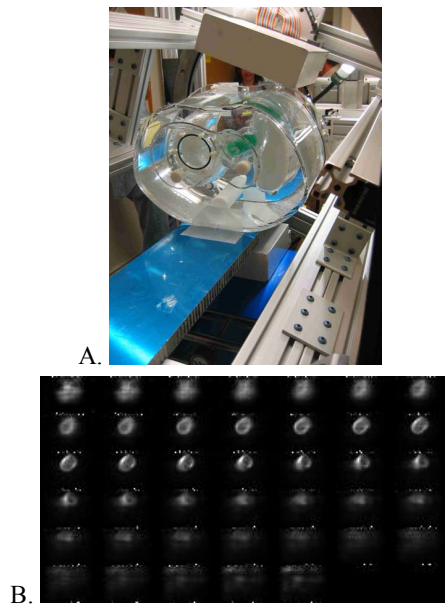
A.

B.

Fig. 7. A) Photograph of physical prototype gantry and cardiac and torso phantom, B) Images reconstructed from data obtained from the gantry and phantom.

IV. SUMMARY

A simulation study was performed to investigate the effects of noise, attenuation and angular sampling on reconstructed image quality for a proposed bedside cardiac PET imager. Results showed that image noise will not be a critical factor in this context due to high count statistics. Reconstructed image

intensity artifacts result primarily from limited angle acquisition and secondarily from non-ideal attenuation correction. A cardiac PET imager of this nature may have limited application for the diagnosis of mild defects (75% of normal intensity), but should have clinical application for the diagnosis of moderate to severe to defects (0-50% of normal intensity) for patients who otherwise cannot be imaged by PET.

V. DISCUSSION

Future work will focus on experimental acquisitions with a prototype gantry and cardiac torso phantom. Figure 7A shows a photograph of this gantry and phantom. Figure 7B shows images reconstructed from data acquired with a single detector position. In the future, data will be acquired and analyzed from detector positions influenced by the patient bed and size.

VI. REFERENCES

[1] C.J. Thompson, K. Murthy, R.L. Clancy, J.L. Robar, A. Bergman, R. Lisbona, A. Loutfi, J.H. Gagnon, I.N. Weinberg, R. Mako, "Imaging Performance of PEM-I: A High Resolution System for Positron Emission Mammography (PEM)", IEEE Nuclear Science Symposium and Medical Imaging Conference Record, Vol. 2, Pg. 1074-1078, (1995).
[2] M.F. Smith, S. Majewski, R.R. Raylman, "Positron emission mammography with multiple angle acquisition", IEEE Nuclear Science Symposium and Medical Imaging Conference Record, Vol. 3, Pg. 1883-1886, (2002).
[3] R. Freifelder, J.S. Karp, "A dedicated PET scanner for Breast Cancer", IEEE Nuclear Science Symposium and Medical Imaging Conference Record, Vol. 3, Pg. 1358-1362, (1995).
[4] C.J. Thompson, K. Murthy, Y. Picard, I.N. Weinberg, R. Mako, "Positron Emission Mammography (PEM): A Promising technique for detecting Breast Cancer", IEEE Transactions on Nuclear Science, Vol. 42, No. 4, Aug. 1995, Pg. 1012-1017.

Performance Evaluation of a Small Field-of-View, Mobile PET/SPECT System

Matthew. T. Studenski, *Member, IEEE,* J.G. Parker, D.R. Gilland, S. Majewski, B. Hammond

Abstract– **This paper reports on the initial performance evaluation of a small field-of-view, mobile PET/SPECT system for bedside imaging. The system was designed to move within a hospital to image patients who cannot easily be transported to a conventional PET or SPECT facility, for example, patients within an intensive care unit (ICU). The focus of the system is cardiac imaging in which both viability (^{18}F fluorodeoxyglucose; FDG) and perfusion (^{99m}Tc Sestamibi) images are desired. This paper evaluates the capabilities of the mobile system for acquisitions at both 140 keV (Tc-99m) and at 511 keV (F-18) operated in single photon counting mode. Parameters evaluated were the planar and reconstructed SPECT spatial resolution, the intrinsic energy resolution, sensitivity, and the count rate capability. Results demonstrate an intrinsic energy resolution of 32% at 140 keV and 23% at 511 keV, a planar intrinsic spatial resolution of 0.56 cm full width half-maximum (FWHM) at 140 keV and 0.61 cm FWHM at 511 keV, a system spatial resolution at 10 cm of 1.14 cm FWHM for both 140 keV and 511 keV, a reconstructed SPECT spatial resolution of 1.37 cm at 140 keV (22 cm radius-of-rotation), a sensitivity of 3.1 counts•µCi^{-1}•s^{-1} at 140 keV and 0.48 counts•µCi^{-1}•s^{-1} at 511 keV, and a maximum count rate of 1.46×10^5 counts/s at 140 keV and 1.56×10^5 counts/s at 511 keV.**

I. INTRODUCTION

The ability to bring an anatomical imaging system (mobile radiographic system or mobile C-arm fluoroscope) to a patient rather than the patient to the imaging system is commonplace in clinical radiology today. The University of Florida has developed an imaging system that allows functional imaging (SPECT and PET) to be brought to patients who cannot be transported to a traditional facility, for example, patients within an intensive care unit (ICU). This mobile gantry system has been designed to position the detectors for PET or SPECT acquisitions under the challenging conditions of the bedside environment. The company Segami Inc. (Columbia, MD) does market a portable cardiac SPECT scanner, but it requires that the patient is moved into a seated position. The system described in this paper is designed to image patients lying supine in, for example, an ICU bed.

Fig. 1. Mobile gantry system in a bedside environment with the detector heads in anterior positions for acquisitions in the single photon detection (SPECT) mode.

The system consists of two compact detectors, each with approximately 25×25 cm^2 detector areas, mounted on a mobile gantry system with a detachable computer and electronics rack (Fig. 1). The detectors (fabricated at Thomas Jefferson National Accelerator Facility [1]) consist of pixilated NaI(Tl) (5.0×5.0×12.5 mm^3 with 5.5 mm pitch). This scintillator was chosen to enable a compact and economical imager for both 140 keV and 511 keV. The reduced detection efficiency for 511 keV from the 12.5 mm thick NaI crystal is a concern, but we anticipate that this can be partially compensated by longer scan times in ICU applications. The photomultiplier tube (PMT) readout uses position-sensitive PMTs with high-rate four analog outputs arranged in a 4×4 array for each detector to form the 25×25 cm^2 active detector area.

The gantry system includes low profile legs that slide beneath ICU beds for stable support. The detectors mount to the rails of a linear bearing set that allows precise horizontal detector motion. Vertical detector motion is motor-driven using electronic motion control modules. Detector pivoting provides the additional, necessary motion dimension for tomographic imaging. The linear motions and pivot angle are digitally encoded for input to the reconstruction software. In PET mode, the detectors assume an 180˚ opposing orientation and in SPECT mode, a single detector can assume any angular orientation and orbit the anterior of the patient (Fig. 1).

This paper reports on the performance evaluation of this imaging system operated in single photon detection mode (SPECT) for both 140 keV (Tc-99m) or 511 keV (F-18). The 511 keV SPECT approach, using high energy collimators and acquiring projections over the anterior 180˚, has advantages over PET imaging despite the reduced detection sensitivity. First, projection data with complete angular sampling (anterior 180˚) is more readily achieved with SPECT mode due to the

restrictions in detector positioning beneath the bed in coincidence PET mode. Second, the effects of attenuation and scatter are greatly reduced with 511 keV SPECT (anterior 180°) for cardiac imaging relative to coincidence PET.

II. METHODS

The four metrics evaluated for the mobile system were intrinsic energy resolution, planar and reconstructed SPECT spatial resolution, sensitivity, and count rate capability for both 140 keV and 511 keV imaging.

A. Energy Resolution

The energy resolution of the system was measured intrinsically (without a collimator) with a point source positioned 75 cm from the detector face and 1.0×10^7 total counts acquired for each source. Using this geometry, energy spectra of the point sources were obtained. An 80 µCi source of Tc-99m (140 keV gamma) was imaged at the low energy setting and a 240 µCi source of F-18 (511 keV gamma) was imaged at the high energy setting. These activities were low enough to ensure that the detector did not exceed the maximum count rate. The peak channel and the FWHM of each spectrum were measured.

To determine a keV/channel calibration factor for each energy setting, a 5 µCi source of Co-57 (122 keV gamma) was imaged at the low energy setting and a 65 µCi source of Cs-137 (662 keV gamma) was imaged at the high energy setting. The peak channel for each of these sources was measured and a keV/channel factor was obtained for each energy setting. This calibration factor was used to convert the measured energy resolution (FWHM in channels) into keV units.

B. Spatial Resolution

The intrinsic planar spatial resolution of the system was measured using a 1 mm wide slit phantom. A 190 µCi Tc-99m point source and a 160 µCi F-18 source was positioned 75 cm from the detector face and 1×10^7 counts were obtained. Since almost all of the detector face was shielded, the count rate was not an issue. To ensure that the slit was not overlapping two pixels, three acquisitions were obtained with the slit moved 1 mm each time.

The system planar spatial resolution at 140 keV and 511 keV was evaluated using low and high energy collimators, respectively. The different parameters for these collimators can be seen in Table I. The measurements used 1 mm diameter capillary tubes to create line sources at distances of 10 cm, 20 cm, and 30 cm from the collimator face and oriented in both the X and Y directions. Profiles were taken across the images to obtain line spread functions (LSF) at each distance. 500 µCi of Tc-99m and 200 µCi of F-18 were used to obtain 5.0×10^5 counts at each distance and the FWHM was measured. For the 511 keV case, the FWHM was measured both with and without subtracting a constant from the LSF to compensate for the tails in the distribution due to septal penetration. This constant was computed from the average

intensity of twenty pixels not contained in the peak. The measured FWHM was reported by averaging the X and Y directions. These results were then compared to the theoretical FWHM calculated using the effective length of the collimator holes, the diameter of the holes, and the distance from the collimator face [2].

Uniformity correction was applied to all the images acquired for spatial resolution measurements. The image used to uniformity correct each acquisition was the intrinsic flood image acquired for the energy resolution evaluation at each respective energy. A 40% energy window was used for the 140 keV images and a 25% energy window was used for the 511 keV images.

Finally, a multi-angle SPECT acquisition was performed on a 5 mm diameter, 2.5 mCi, Tc-99m syringe (point source) to measure the reconstructed spatial resolution of the system at 140 keV. A total of 19 projections (every 10° from 0°–180°) with 5×10^5 counts per projection were obtained. The activity in the syringe was centered in the detector field-of-view with a radius of rotation of 22 cm. A filtered back-projection reconstruction algorithm with no smoothing filter was used to reconstruct the projections into a 45×45×45 voxel image (5 mm^3 voxels). A profile was taken across a transaxial slice of the reconstructed image and from this, the FWHM was measured.

C. Sensitivity

The extrinsic (with collimator) system sensitivity in terms of counts•µCi^{-1}•s^{-1} was evaluated using point sources of 240 µCi Tc-99m and 534 µCi F-18 suspended 30 cm from the collimator face. A 600 s acquisition with a 40% energy window for Tc-99m and a 25% energy window for F-18 was obtained of each source. For the 140 keV acquisition, the total number of counts in each pixel was summed to yield the total number of counts in the 600 s acquisition time. For the 511 keV acquisition, only a 20 cm^2 elliptical region-of-interest containing the source was summed to avoid counting events from septal penetration at the edge of the image. Using this data, the sensitivity of the detector at each energy setting was calculated.

D. Count Rate

The maximum intrinsic count rate was evaluated using 1.1 mCi F-18 and 535 µCi Tc-99m. Each source was suspended 30 cm from the detector face and 20 s acquisitions were obtained while the source decayed through several half lives. The number of counts per second (cps) minus the background was recorded at each time so the maximum count rate could be measured.

TABLE I. LOW ENERGY (140 keV) AND HIGH ENERGY (511 keV) COLLIMATOR PARAMETERS

	Low Energy	High Energy
Hole Shape	hexagonal	hexagonal
Collimator Thickness [cm]	2.3	4.9
Hole Diameter [mm]	1.5	2.3
Septal Thickness [mm]	0.2	2.02

III. RESULTS

A. Energy Resolution

The energy spectrum from the Tc-99m and F-18 images can be seen in Fig. 2. The measured FWHM was 108 channels for the F-18 spectrum and 166 channels for the Tc-99m spectrum. The energy resolution for each energy setting was calculated by multiplying the calibration factor (keV/channel) to the FWHM obtained from each respective energy spectrum. The resulting energy resolutions were 32% at 140 keV and 23% at 511 keV.
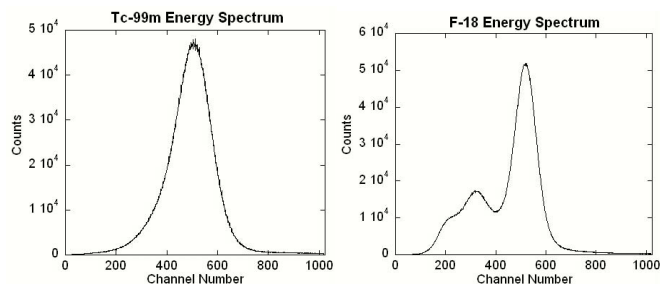

Fig. 2. Energy spectra obtained from 1×10^7 count acquisitions with Tc-99m and with F-18 point sources.

B. Spatial Resolution

The intrinsic spatial resolution of the detector was measured to be 0.56 cm FWHM at 140 keV and 0.61 cm FWHM at 511 keV. Fig. 3 shows the normalized intrinsic LSFs from the slit phantom. The tails in the 511 keV profile are assumed to be from scatter in the detector.
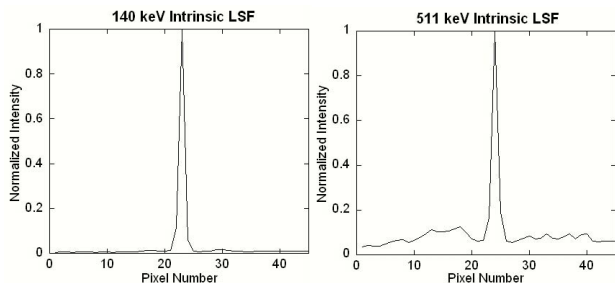

Fig. 3. Normalized intrinsic LSFs measured using a 1 mm wide slit phantom and a Tc-99m and F-18 point source 75 cm from the detector.

Fig. 4 shows the normalized LSF from the capillary tube acquisitions at 140 keV and 511 keV in the X direction. Notice the tails from septal penetration in the 511 keV LSFs.

Fig. 5 shows the normalized LSF at 511 keV after subtracting a constant (0.18), which was the average pixel intensity from twenty pixels not contained in the peak. The measured FWHM of the LSF compared with theoretical values can be seen in Table II.

Table II shows that the tails from septal penetration caused significant degradation in the measured FWHM. Subtraction of the tails resulted in less deviation from the theoretical mean.

To prove that the image degradation was actually a result of septal penetration and not scatter from surrounding materials, a simulation was run using the GATE software package [3], a front-end for the GEANT4 Monte Carlo simulation code [4], with the same geometry as the point source sensitivity acquisition but with no scattering material surrounding the crystal (for example, PMTs, gantry, and detector box).
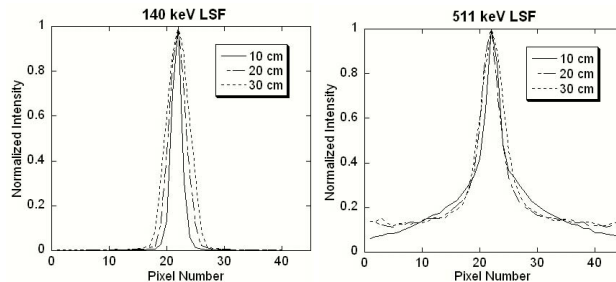

Fig. 4. Normalized LSFs obtained from 1 mm diameter capillary tube acquisitions of 5×10^5 counts at 10, 20, and 30 cm from the detector face at both 140 keV and 511 keV (notice the septal penetration tails in the 511 keV LSFs).
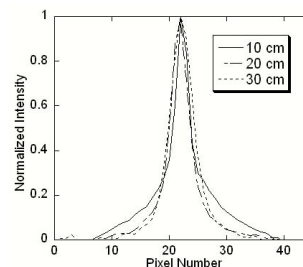

Fig. 5. Normalized LSFs of 1 mm diameter capillary tube acquisitions at 511 keV with a constant (0.18) subtracted to eliminate septal penetration tails.

Fig. 6 shows the acquired image (A) and the simulated image (B). The tails in the point spread function (PSF) from the simulated image show that the spread in the LSF resulted from septal penetration and not from scatter. An interesting observation is the difference in PSF and LSF at 511 keV. The height of the penetration tail is higher in the LSF (Fig. 4) due to the contribution of all parts of the line source to the tails in the profile. The point source does not have this extra source contribution at all points and therefore the tails are lower and only appear as a star pattern in the image.

Fig. 7 shows transaxial slice 45 from the reconstructed SPECT image of the Tc-99m syringe along with its

TABLE II. SYSTEM SPATIAL RESOLUTION MEASUREMENTS (FWHM in cm)

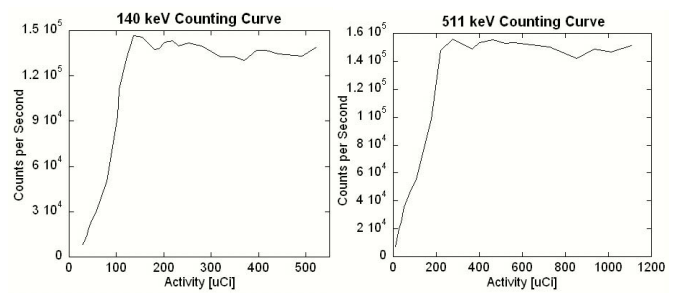|	b [cm]	No Subtraction	With Subtraction	Theoretical	% Deviation
140 keV	10	1.14	-	0.99	14.7
	20	1.64	-	1.57	4.5
	30	2.35	-	2.18	7.8
511 keV	10	1.54	1.14	1.03	50.0 / 11.1
	20	1.93	1.62	1.56	23.7 / 3.8
	30	2.64	2.03	2.13	23.9 / -4.7

Fig. 8. Counting curves for Tc-99m and F-18 obtained over several half-lives.

this energy. The images and energy spectra were distorted when the detector count rate was saturated.

IV. CONCLUSIONS AND FUTURE WORK

This unique system is capable of performing bedside SPECT imaging at both 140 keV and at 511 keV. Future work will involve multi-angle SPECT acquisitions at 511 keV to determine the reconstructed spatial resolution. Also, evaluation of the spatial resolution, sensitivity, count rate, and reconstructed spatial resolution of the PET capabilities of the system along with studies involving anthropomorphic phantoms and patients will be part of the ongoing research on this system.

REFERENCES

[1] A. G. Weisenberger, S. Majewski, D. Gilland, W. Hammond, B. Kross, V. Popov, J. Proffitt, J. McKisson, and M. F. Smith. Implementation of a Mobile, Cardiac PET Imager for the Emergency Room and Intensive Care Unit. *2007 IEEE Nuclear Science Symposium and Medical Imaging Conference.*

[2] S. Cherry, J. Sorenson, M. Phelps, *Physics in Nuclear Medicine, 3rd ed.* Philadelphia: Saunders, 2003.

[3] S. Jan et al, "GATE: A Simulation Toolkit for PET and SPECT," *Physics in Medicine and Biology*, 2004; 49: 4543-4561.

[4] Geant4 Collaboration (S. Agostinelli et al), "GEANT4: A Simulation Toolkit." *Nuclear Instruments and Methods in Physics Research*, 2003;506: 250-303.

Fig. 6. Acquired (A) and simulated (B) 511 keV point source images with the corresponding normalized PSFs in the X and Y directions.
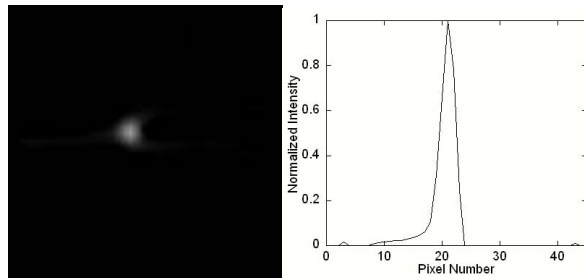
Fig. 7. Reconstructed transaxial slice 45 from a 19 projection angle SPECT acquisition of a Tc-99m point source and the corresponding normalized PSF.

corresponding PSF. The FWHM calculated from the PSF was 1.37 cm.

C. Sensitivity

From the total counts obtained in each image, the extrinsic sensitivity was calculated to be 3.1 counts•μCi^{-1}•s^{-1} for Tc-99m and 0.48 counts•μCi^{-1}•s^{-1} for F-18. The difference in sensitivity can be accounted for in two ways: the geometric sensitivity of the two collimators and the attenuation efficiency of the NaI crystal at each energy. The geometric sensitivity of the low energy collimator is about two times higher than the high energy collimator and the attenuation through 12.5 mm of NaI at 140 keV is about three times higher than at 511 keV (including scatter). These two effects account for the factor of six increase in sensitivity of the system at 140 keV versus 511 keV.

D. Count Rate

The maximum intrinsic count rate of the detector was measured to be 1.56×10^5 cps at 511 keV and 1.46×10^5 cps at 140 keV. At the time of the maximum count rate, there was 275 μCi F-18 and 135 μCi Tc-99m present. The counting curves for 511 keV and 140 keV can be seen in Fig. 8.

The saturation of the detector occurred at a lower activity for Tc-99m because of the higher sensitivity of the detector at

Implementation of a Mobile Cardiac PET Imager for the Emergency Room and Intensive Care Unit

A.G. Weisenberger, S. Majewski, D. Gilland, W. Hammond, B. Kross, V. Popov, J. Proffitt, J. McKisson, and M. F. Smith

Abstract— Often emergency room and intensive care unit patients are in a condition too critical to be safely moved to a hospital's nuclear medicine suite to assess their cardiac function. To address this need we have built an economically practical mobile cardiac PET based imager for use in an intensive care/emergency room environment. The system is based on a pair of low profile 25 cm x 25 cm detector heads. Each head is structured in a modular fashion in that it utilizes an array of position sensitive photomultiplier tubes (PSPMTs) coupled to a NaI(Tl) crystal array. Sixteen Burle 85002-800 micro-channel plate-based PSPMTs are arranged to form each detector head resulting in a 25 cm x 25 cm field of view. The NaI(Tl) scintillating crystal array for each detector head is composed of 5 mm x 5 mm x 12.5 mm crystal elements spaced at a 5.5 mm step. The modular readout architecture has achieved over 100 kHz coincidence trigger rate. The system is now installed at Shands Hospital at the University of Florida and is undergoing phantom tests in anticipation of future clinical trials.

I. INTRODUCTION

THE University of Florida (UF) and Thomas Jefferson National Accelerator Facility (JLab) are collaborating on the development of a mobile cardiac PET based imager for use in an intensive care/emergency room setting. Often emergency room and intensive care unit patients are in too critical condition to be safely moved to a hospital's nuclear medicine suite to better evaluate their cardiac function. To address this need we have developed and built a mobile cardiac PET based imager for use in an intensive care and emergency room environment. No commercial source exists for a clinical PET system that can be moved into the limited space in an emergency room or operating room. The company Segami, Inc. does market a portable cardiac SPECT system but requires the patient to be seated [1]. Our goal was not only to develop a high performance system in a compact mobile package, but to also build an economically practical PET imager. Our detector system is patterned after a dual planar PET detector design that others and us have implemented for breast imaging [2, 3 &4]. We have described earlier the basic design concept of our detector heads for the mobile PET system which are based on position sensitive photomultiplier tubes (PSPMTs) and initial technology testing which we will summarize here. [5, 6 & 7]

The system utilizes a modular design of 16 detector modules based on the compact channel plate-based PSPMT. A total of 16 PSPMTs are used to form a detector head 25 cm x 25 cm in area. The analog signals from the PSPMT are readout and digitized using a JLab developed high rate FPGA based data acquisition ADC system. In Fig. 1 is a photograph of the two detector heads mounted in a mobile gantry at the University of Florida.

Fig. 1. Photograph of 25 cm x 25 cm detector heads attached to mobile gantry installed at the University of Florida.

II. METHODS

Each detector head is composed of sixteen separate PSPMT detector modules. The basic PSPMT detector module is based on a Burle [8] 85002-800 four-pad microchannel plate-based position sensitive photomultiplier tube that provides four high-rate analog outputs. Several PSPMTs in the first batch of Burle 85002-800 failed because of loss of vacuum. The manufacturer was able to modify their manufacturing process to deliver a more robust PSPMT. For each detector head we arrange 16 PSPMT units in which each PSPMT is spaced apart with a 1 cm gap resulting in a 4 x 4 array. Thus each detector head has a 25 cm x 25 cm field of view. Air coupled to the array of PSPMTs is a scintillation array (made by Saint-Gobain Crystals and Detectors [9]) of 5 mm x 5 mm x 12.5 mm NaI(Tl) pixels spaced at 5.5 mm providing a total active area of approximately 25 cm x 25 cm. The pixels are optically separated by white reflective/ diffusive epoxy material. Please see Fig. 2.
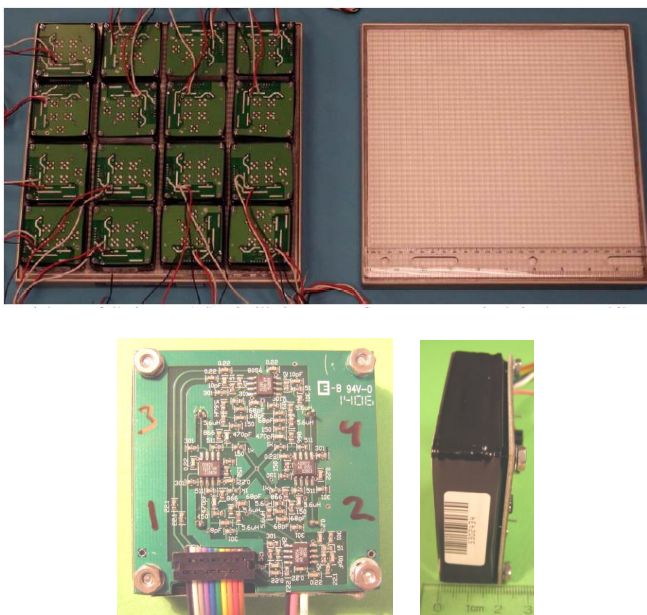

Fig. 2. At top are shown PSPMTs as arranged in which there is a 1 cm space between each PSPMT to cover the 25 cm x 25 cm FOV of the 5 mm pixel NaI(Tl) scintillation array, pictured separately at top right. In the two bottom pictures a single PSPMT with attached amplifier board is shown in two views. Total thickness of the very compact package PMT+card+connectors is less than 30 mm.

A total of 64 analog outputs are therefore read per detector head thus requiring 128 ADC channels for the whole system. The fast pulse per detector head is formed by summing all 64 pads and producing a corresponding fast constant fraction discriminator trigger pulse for two-head coincidence requirement or single gamma imaging mode trigger. A special interconnect board collects pad signals from individual PSPMTs for transfer via cables to the DAQ system. The board also distributes individually adjusted high voltages (HVs) to each PSPMT module. The individual HV-PSPMT bias voltages are adjusted to assure that all PSPMT modules in the detector head have similar gain and signal response to the same initial energy deposited (511 keV).

To assure good optical coupling of scintillator pixels opposite the dead regions between the sparsely placed PSPMTs, an additional optical light-guide was added between the 5 mm glass window of the encapsulated NaI(Tl) array and PSPMTs. This light-guide is made of a high quality 20 mm thick UV acrylic plate. Light sharing between the detector modules is achieved by the use of the light-guide resulting in the "dead" regions between PSPMTs resulting in only a 45% drop in signal across the gap. To guarantee long-term optical coupling stability, only dry optical couplings were used between both windows and the PSPMTs. Please see Fig. 3 below for an example of the raw image acquired. We used a ^{22}Na point source to obtain the image.
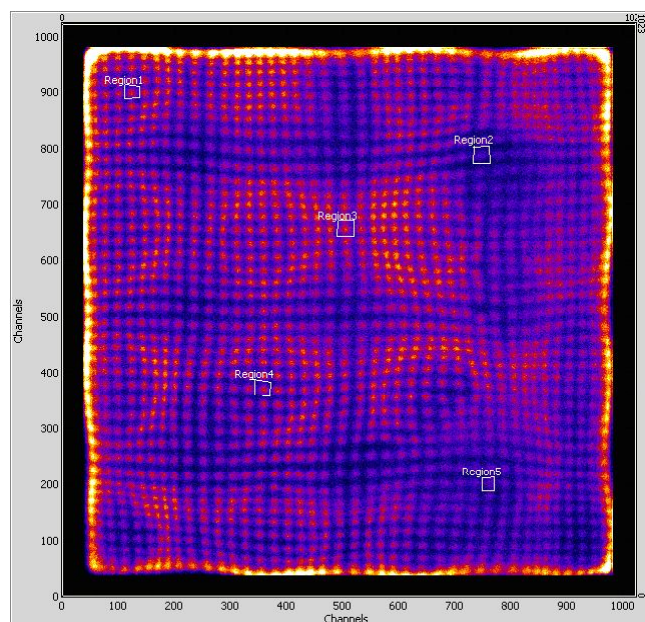

Fig. 3. Example of a raw flood image from a fully illuminated detector head (with a 22Na source) after first-order gain uniformity correction (by adjusting HV biases of individual PMTs). Good pixel separation over the whole field-of-view is observed. Response non-uniformities are still evident because of remaining gain differences, dead regions between individual photomultipliers, and low granularity (~2.5 cm) of the PMT pad readout. See Fig.4 for individual energy spectra for the regions of interest for the single crystal elements indicated by white rectangles.

In Fig. 4 is shown the variation of gain and energy resolution across the array. As can be seen all crystal elements show good energy resolution of about 15-20% at the 511 keV photopeak confirming proper operation of the detector across all regions of the active surface. The range of amplitudes of about factor of 2 is observed after first-order adjustment of response uniformity.

To achieve high rate capability, each detector head is connected to a separate JLab developed 64 channel FPGA DAQ card [10]. This card is read out via a USB2 link to a

separate data acquisition PC. Two data acquisition PCs, each used for one detector head, send the collected data files for processing to a next level "event builder" computer.
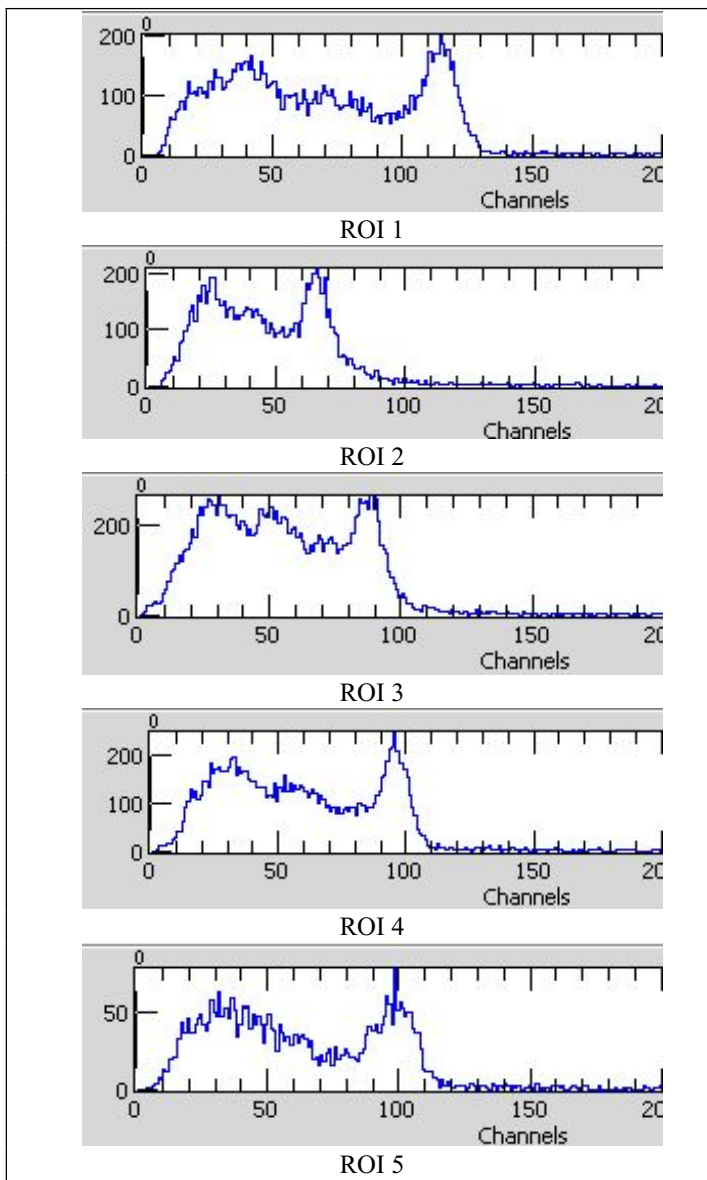

Figure 4: Examples of ^{22}Na energy spectra obtained from selected characteristic five NaI(Tl) crystal elements (corresponding ROIs are shown in the raw image in Fig. 3).

Please see Fig. 5. On the "event builder" computer time-stamped data files are collected separately for each detector head. The pair of files file can be processed and fused into a single coincident file or treated separately when used in a single gamma mode for detector testing.

During the coincident file event building phase, recorded and time-stamped events corresponding to two coincident 511 keV photons from both detector heads are processed and put into a summary file, listing final calculated x and y gamma event positions and gamma ray energies for the two gammas from both detector heads, plus an event time stamp for each acquired coincident event, with ~5 ns time accuracy.

FPGA ADC data acquisition is controlled by distributed Java-based software. Java-based server application sits on each of the acquisition computers and directly controls one FPGA ADC board through a USB2 connection. The USB driver for the FPGA board is directly accessed by C++ code; the JNI (Java Native Interface) is used to allow Java indirect control of the USB driver.
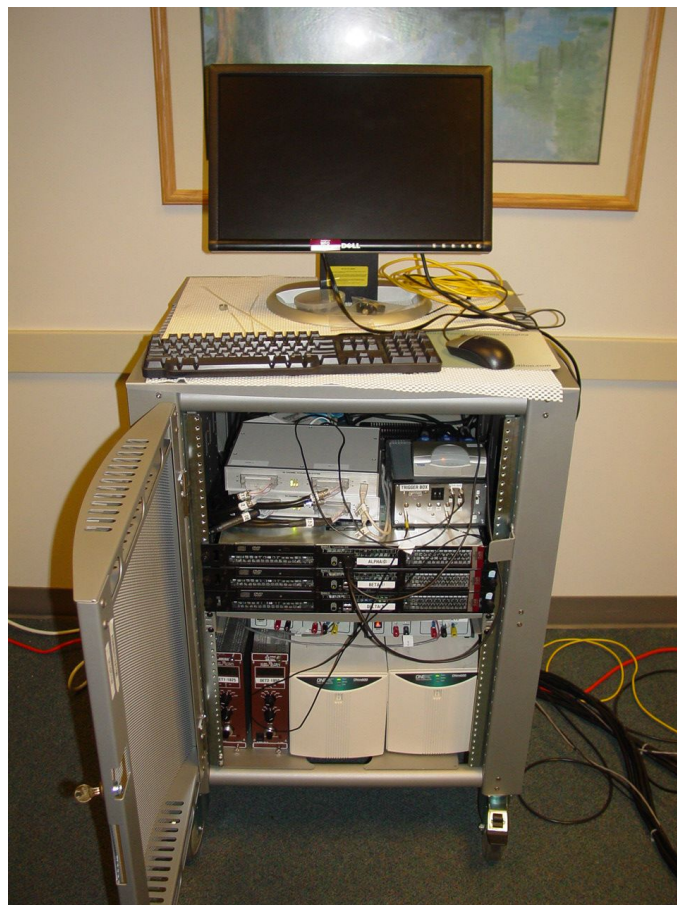

Fig. 5. Photograph of mobile electronics rack. Installed are three rack mounted PCs, two FPGA based ADC modules, low voltage and high voltage power supplies and two hospital grade un-interruptable power supplies with the monitor and keyboard.

The server application on each of these machines is controlled by a remote client Java-based application on the control event builder computer that coordinates the collective acquisition, transfer, and processing of data. The client application is connected to each of the four server applications through a dedicated gigabit Ethernet network. After data is acquired and written to disk on the acquisition computers, the server application transfers data to the remote client computer. Finally, the client application sorts through data from coincident detectors, matches events by the time stamp and then sends the data for reconstruction. Details of the software architecture are described elsewhere at this conference [11].

The software analysis program reads data written to disk by the acquisition software in order to display raw images, implement calibrations and corrections, and provide tools to characterize the two detector head system performances. A special position algorithm uses digitized raw pad signals from all 64 pads of sixteen PSPMTs to obtain raw gamma event positions. Below in Fig 6 is a photograph of the two detectors mounted in the mobile gantry at the University of Florida.
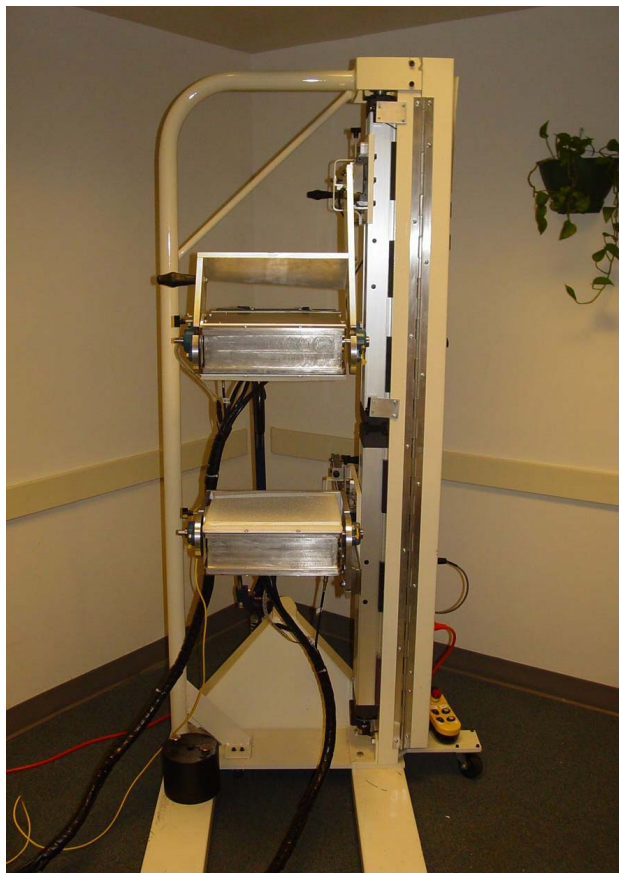

Fig. 6. Photograph of the complete mobile PET imaging system in place at Shands Hospital at the University of Florida.

III. RESULTS

The cardiac imager can operate with over 100 kHz coincidence trigger rate and achieves uniform detection efficiency across the 25 cm x 25 cm FOV, including dead regions between PSPMTs where signal decreases to no less than about 55% relative to the on-PMT signal value. Initial timing resolution of about 5 ns FWHM was achieved for a single detector head (against fast trigger detector). One of the detector heads was shipped back to Jefferson Lab to undergo a PSPMT replacement. The detector head was damaged through shipping. Once the detector is repaired we intend to continue testing the performance of the system in anticipation of clinical trials.

IV. SUMMARY

We have in place at the University of Florida a mobile cardiac PET based imager for use in an intensive care/emergency room setting. Our system is based on 16 Burle 85000 PSPMTs coupled to a NaI(Tl) scintillating crystal array for each head. The arrays are composed of 5 mm x 5 mm x 12.5 mm thick crystal elements spaced at a 5.5 mm step. Early evaluation tests demonstrated that the imager is a high performance economically practical PET imager system in a compact mobile package. The detectors underwent initial tests at the University of Florida and are reported also at this conference [12].

V. ACKNOWLEDGMENT

VI. REFERENCES

[1] Segami Corporation, Columbia, MD.
[2] C. J. Thompson, K. Murthy, R.L. Clancy, J. L. Robar, A. Bergman, R. Lisbona, A. Loutfi, J. H. Gagnon, I. N. Weinberg, R. Mako, "Imaging Performance of PEM-I: A High Resolution System for Positron Emission Mammography (PEM)," Nuclear Science Symposium and Medical Imaging Conference Record, Vol. 2, Pg. 1074-1078, 1995.
[3] M.F. Smith, S. Majewski, A. G. Weisenberger, D. A. Kieper, R. R. Raylman, T.G. Turkington, "Analysis of factors affecting positron emission mammography (PEM) image formation," IEEE Transactions on Nuclear Science, vol. 50, no. 1, pp: 53-59, Feb. 2003.
[4] M. F. Smith, S. Majewski, R. R. Raylman, "Positron emission mammography with multiple angle acquisition," Nuclear Science Symposium and Medical Imaging Conference Record, vol. 3, pp: 1883-1886, 2002.
[5] U.J. Tipnis, D.R. Gilland, M.F. Smith, W.E. Drane, S. Majewski, "Design of a compact, mobile PET detector for bedside cardiac imaging," Nuclear Science Symposium Conference Record, 2003 IEEE, vol 4, pp: 2438 - 2441, 19-25 Oct. 2003.
[6] S. Majewski, W. Gunning, R. Hammond, B. Kross, M. Smith, V. Popov, J. Proffitt, A. Weisenberger, R. Wojcik, and D. Gilland, "Development and Evaluation of Detector Heads and Readout for a Mobile Cardiac Imager System," presented at 2006 IEEE Nuclear Science Symposium and Medical Imaging Conference.
[7] U. J. Tipnis, M. F. Smith, T. G. Turkington, J. Wilson, S. Majewski, B. Kross, R. Wojcik, D. R. Gilland, "A simulation study of a bedside cardiac PET imager," Nuclear Science Symposium Conference Record, 2004 IEEE vol. 5, pp 3126-3129, 16-22 Oct. 2004.
[8] Burle Industries, Lancaster, PA.
[9] Saint-Gobain Crystals and Detectors, Newbury, OH.
[10] J. Proffitt, W. Hammond, S. Majewski, V. Popov, R.R. Raylman, A.G. Weisenberger, R. Wojcik, R, "A flexible high-rate USB2 data acquisition system for PET and SPECT imaging," IEEE Nuclear Science Symposium Conference Record, vol. 5, pp: 2971 – 2975, 2005.
[11] J. E. McKisson, W. Hammond, J. Proffitt, A. G. Weisenberger, "A Java Distributed Acquisition System for PET and SPECT Imaging," presented at 2007 IEEE Nuclear Science Symposium and Medical Imaging Conference.
[12] M.T. Studenski, J.G. Parker, D. R. Gilland, S. Majewski, W. Hammond, "Performance Evaluation of a Small Field-of-View, Mobile PET/SPECT System," presented at 2007 IEEE Nuclear Science Symposium and Medical Imaging Conference.